CONVECTIVE FLOWS UNDER CONDITIONS APPLICABLE TO FIRES IN HIGH RISE BUILDINGS

by

Johnnie B. Cannon, Jr.

In Partial Fulfillment of the Requirements

For the Degree of

Doctor of Philosophy

California Institute of Technology

Pasadena, California

1974

(Submitted September 20, 1974)

ACKNOWLEDGMENTS

The author is indebted to his thesis advisor, Professor Edward E. Zukoski, for his guidance and encouragement throughout all aspects of this research project.

Also, thanks are due to Doctors R. Koh, T. Kubota, J. List, and J. Imberger for their many helpful suggestions and criticisms during certain phases of this project.

Most of the experiments were performed at the W. M. Keck Hydraulics Laboratory of the California Institute of Technology. Elton Daly and his staff were very helpful in constructing the apparatus for this project. Also, Ty Linton was instrumental in the design and construction of some of the apparatus.

Thanks are due to J. F. Saint-Marcoux for performing the preliminary heat transfer experiments.

The first draft of this report was typed by Joan Mathews and my faithful wife, Sandra. Roberta Duffy typed the final draft, and the figures were drawn by Ty Linton and Betty Woods.

This research was supported by a grant from the National Science Foundation, GI 31892X, X1. The author was also supported by fellowships and teaching assistantships from the California Institute of Technology.

ABSTRACT

This study was an attempt to analyze convective flow patterns under conditions applicable to fires in high rise buildings when natural convection alone is the most important driving force. The primary aim of this investigation was to consider the turbulent flow in vertical shafts caused by hot gases entering the bottom of the shaft which is already filled with a cooler (denser) gas, and hence creating an unstable density field.

The small scale model used to study this problem consisted of a vertical tube of dense fluid placed in an infinite (less dense) fluid environment. General scaling laws were developed for the variation of density with time for the flow set up in the model. Also, an analytical model was developed to account for the observed mixing rates in this simple configuration.

In the analysis, the diffusion equation was solved and found to be in agreement with the small scale model. The mixing coefficient for this unstable system is

$$E_z = 0.28 \sqrt{\frac{g}{\rho_a} \frac{\partial \rho}{\partial z}} \, (d^7 L)^{1/4} ,$$

where the constant, 0.28, was determined empirically, and the fundamental time scale that characterizes the mixing in the vertical column is

$$\tau = \sqrt{\frac{\Delta \rho_i}{\rho_a} \frac{g}{d}} \left(\frac{d}{L}\right)^{9/4} t \, .$$

Later, the above techniques were used to investigate in a more superficial way the effects on the mixing rates of geometric variations, limited external environments, changes in the internal geometry of the shafts, gas density ratio, and heat transfer.

TABLE OF CONTENTS

LIST OF FIGURES

LIST OF FIGURES (Cont'd.)

LIST OF FIGURES (Cont'd.)

LIST OF FIGURES (Cont'd.)

LIST OF TABLES

1. INTRODUCTION

1.1 Background

High rise buildings are found throughout the world. They are symbolic of the economic growth of any prosperous city. However, fires in such buildings are very difficult to cope with. The construction of skyscrapers has advanced more rapidly than the local fire departments. As a result, they are not properly equipped to handle fires in the multi-story buildings, and many lives are lost each year.

Fires in multi-story buildings are much different from those in conventional buildings. The difference is that isolated fires on lower floors create tremendous buoyancy forces that drive the hot gases to the upper floors. These toxic gases usually account for most of the deaths. The amazing phenomenon is that although the fire often does not reach the top floors, the death toll is usually highest there. For instance, a fire in a fourteen story hotel in Jacksonville, Florida killed twenty-two people[1]. It occurred in the ballroom of the first floor and was under control within 30 minutes. During that time, however, smoke spread to the ceiling of the ballroom and up 15 vertical pipe shafts, each about 2' by 5', and thus passed through the building to the top floor. The smoke advanced through access panels to the corridors and into a number of the bedrooms, and eventually produced the deaths of people caught between the 6th and 13th floors. The people who died occupied the floors as follows: 8 on the 13th floor, 4 on the 12th floor, 5 on the 11th floor, 2 on the 10th, 2 on the 9th, and 1 on the 6th floor. This incident reflects the situation of movement of smoke into the upper floors remote from the fire, and

also that heat is not the primary cause of most fire-related deaths.

The nation spends about 105 million dollars annually on research and development related to fires[2]. This amounts to less than one per cent of the cost of destruction caused by fires in the United States. Until recently, more emphasis was placed on the evacuation of the occupants of burning buildings. Now researchers are placing more emphasis on the movement of smoke. This study is an attempt to analyze the propagation of toxic gases to the upper floors of multi-story buildings as a result of natural convection. Knowledge of the time required for the smoke to reach a lethal concentration on the upper floors of a building may be valuable in saving lives and in the design of building construction codes.

1.2 The Propagation of Fires in High Rise Buildings

The spread of fire in all buildings is qualitatively similar. It essentially consists of three phases, as shown in Fig. 1.1. They are (1) the ignition, (2) the growth within the compartment of origin, and (3) the spread between adjacent compartments. If the fire does not extinguish itself, it may lead to total involvement and spread to other enclosures. The growth of the fire within the compartment does not change if it is taking place in a multi-story or conventional building; but once the fire propagates beyond the room of origin, the fact that it is in a high rise building becomes relevant in relation to the spread of the toxic gases. Figure 1.2 is a schematic of a building that depicts the phenomena occurring as a result of an isolated fire. It consists of a room where the isolated fire is initiated and a long corridor that connects the room with the stairwell or elevator shaft.

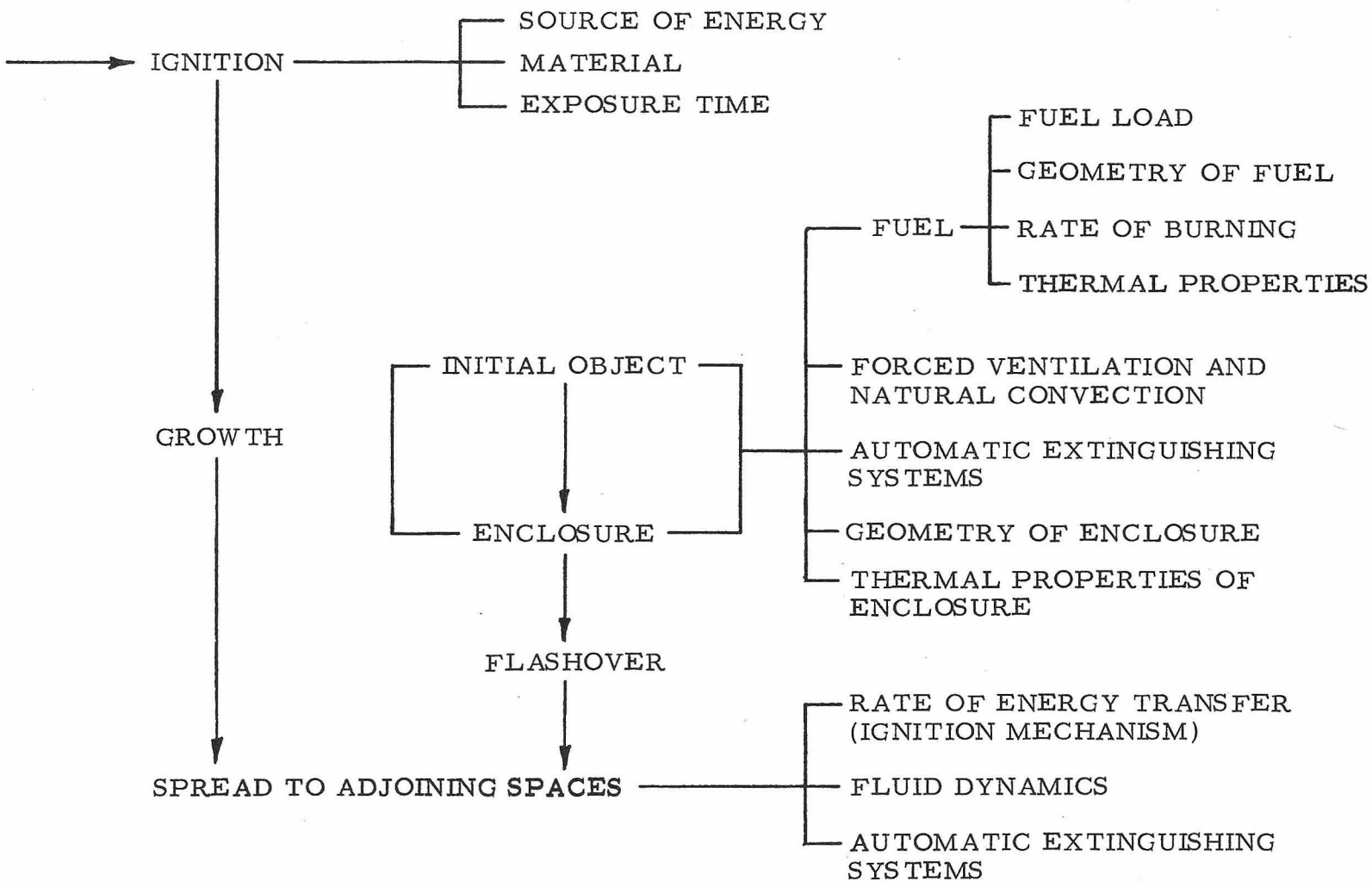

Fig. 1.1 Factors Affecting Ignition, Growth, and Spread of Fire in a Building (after Airlie House, 1971).

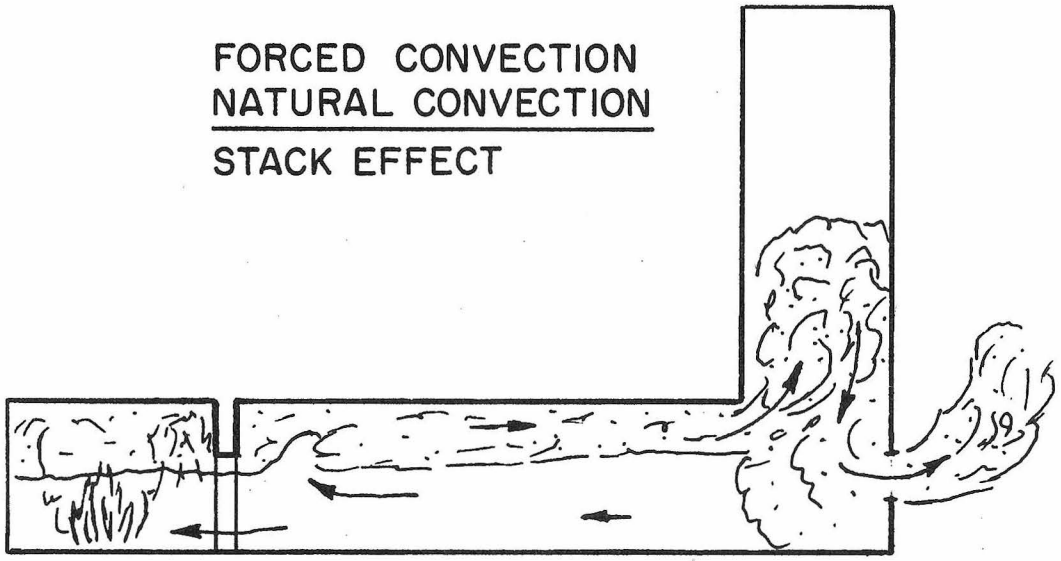

Fig. 1.2 Schematic Drawing of Fire in a Building.

The mechanism by which the isolated fire spreads throughout the enclosure depends primarily on the fuel. Energy is transferred by convection currents (natural or forced) and radiation. After a certain amount of energy has been absorbed by the enclosure, the entire room will burst into flames, Fig. 1.3. After a fire is ignited and spreads, the transfer of energy by combustion processes to the air and combustion products produces an increase of pressure in the compartment primarily due to the reduction in density, i.e., expansion of the heated air. The pressure gradient that exists between the room and corridor, for example, causes convection to take place in the absence of any ventilation systems. In addition, hot gas produced in the fire will spill out under the door and spread down the hall.

The fluid motion that takes place in the corridor is coupled to that in the room. It consists of a two-layered flow system as shown

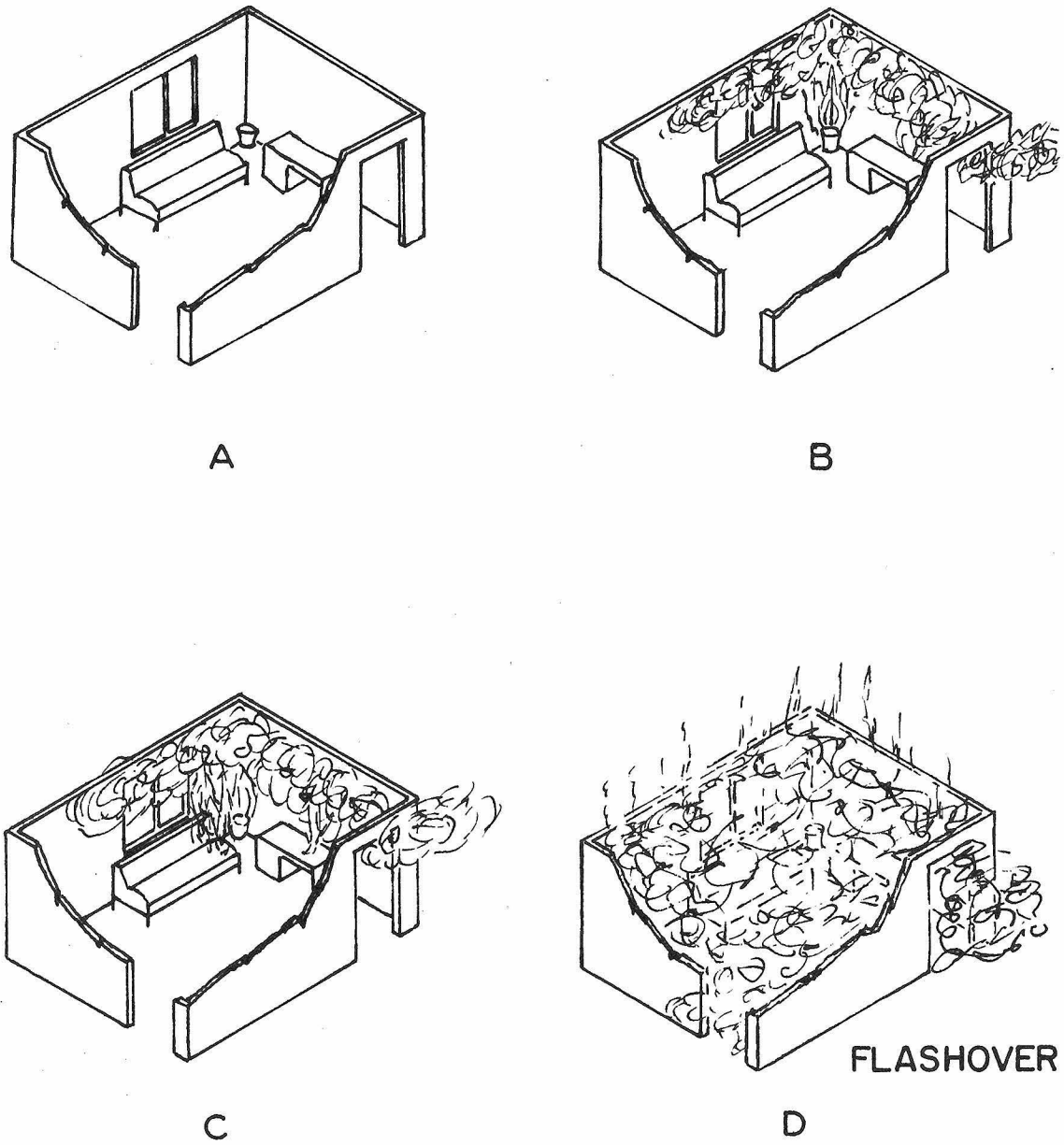

Fig. 1.3 Development of a Typical Room Fire (after Fitzgerald, 1973).

in Fig. 1.2. The gas that propagates to the upper floors is on the top, and the bottom layer is the cold return flow. The return flow supplies the oxygen to the fire in the room which is necessary to sustain itself. Besides the mixing taking place between the hot and cold layers of the gases, the only energy being transferred in the corridor is through the upper walls by conduction.

The elevator shafts and stairways connect all other floors of the building to the one where the fire exists. Strong buoyancy forces drive the toxic gases to the upper floors. Initially, there is a cold column of gas resting on top of a hot layer. Since the system is unstable, the cold gas falls and the hot gas rises in some fashion. The extent of mixing of the hot and cold fluids determines the rate at which the upper floors fill up with the toxic gases. The dynamics and mixing involved in this phase are the central theme in this document.

1.3 Objectives and Scope of Study

Problems due to the movement of smoke in high rise buildings have been widely discussed[3], but only a few analytical and experimental models[4] exist. The non-existence of scaling laws is due primarily to the difficulty of simulating the movement of smoke. Fung[5] made a quantitative study of a pressurized stairwell smoke control system for a 12-story apartment building. Smoke was simulated by the flow of air from a room on the bottom floor of the building. The air was heated $10^{\circ}F$ above the corridor temperature and mixed with a certain percentage of SF_6 tracer. Although this model is useful, the buoyancy force created by the 10 degree temperature difference is very small. In a real fire, the temperature rise may be as high as

800 degrees. For this reason, fire models that contain useful quantitative data on the movement of smoke up vertical ducts are scarce.

This study deals with the propagation of hot gases to the upper floors of a high rise building. It seeks to provide a fundamental time scale to characterize the mixing in vertical ducts due to an unstable density field. An understanding of the physical mixing laws can aid researchers in their quest to simulate the movement of smoke in buildings.

The remaining chapters of this report deal with the presentation and validation of a model simulating the transport processes of hot gases in building fires due to natural convection. Chapter 2 defines each problem being considered and states the relevant questions to be answered in each case. Chapter 3 discusses the experimental approach to the various problems and gives a brief description of the small scale models. Chapter 4 gives a complete description of the mixing mechanism observed in the experimental model and develops analytical models to predict the mixing rates and density profiles found in the small scale models. Chapter 5 discusses the experimental apparatus and procedures of the various models, and Chapter 6 presents and discusses the experimental data and compares them to the analytical results. The summary and conclusions of this study are given in Chapter 7.

2. STATEMENT OF THE PROBLEM

The primary aim of this research project was to study natural convective flow patterns in high rise buildings due to fires. The propagation of fires in multi-story buildings was discussed briefly in Chapter 1. There we pointed out that elevator shafts, stairwells, and other vertical ducts are the primary sources by which hot gases escape to the upper floors of the buildings. Because of their relative importance, the dynamics of the buoyancy-driven motion in vertical ducts received the most attention in this report.

We have primarily considered the transient flow problem shown schematically in the left hand side of Fig. 2.1. A fire starts in the room and generates hot gas which then runs down the hall and begins to propagate up the stairwell or elevator shaft. In some manner, hot gases of temperatures ranging from 800° to 1500°F enter the stairwell and replace the cold, dense air initially present. The density stratification, prior to and after the initiation of the mixing process, is unstable because of the constant existence of hot gas at the bottom of the stairwell and the mixture of cooler, and hence more dense, gases at the top of the stairwell. (To avoid forced convection effects, we have assumed that the only entrance to the duct is through the bottom.)

From this often-realized situation we have abstracted for study the simpler problem shown in the right hand side of Fig. 2.1. That is, we consider the transient density changes occurring in a vertical shaft closed at the top and initially filled with a dense (cool) fluid. At the start of the problem, the bottom of the shaft is suddenly opened and the dense fluid is exposed to an unlimited volume of less dense (hot) fluid.

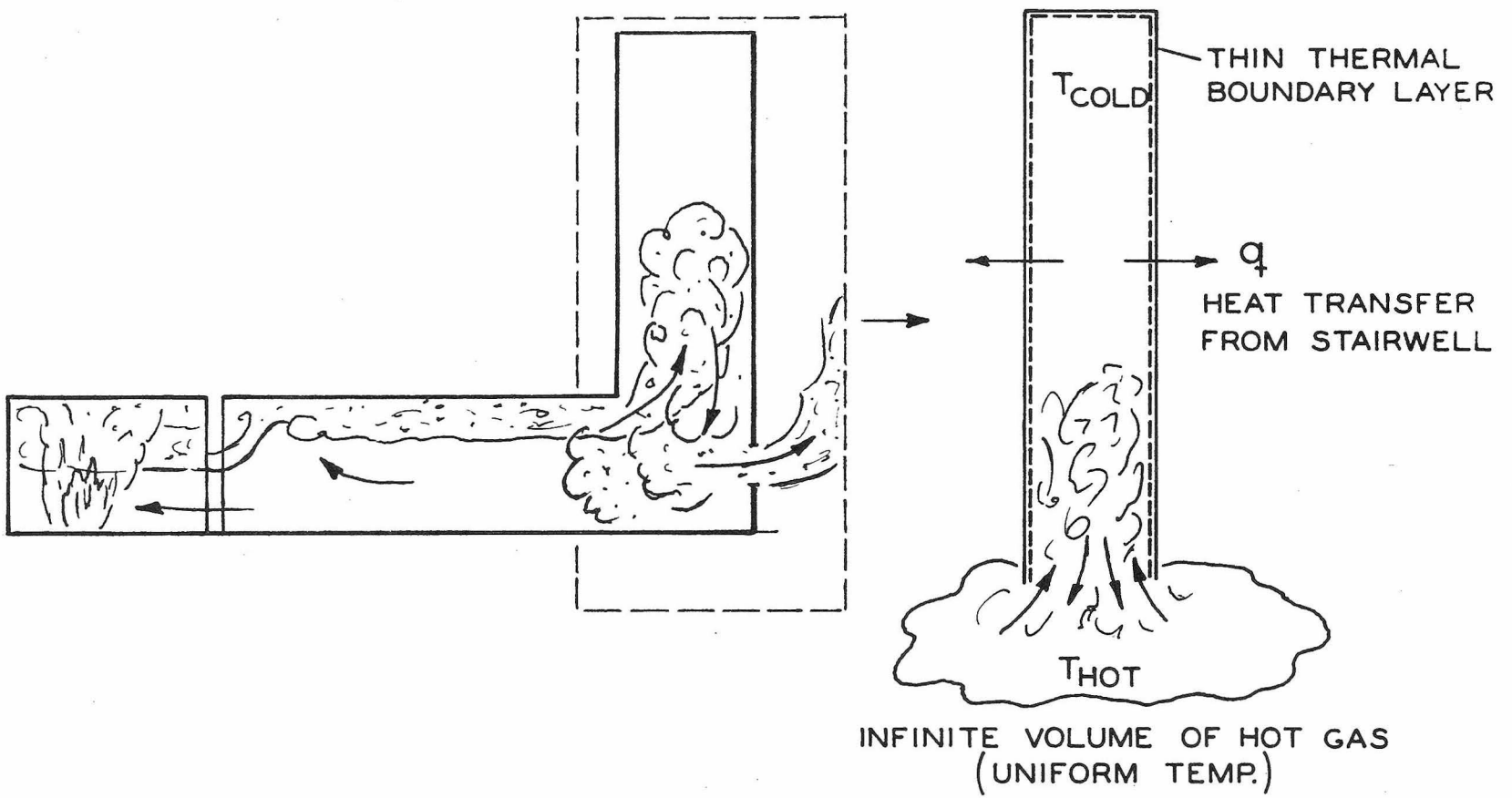

Fig. 2.1 Definition Sketch of Mixing Phenomena Associated with Fire in a Stairwell.

The dynamics of this problem are controlled by density differences in the gas and heat flux to the walls of the duct. To simplify our study further, the problem was divided into two major categories: (1) a buoyancy force model, and (2) a heat transfer model. The buoyancy model was treated in much more detail than the heat transfer model (which is not yet completed).

In addition to this problem, a number of related examples were studied briefly. A concise statement of the aspects of each model investigated is considered in the following sections.

2.1 Buoyancy Force Model

In the buoyancy model we attempt to analyze only the effects of large density differences due to temperature without the influence of heat transfer from the system. The following subsections present the questions to be studied in each case of this model.

2.1.1 Vertical Duct (Stairwell). Consider a fire in a large volume below the inlet of an insulated duct that is closed at the top, as shown in Fig. 2.2. Although this is an oversimplification of the problem, the fire is assumed to supply a continuous source of buoyancy in the stairwell. In essence, the fire and volume surrounding it are replaced by an infinite volume of hot gas at the same temperature as the fire. The basic questions to be answered may be stated in the following manner.

1) How long does it take the hot gas to propagate to the top of the stairwell? Is the stratification always unstable?

2) Physically, in what manner does the hot air displace the column of room temperature air in the vertical duct? Is it

turbulent, or does the cold air fall along the walls of the vessel or along one side?

3) Is the motion of the gas in the duct reproducible? If so, can it be modeled physically on a small scale?

4) What are the important parameters and scaling laws that affect the dynamics of this problem? For example, what role does viscosity play, etc.?

5) In particular, what effect does the aspect ratio, L/d, have on the mixing rates of the hot and cold air if it is turbulent?

2.1.2 Corridors. We pointed out in the Introduction that the corridor links the room with the fire to the stairwell in this example. The motion of the gas in this case has received much attention by workers in other fields, such as density currents[6] and stratified flow[7]. The main problem is concerned with the transfer of energy and momentum between two counterflowing streams. In this case, the opposing streams are the fresh supply of cold air en route to the fire and the stream of hot, toxic gases emitted by the fire en route to the exit or upper floors. The behavior of the two streams influences the fire and its propagation, and the spread of toxic gas.

2.1.3 Stairwell-Corridor System. In most instances, fire spreads from floor to floor upward. That is, the hot gases propagate to the stairwell and up it to other floors. Combustible materials are preheated along the way. Usually, the toxic gases leave the stairwell by way of corridors on each floor. A simplified version of a stairwell-corridor system is shown in Fig. 2.3. The dynamics of the gas motion

in the vertical duct is changed because of the addition of the corridor. The obvious question is: "does the corridor increase or decrease the mixing rates in the vertical duct?" Do the same mixing phenomena exist in both the horizontal and vertical portions of the tubes? From experience, one expects a two-layered flow system to exist in the horizontal attachment. However, the effect of the change in direction of the momentum vector from horizontal to vertical orientation is not known.

2.1.4 Stairwell-Basement System. Consider a fire in a basement, or in some other enclosure of limited extent, that is connected to a vertical duct as shown in Fig. 2.4. In this example, the fire is not allowed to burn throughout the duration of the mixing process. The essential point is that a limited supply of buoyancy is present instead of an unlimited supply as was the case in the previous problems. Now the mixing rates in the vertical duct will be different because the amount of potential energy in the system is much less. The same basic questions may be asked in this problem as with the case of a continuous source of buoyancy.

2.1.5 Stairway System. The addition of stairs in the stairwell, Fig. 2.2, complicates the problem a little more. For simplicity, the stairs may be viewed as baffles spaced equal distances apart, as depicted in Fig. 2.5. Since the baffles are streamlines with respect to flow in the duct, one expects the flow to be more predictable than in the initial problem. However, the obvious question is: "do the stairs speed up or slow down the mixing in the duct?" If it takes a longer period of time for the hot gas to reach the top of the duct,

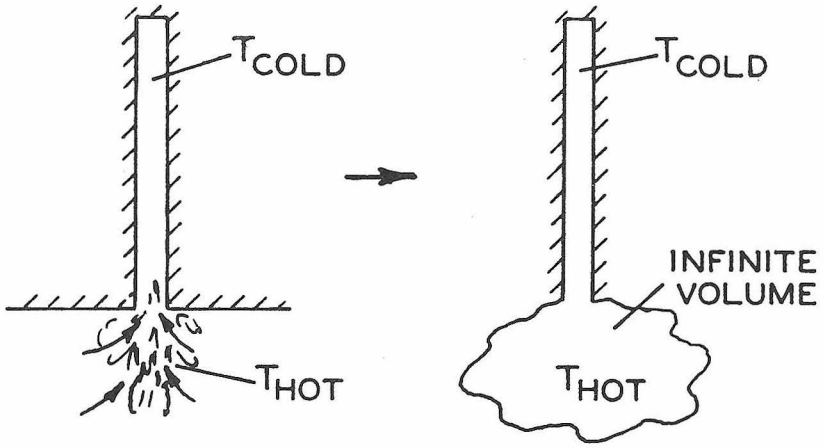

Fig. 2.2 Fire in a Closed, Insulated Stairwell.

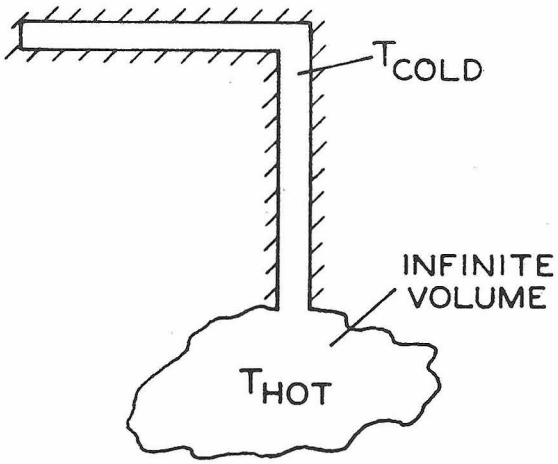

Fig. 2.3 Schematic of Stairwell-Corridor System.

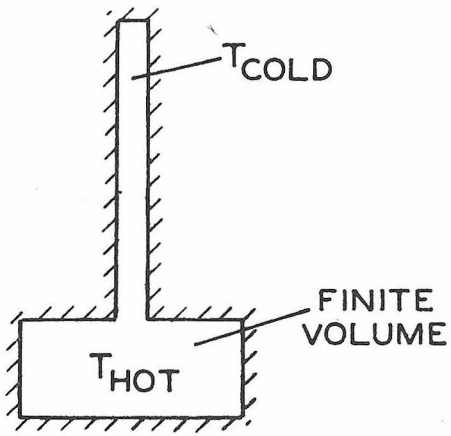

Fig. 2.4 Schematic of Stairwell-Basement System.

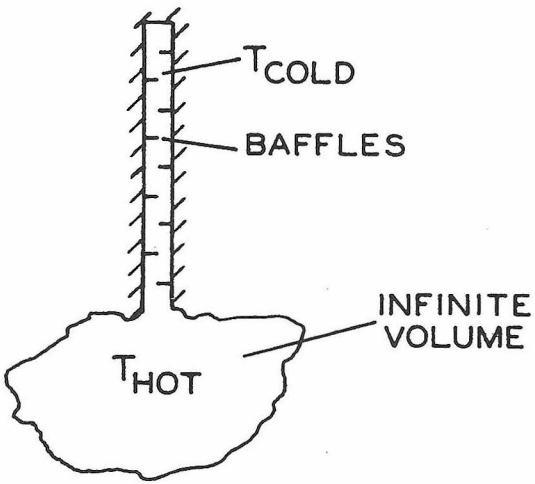

Fig. 2.5 Schematic of Stairway System.

the stairs serve a dual purpose. That is, along with the known purpose of transporting people, it may also be a life saver with respect to fire, or vice versa.

2.2 Heat Transfer Model

In the buoyancy model, all of the ducts were insulated. An effort was made to isolate the heat transfer and to consider the dynamics of the gas due only to density differences. However, the addition of heat transfer to the system complicates the problem even more. The schematic in Fig. 2.1 shows that energy is drained out of the system because the walls of the stairwell are at a lower temperature than that of the hot gas, initially. Eventually, the walls heat up. A question that arises is: "since energy is drained out of the stairwell, is it possible to inhibit the mixing process so that the hot gases will not penetrate to the top of the duct during the initial stages of the fire?" A priori, one expects that the heat transfer from the hot gas will reduce the mixing rates, but to what extent is not known.

The above problems are of fundamental importance in relation to the propagation of toxic gas and fire in a high rise building. This research study is an attempt to investigate each of them. They are considered in more detail in the following chapters.

3. MODEL REPRESENTATION

Small scale models were used to examine the mixing phenomena associated with the problems stated in Chapter 2. Initially, salt-water mixtures were used to model the dense (cool) gas and water alone to model the less dense (hotter) gas. In this program we attempted to:

1) develop general scaling laws for the variation of density with time in the flow set up in a vertical tube placed in an unlimited surrounding atmosphere;

2) develop an analytical model which can account for the observed mixing rates in these simple configurations;

3) use the above techniques to investigate what the effects of geometric variations, limited external atmospheres, and changes in the internal geometry of the shafts would have on the mixing rates.

Later, we used gases of uniform temperature but different densities, $\Delta\rho/\rho > 1$, to produce the buoyancy forces in the gases in a more realistic manner. Temperature differences alone (rather than specie changes) were used in this manner too. Then the effects of large density differences and heat transfer were considered.

This chapter explains briefly the physical models used to study the various problems. Also, consideration is given to the physics and scaling laws used in conjunction with the models.

3.1 Buoyancy Force Model

In the buoyancy force model, the stairwell was replaced by a cylindrical tube immersed in a large basin filled with a lighter mis-

cible fluid. Brine solutions and dense gases were used as the heavy fluids, whereas the less dense fluids were tap water and air, respectively. A schematic of the system is shown in Fig. 3.1. In this particular case, the tube was filled with a salt solution and placed vertically over a large basin of tap water. The mouth of the tube was placed several diameters below the water surface in the basin. Initially, a partition separated the brine solution and the tap water, and the mixing began when this partition was removed.

The mixing, subsequent to the removal of the partition, was very turbulent. A distinct front propagated up the tube rapidly. Violent mixing existed on the lower side of this front, whereas the

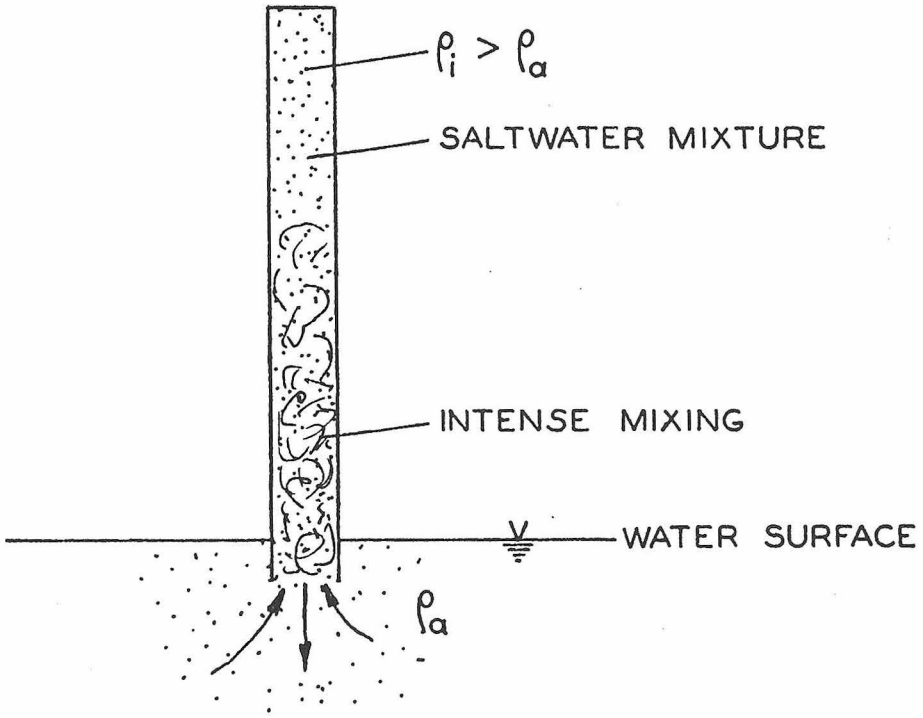

Fig. 3.1 Schematic of Mixing Phenomena in Brine Solution Model.

brine solution on the upper side was motionless. Later the front reached the top of the tube and turbulent mixing existed everywhere in the duct.

Both dense gases and brine solutions were used in the vertical duct problem (unlimited source of buoyancy). In the other problems with their specific geometries, use was made of brine solutions as in the case cited above. In each instance, the ducts were cylindrical and the intense turbulent mixing was observed.

3.1.1 Scaling Laws. The density at any point in the tube has the form

$$\frac{\rho-\rho_a}{\rho_i-\rho_a} = F(x, \tau) ,$$

where $x = Z/L$ and τ is a dimensionless time. The purpose of this study is to find the fundamental time scale, τ, that characterizes the mixing. From dimensional arguments, τ may be written as

$$\tau = f\left(\sqrt{\left(\frac{g}{d}\right)\frac{\rho_i-\rho_a}{\rho_a}}\, t,\ L/d,\ Gr \right) ,$$

where Gr is the Grashof number. Note that $(\Delta\rho_i/\rho_a)$ was included with the first dimensionless group. However, it may also appear as as a separate variable when $\Delta\rho_i/\rho_a >> 1$.

The Grashof number has the form

$$Gr = \left(\frac{\rho-\rho_a}{\rho_a}\right)\frac{gd^3}{\nu^2} ,$$

where ν is the kinematic viscosity. In a real fire, the properties of the heated gases change drastically. Roughly, the kinematic viscosity

and the thermal diffusivity change by a factor of 10 if one compares the hot and cold gas values. For example, the Grashof number, based on a fire at $500^{\circ}F$ in a duct of diameter of 10 ft., is of the order of 7×10^{11}. If the gas temperature is $2000^{\circ}F$, it is roughly 2.5×10^{10}. The Reynolds number, Re, which can be expressed here as the square root of the Grashof number, ranges from 1.5×10^{5} to 8.5×10^{5} in the above examples. The largest values of Gr and Re indicate that the flow is certainly turbulent in a real fire. Although the molecular transport quantities change by a significant amount in the fire, it is the turbulent transport of energy and momentum that dominate the dynamics of this problem.

In the brine solution model used in these experiments, Grashof numbers are roughly $1/2 \times 10^{10}$, and hence Reynolds numbers are about 0.7×10^{5}. These values are somewhat smaller than the comparable values in a fire, but are close enough so that no large differences are anticipated. Therefore, we assumed that the important parameters in the model are $\frac{\Delta\rho}{\rho}$ g, d, and L, and that viscosity could be omitted. All of the small scale experiments were aimed at finding the fundamental time scale, τ, and mode of density change based on these quantities.

3.2 Heat Transfer Model

Heat transferred through the walls of the vessel was neglected in the previous model, and an attempt was made to solve the more basic problem of buoyancy. The dynamics of the gas motion is changed, somewhat, because of the loss of potential energy of buoyancy due to heat transfer. In the prototype, the heat capacity of the

gas is much smaller than that of the duct. For example, consider a cylindrical duct made of concrete, filled with air at room temperature. The cylinder is 15' long, 1/2' thick, and its diameter is 10'. The heat capacity of the concrete duct is roughly 6800 BTU/^{o}F, as compared to 7$\frac{1}{2}$ BTU/^{o}F for the volume of air in it. If the same amount of energy is absorbed by both the duct and the volume of air in it, the temperature change of the duct is negligible relative to the temperature change of the air.

Therefore, it takes much more energy to heat the walls of the duct than it takes to heat the volume of gas in it. This implies that the temperature of the walls of the duct will essentially remain fixed or will change slowly during the mixing process in the stairwell. Since the walls are cool, they will act as a constant-temperature heat sink and have a tendency to drain energy from the hot gases. Figure 3.2 is a schematic of the energy transfer mechanisms.

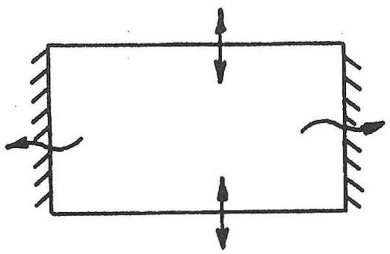

Fig. 3.2 Schematic of Energy Transfer Mechanisms in Heat Transfer Model.

The experimental set-up of the heat transfer model was very similar to that in the buoyancy model, Fig. 3.3. It consisted of a vertical tube whose walls were maintained at a very low temperature.

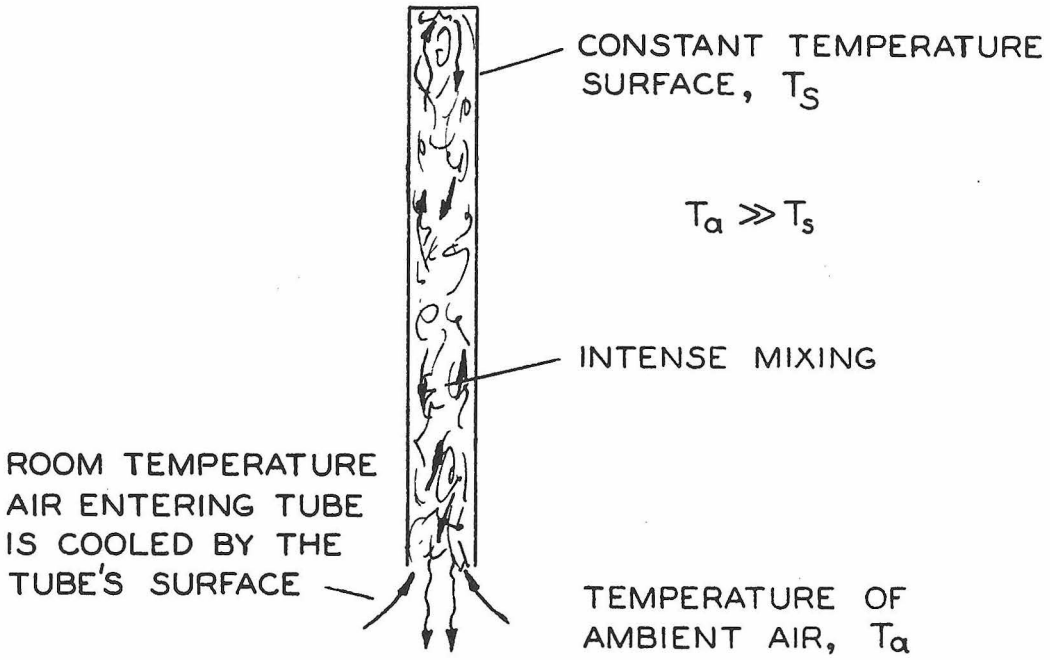

Figure 3.3 Schematic of Mixing Phenomena in Heat Transfer Model.

Initially, the air in the tube was chilled to the same temperature as that of the surrounding walls. The experiment began when the partition separating the ambient air and the cold air in the tube was removed. The mixing was very turbulent, as before. The room temperature air entering the tube was cooled by the walls of the vessel during the mixing process. Thus, the temperature of the gas near the top surface was much lower than that of the gas near the inlet of the tube, and hence the system was unstable. However, the heat flux through the walls drained energy from the mixing eddies, and after a suitable time a steady state would be set up in which the temperature

of the gas in the tube approached a constant value at any position.

In the previous cases, the system was always unsteady because no other energy or density transfer mechanism existed to offset losses from the open mouth of the tube.

4. THEORETICAL ANALYSIS

This chapter contains an analytical treatment of the buoyancy force and heat transfer models. Initially, a description of the mixing process in the brine solution model (stairwell problem) is given in order that the reader gets an insight into the dynamics of the flow. Then the one-dimensional turbulent diffusion equation is derived for this system. Its derivation relies heavily on dimensional analysis that takes the observed mixing phenomena into consideration. Solutions of the diffusion equation are found for the basic vertical duct problem, the stairwell-corridor system, and the stairwell-basement system. Results are derived that can be applied directly to the small scale models.

Formulation of the heat transfer model is an extension of the buoyancy model. The solution of this problem describes the effects of the heat transfer on the system.

4.1 A Description of the Mixing Phenomena in the Brine Solution Model (Stairwell)

The remarkable phenomenon observed in the experimental work was the intense mixing which lasted long after major density differences had died out. Figure 4.1 is a photograph showing the structure of the turbulence midway up the tube for the situation shown schematically in Fig. 3.1. Salt-water mixtures and tap water (containing dye to help visualize the mixing phenomena) were used to produce the buoyancy forces in this model. The photograph shows dark (less dense) solution propagating up the tube and the clear (dense) solution moving down the tube.

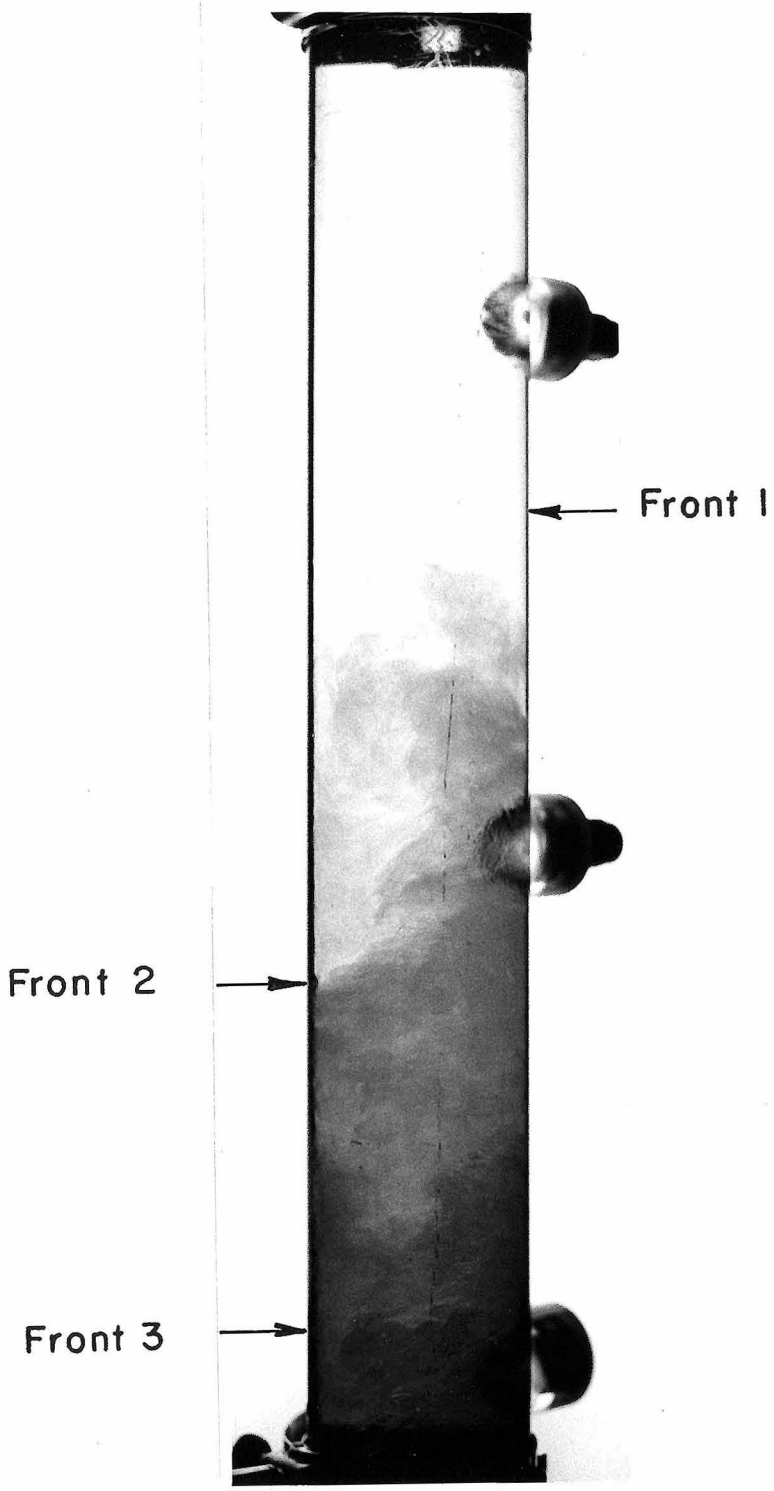

Fig. 4.1 Turbulent Mixing in Brine Solution Model Midway Up the Vertical Tube.

After the removal of the partition separating the two fluids, a distinct interface or front could be seen propagating up the tube. On the lower side of the front there was intense mixing, and on the upper side the brine solution was observed to be undisturbed. The propagation of this interface was not steady. Its movement consisted of intermittent bursts of high speed followed by periods of almost no motion. Initially the average speed of the front and the density gradient near the front were large. However, as the front traveled up the tube, its density gradient and its speed decreased until another stronger front penetrated it. The initial front was always followed by a series of stronger fronts, as shown in Fig. 4.1. The series of fronts move up the tube and pass the initial front. Later, they pass through each other. This is shown more explicitly in Figs. 4.2 and 4.3, which are a sequence of photographs of the front before it reaches the top of the duct.

Figure 4.2 depicts the mixing phenomena near the inlet of the tube. The arrows on the photographs show the various fronts. The sequence of photographs may be explained in the following manner.

A) The density of the initial front has increased (because of its light color) and a less dense (darker) front has formed about one diameter below it.

B) The second, stronger front in A has penetrated the original front. Still another front is about $1\frac{1}{2}$ diameters below it.

C) and D) The fronts are very dense in these sequences.

E) The density of the previous fronts has increased and

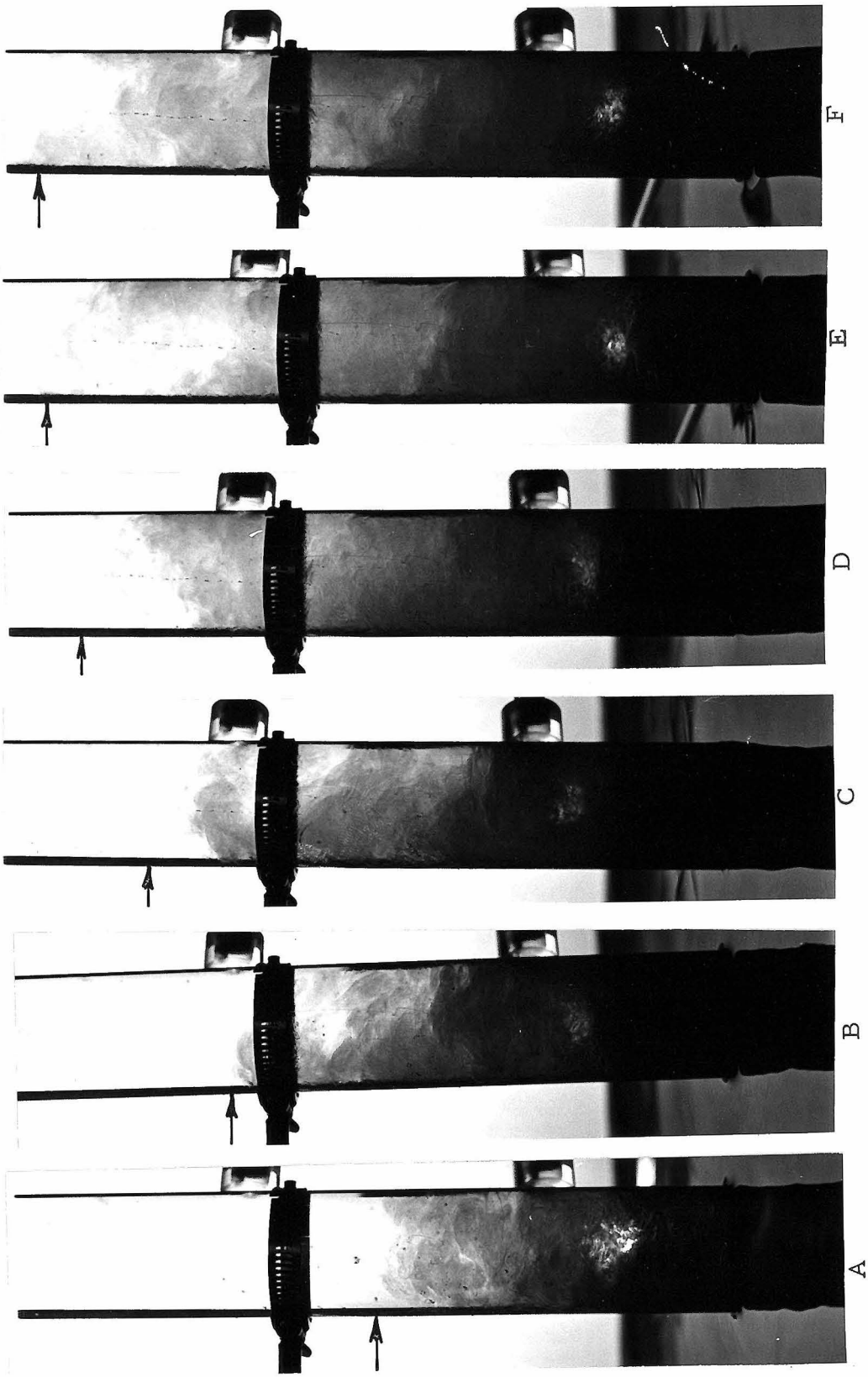

Fig. 4.2 Turbulent Mixing in the Brine Solution Model near the Inlet of the Vertical Tubes. (Sequence of Photographs).

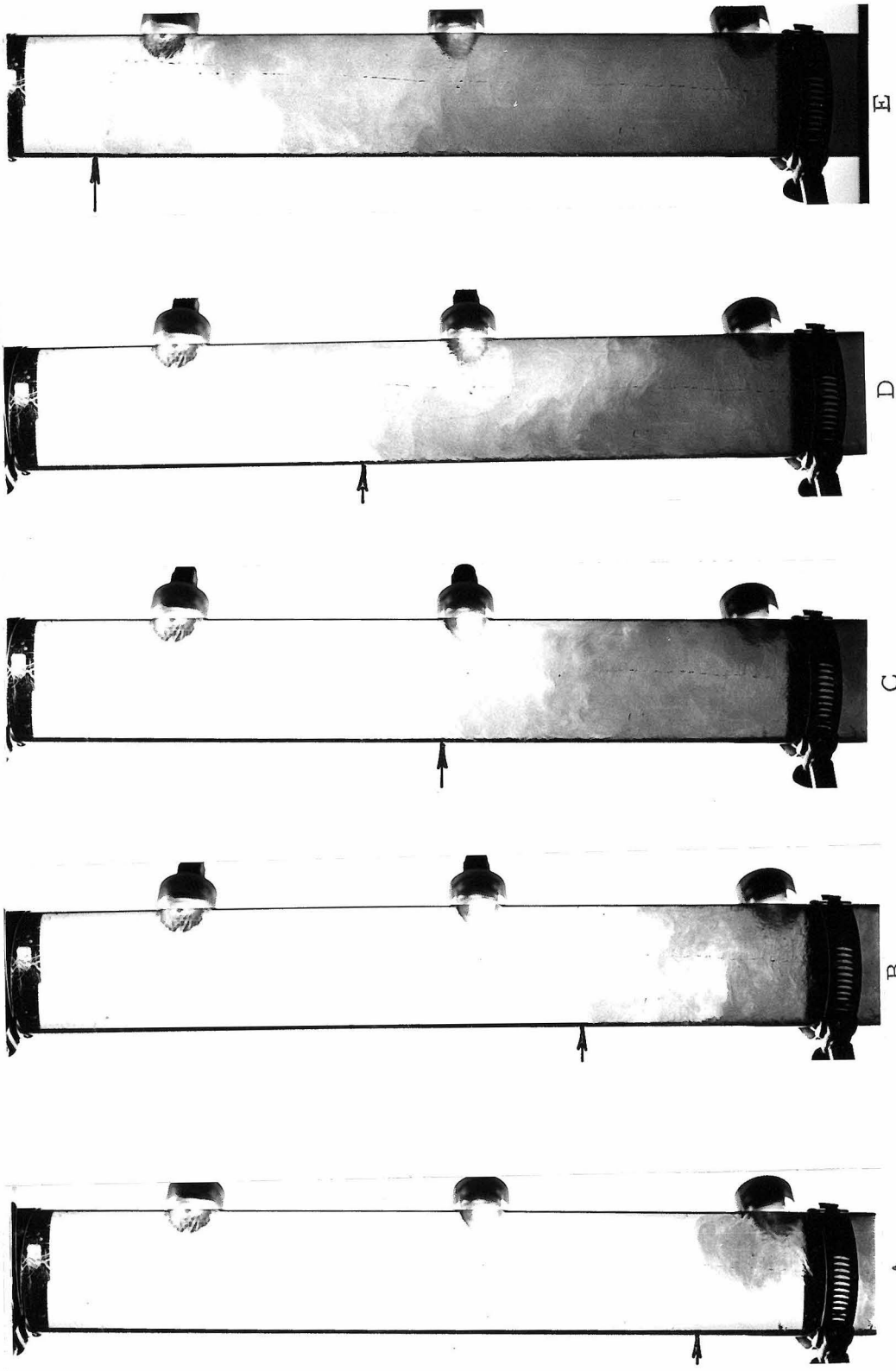

Fig. 4.3 Turbulent Mixing in the Brine Solution Model Midway Up the Vertical Tubes (Sequence of Photographs).

a new distinct front is about 3 diameters below the uppermost front.

F) Same as above.

The above photographs show how the fronts of less dense solution mix with the more dense brine solution and, hence, decrease the density gradient between the front and the fluid above it. Also, the manner in which the front propagates up the tube is shown. For example, in Frame B, the solution is not uniform across the tube. The dense (light colored) solution goes down the right hand side of the tube, while the less dense (dark colored) solution goes up the left side. The sequence of photographs (taken midway up the tube) in Fig. 4.3 also depicts this mechanism. Rather than propagating up or down a side, the solution spirals in all directions. The spiralling motion is random and very turbulent. The largest eddies at each cross section were roughly the size of the diameter of the tube.

All of the above photographs were taken before the fronts reached the top of the tube. We pointed out in Chapter 3 that the mixing was turbulent everywhere in the duct after the front reached the end of the tube. However, the same mixing mechanism (described in the above paragraph) continued throughout the tube until the density stratification in the tube was reduced to zero. Figure 4.4 is a typical concentration record at a point near the top of the duct that shows the pulse-type motion. In this example, the wave-like fronts are easily seen on the concentration record. They are well-defined here because this example had a large initial value of $\frac{\Delta\rho}{\rho} g$ and a very small L/d. Systems with these characteristics have well-defined fronts reaching

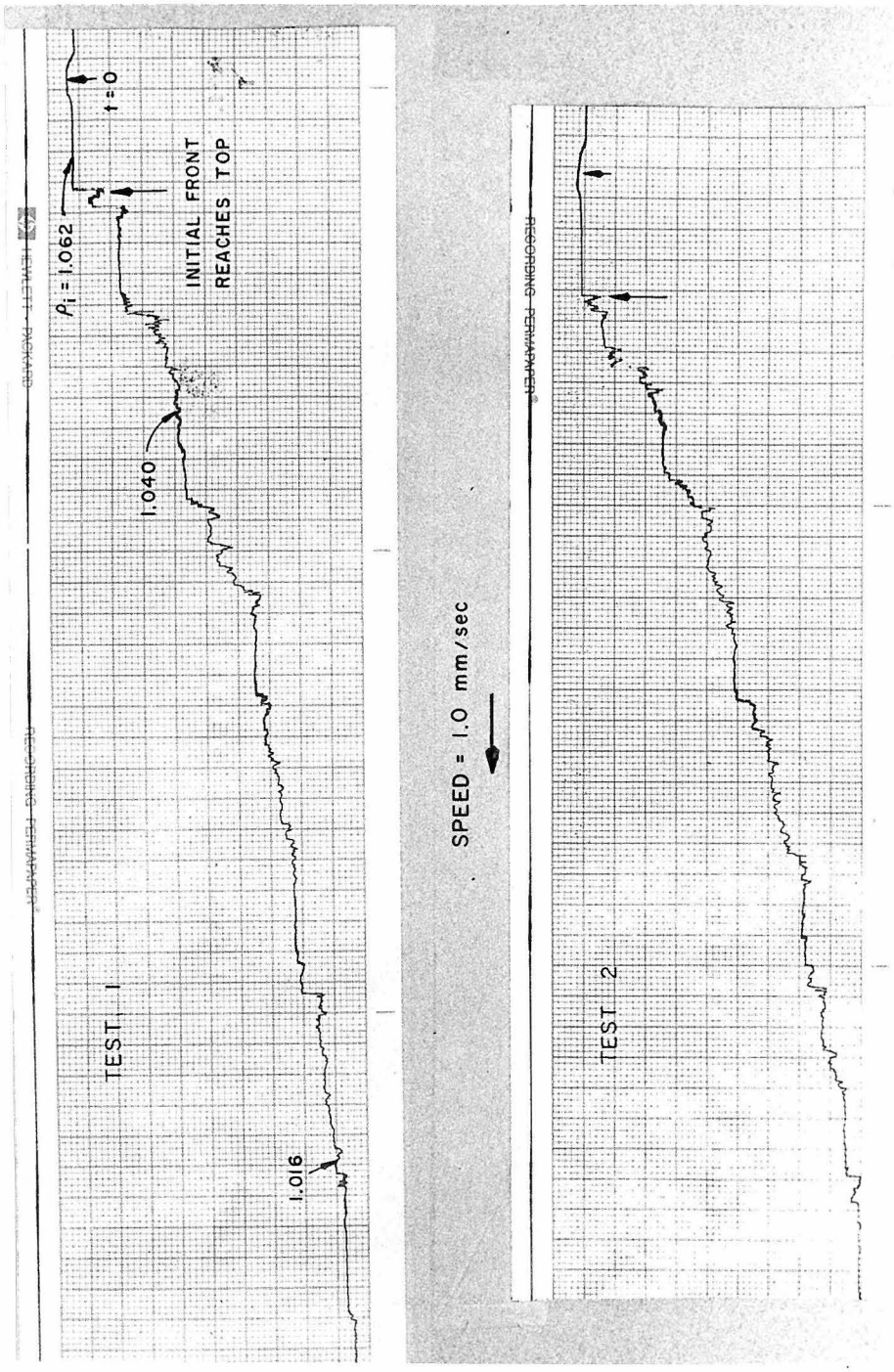

Fig. 4.4 A Typical Concentration-Time Record for Conductivity Probes Located Near the Top of the Vertical Tubes ($L/d \leq 8$).

the top of the tube. In tubes with smaller initial density differences and large L/d, the fronts are not as distinguishable and a much more smooth concentration record is obtained.

While the mixing process described above was occurring, the diluted brine solution could be seen leaving the bottom or inlet of the duct more or less on its centerline. Tap water entered the tube near its surface in a somewhat spiralling motion. Photographs of this phenomenon are shown in Fig. 4.5, for which the heavy brine solution was colored with dye. The heavier solution leaving the tube fell to the floor of the tank containing the low-density fluid as a turbulent plume and spread along the floor of the tank as a density current. In analyzing the mixing process, we will assume that the density at the exit is the ambient fluid density. From these photographs, it is clear that this assumption is not exact.

In the gas - gas experiments of the buoyancy force model and the experiments in the heat transfer model, the mixing phenomena were not visible as in the above case. However, smoke was introduced into the mouth of the tube in the gas - gas experiments, and although the smoke could not be seen propagating to the top of the tube, the mixing (when visible) was very turbulent. The same spiralling motion and motion near the inlet were observed as in the brine solution model. In the heat transfer experiments, dense fog was observed at the inlet of the tube. It revealed the flow to be very turbulent, as in the other cases. Hence, the visual observations indicated that all three cases produced the same general type of motion.

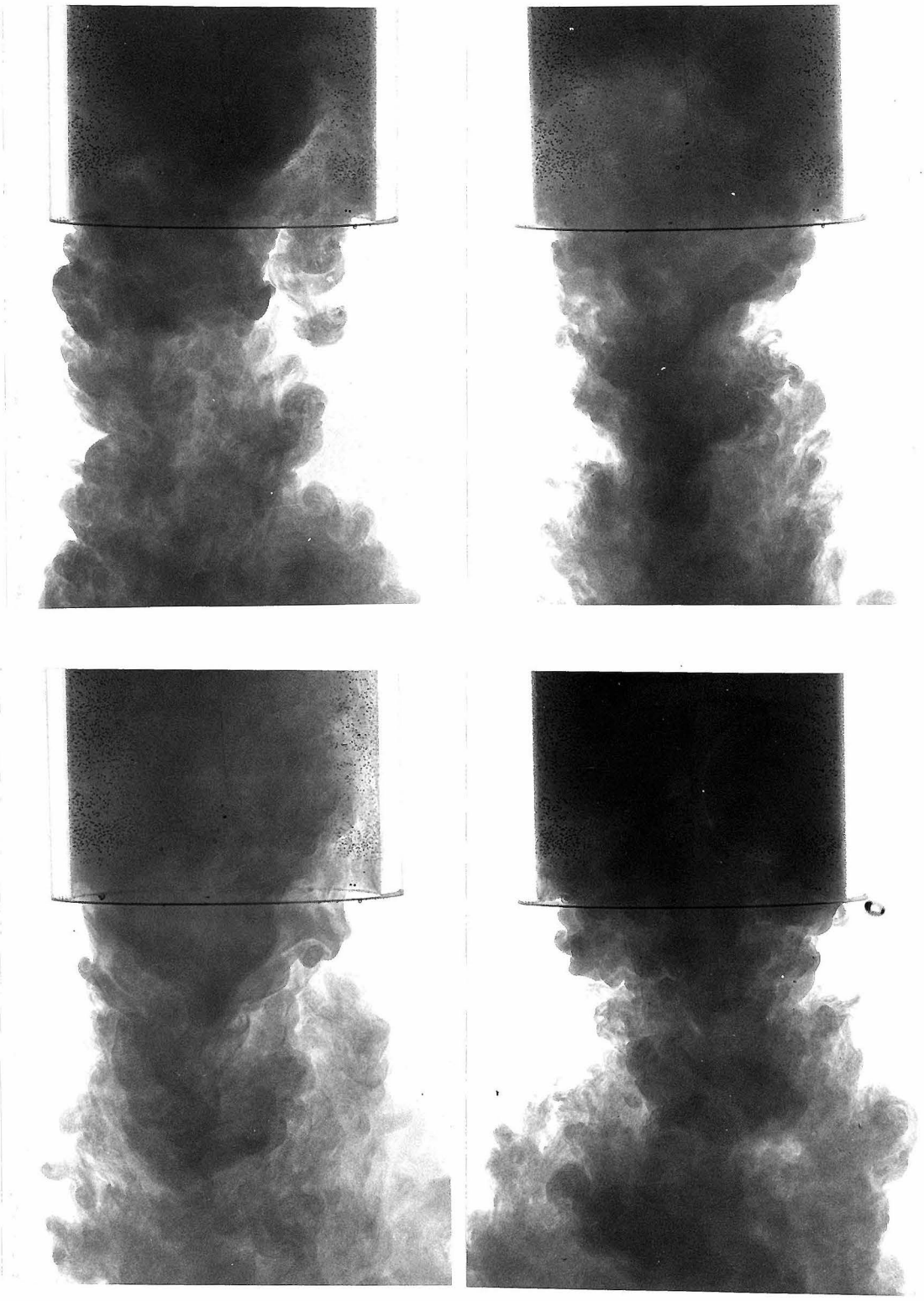

Fig. 4.5 Mixing Phenomena at the Inlet of Tubes in the Brine Solution Model.

4.2 Buoyancy Force Model

This section consists chiefly of three parts. Initially, the conservation equations are stated for a system in general. Then they are applied to the model under investigation and a diffusion coefficient is derived based on simple energy arguments and dimensional analysis. The turbulent diffusion equation derived from this analysis is then solved for the basic vertical duct discharging a dense solution into an infinite environment of less dense solution. The stairwell-corridor and stairwell-basement problems are just extensions of the vertical duct problem. They are solved by making assumptions that change the boundary conditions of the vertical duct problem. The resulting solutions have the same form as that of the basic separation of variables solution of the stairwell problem.

The model equations derived here are based on the assumptions that viscosity and molecular diffusion are not important. These assumptions are in part justified by the discussion in Section 3.1 and the description of turbulence given in Section 4.1.

4.2.1 The Turbulent Diffusion Equation. Consider fluid flowing through a control volume as shown in Fig. 4.6. If the fluid is homogeneous, the continuity equation is

$$\frac{\partial \rho}{\partial t} + \nabla \cdot (\rho \underline{v}) = 0 \qquad (4.1)$$

where $\underline{v}$ is the velocity vector. The velocities in this analysis are purely kinematic and are not weighted averages as those computed from a momentum flux balance. That is, the velocities are based on the distance a particle travels and the time elapsed during this flow period, which makes their values independent of the mass of the particles.

If there is a foreign substance in the fluid, as dissolved salts in water, then there is an additional transfer of mass across the control volume due to molecular diffusion of the salt through the water. Therefore, an additional mass transfer term must be added to the continuity equation if the fluid is nonhomogeneous. That is,

$$\frac{\partial \rho}{\partial t} + \nabla \cdot (\rho \underline{v}) = \nabla \cdot (D \nabla c) \qquad (4.2)$$

where D is the molecular diffusion coefficient and c is the concentration of the dissolved salt. In this same example, the equation for conservation of mass of the dissolved salt is

$$\frac{\partial c}{\partial t} + \nabla \cdot (c \underline{v}) = \nabla \cdot (D \nabla c) , \qquad (4.3)$$

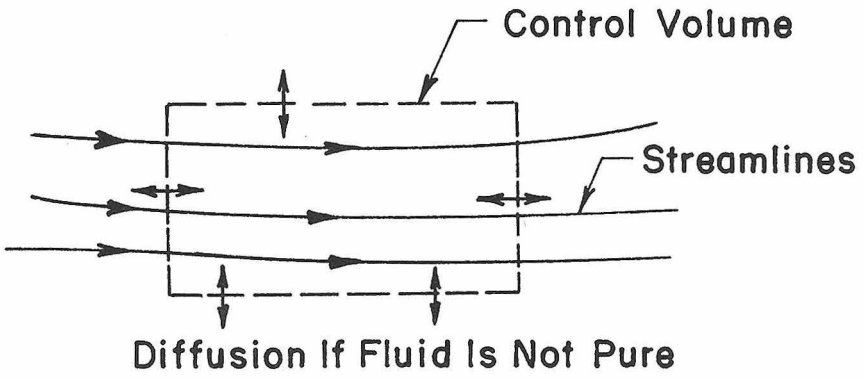

Fig. 4.6 Definition Sketch of Fluid Flowing through a Control Volume.

where ∇ is the gradient operator. To complete the conservation equations, the density must be related to the concentration of the salt. The relation has the form, determined empirically,

$$\rho - \rho_o = \beta (c - c_o) \qquad (4.4)$$

where ρ_o is the density of water in this case and β is a constant.

Although reference was made to dissolved salts as being the foreign substance which makes the fluid nonhomogeneous, the above conservation equations apply for the gas - gas experiments. In those experiments, the molecular weight (M) of the gas mixture is analogous to the concentration of salt in the solution. For instance, the density can be written as

$$\rho - \rho_o = \beta'(M - M_a) , \tag{4.5}$$

where ρ_o is the density of air and β' is a constant. Since (4.5) is the equation of state for a perfect gas, β' has the form

$$\beta' = P/R_o T .$$

The turbulent diffusion equation can be derived by making the following substitutions into the conservation equations: $\rho = \overline{\rho} + \rho'$, $c = \overline{c} + c'$, $\underline{v} = \underline{v}'$, where $\overline{\rho}$ and $\overline{c}$ are time-averaged quantities and ρ', c', and $\underline{v}'$ are deviations from the corresponding mean values. Note that $\overline{\underline{v}}$ has been assumed to be zero in this analysis. This assumption arises from the fact that the net volume flux of solution at any cross section in the tube is zero. The velocities in this analysis are based on the volume flux of solution in the duct and are independent of any particular species present in the solution. However, this assumption is not valid when the shaft is tilted from its vertical position because a two-layered flow system may develop. Therefore, these equations apply only for the vertical duct system, and also $\overline{\underline{v}}$ must be included in the case of an inclined shaft.

In this analysis, we are concerned only with the mode of density change along the central axis of the tube. Therefore, the one-dimensional diffusion equation will be used because the large scale

mixing rates are a function of the density gradient based on the average density at any cross section in the tube. Hence, we are assuming that the cross-sectional variation of the density is not important.

Therefore, after substitution of the above quantities into Eqs. (4.2) and (4.3) and using Reynolds' averaging techniques, the conservation equations become (in one dimension)

$$\frac{\partial \bar{\rho}}{\partial t} + \frac{\partial}{\partial z}\left(\overline{\rho' v'}\right) = \frac{\partial}{\partial z}\left(D \frac{\partial \bar{c}}{\partial z}\right) \tag{4.6}$$

and

$$\frac{\partial \bar{c}}{\partial t} + \frac{\partial}{\partial z}\left(\overline{c' v'}\right) = \frac{\partial}{\partial z}\left(D \frac{\partial \bar{c}}{\partial z}\right) \tag{4.7}$$

where $\overline{\rho' v'}$ and $\overline{c' v'}$ represent the turbulent mass flux per unit area of the solution and solute, respectively. Using Reynolds' mixing analogy, the turbulent mass fluxes may be written as

$$\overline{\rho' \underline{v}'} = -E_z \frac{\partial \bar{\rho}}{\partial z} \quad , \tag{4.8}$$

$$\overline{c' \underline{v}'} = -E_z \frac{\partial \bar{c}}{\partial z} \quad , \tag{4.9}$$

where E_z is the turbulent mixing coefficient. Since the turbulent transport of energy and momentum are dominant, the molecular diffusion terms can be neglected. This assumption makes (4.6) and (4.7) equivalent because of the relation between ρ and c in (4.4). Therefore, only (4.6) will be used to derive the turbulent diffusion equation. After substitution of (4.8) into (4.6) the diffusion equation has the form

$$\frac{\partial \bar{\rho}}{\partial t} = \frac{\partial}{\partial z}\left(E_z \frac{\partial \bar{\rho}}{\partial z}\right) \quad . \tag{4.10}$$

For simplicity, the bars above ρ and c will be omitted. Whenever they are used it is understood that they are time-averaged and cross-sectional averaged quantities.

Consider the parcels of fluid in a tube as shown in Fig. 4.7, where $\rho_1 > \rho_2$. Since the parcels exist in an unstable environment,

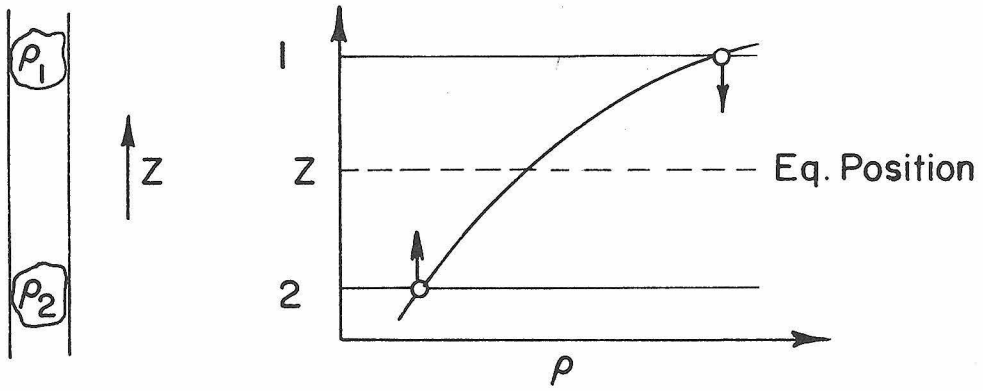

Fig. 4.7 Definition Sketch of an Unstable Density Field.

the rate at which they mix or approach each other depends on their separation and the magnitude of the density differences. As time progresses, the magnitude of the density difference decreases as a result of the mixing, and the diffusion coefficient should decrease also. From dimensional analysis the diffusion coefficient is expected to be of the form

$$E_z \sim w'\lambda \ , \qquad (4.11)$$

where λ is a characteristic length and w' is a velocity fluctuation. As stated above, $w' = f(\partial\rho/\partial z)$ and a simple form for the function may be found from energy arguments. A schematic is shown in Fig. 4.8 which consists of a stratified system that is unstable in its initial state and stable in its final state. The potential energy (P.E.) of state (1) is converted into P.E. of a corresponding stable density field and kinetic energy (K.E.) of state (2). The energy equation is as follows:

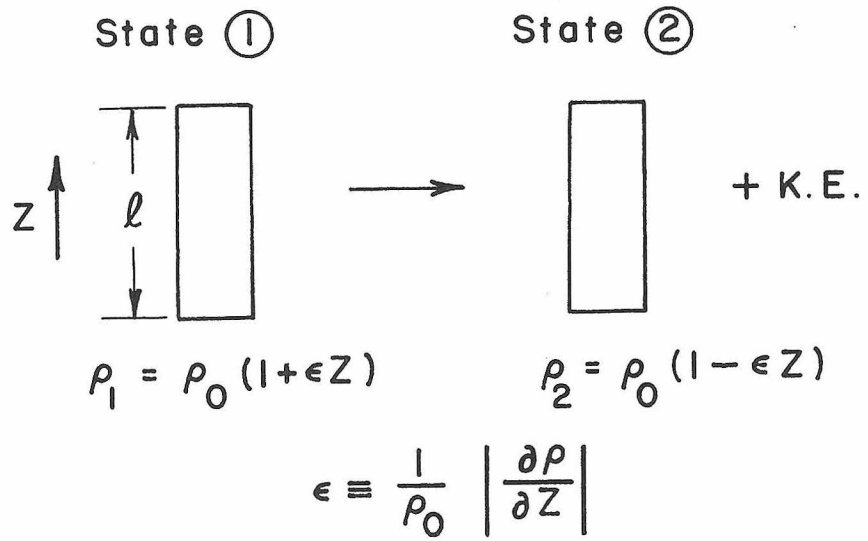

Fig. 4.8 Definition Sketch of the Conversion of Energy from an Unstable System to a Stable System.

$$\text{P.E.})_1 = \text{P.E.})_2 + \text{K.E.} \tag{4.12}$$

The potential energy for the system in Fig. 4.8 can be written as follows:

$$\frac{\text{P.E.}}{\text{area}} = \int_0^{\ell} (\rho g)\, z\, dz \ . \tag{4.13}$$

Substituting (4.13) into the energy equation (4.12) yields

$$\frac{\text{K.E.}}{\text{area}} = \int_0^{\ell} (\rho_1 - \rho_2)\, g\, z\, dz \ .$$

After integration the kinetic energy becomes

$$\frac{\text{K.E.}}{\text{area}} = \frac{2}{3}\rho_o g \epsilon \ell^3 \ . \tag{4.14}$$

The kinetic energy is usually written as

$$\text{K.E./area} = \tfrac{1}{2}\rho w'^2 \ell \ . \tag{4.15}$$

Thus, combining (4.14) and (4.15) yields

$$w' \sim \sqrt{\frac{g}{\rho}\frac{\partial \rho}{\partial z}\ell^2} \ ,$$

and hence

$$E_z \sim \sqrt{\frac{g}{\rho}\frac{\partial \rho}{\partial z}\ell^2}\ \lambda\ .$$

A priori, the logical choice for λ and ℓ is the diameter, d, which is the largest characteristic size of the mixing eddies. However, observations made during these experiments indicate that there is some other length scale that controls the distance a front propagates before being dampened due to the mixing. The experimental results indicate that ℓ^2 is of the order of $d\sqrt{dL}$ and λ is of the order of d, where L is the tube's length. Therefore, the diffusion coefficient will be defined as

$$E_z \equiv k\sqrt{\frac{g}{\rho_a}\frac{\partial \rho}{\partial z}}\ (d^7 L)^{1/4}\ , \qquad (4.16)$$

where k is an empirical diffusion constant. Substitution of (4.16) into the diffusion equation (4.11) yields

$$\frac{\partial \rho}{\partial t} = k\sqrt{\frac{g}{\rho_a}}\ (d^7 L)^{1/4}\frac{\partial}{\partial z}\left(\frac{\partial \rho}{\partial z}\right)^{3/2}\ . \qquad (4.17)$$

The diffusion equation can be normalized by making the following substitutions: $z \equiv XL$, $\Delta\rho \equiv \rho - \rho_a$, $\Delta\rho_i \equiv \rho_i - \rho_a$, $\theta = \Delta\rho/\Delta\rho_i$, and

$$\tau \equiv \sqrt{\left(\frac{\Delta\rho_i}{\rho_a}\right)\frac{g}{d}}\left(\frac{d}{L}\right)^{9/4} t\ . \qquad (4.18)$$

After normalization the turbulent diffusion equation is

$$\frac{\partial \theta}{\partial \tau} = k\frac{\partial}{\partial x}\left(\frac{\partial \theta}{\partial x}\right)^{3/2}\ . \qquad (4.19)$$

This equation resembles the ordinary diffusion or heat transfer equation with a coefficient which in this case is $\sqrt{\partial\theta/\partial x}$. For nonlinear equations of this type, one expects (e. g., ref. 9) to get the wave-like

fronts as shown in Figs. 4.1.

Note that in obtaining equation (4.16) we use $\frac{1}{\rho_a}\frac{\partial \rho}{\partial x}$ rather than $\frac{1}{\rho}\frac{\partial \rho}{\partial x}$ in the expression for the diffusion coefficient. For the water - salt water example for which $\Delta\rho/\rho_a$ is never larger than 0.15, this simplification is justified. For cases where $\Delta\rho \gg \rho_a$, further justifications may be necessary. The change was made primarily because it greatly simplified the analysis, and we were interested in obtaining a simple model.

4.2.2 Stairwell (Vertical Duct). The stairwell model consists of diffusion controlled by an unstable density field. The above observations (Section 4.1) suggest that two phases exist. They are: (1) the time during which the initial front propagates to the top of the tube, $0 \leq \tau \leq \tau_o$; and (2) the time during which the mixing process exists throughout the whole tube, $\tau > \tau_o$. The latter phase will be considered first in the following analysis.

4.2.2.1 Separation of variables solution, $\tau \geq \tau_o$. Previously, we pointed out that turbulent mixing exists throughout the tube after the initial front has arrived at its top boundary. Formulation of the mathematical model begins at this point in time. That is, at some time, τ_o (which is the arrival time of the front), an unstable density stratification exists throughout the tube. The density at the top of the tube decreases with time and is always a maximum there. Also, the density at the inlet of the tube is approximately equal to the ambient value, which is always less than the density at any point in the tube.

The bottom boundary condition fixes the buoyancy in this model. As long as the density at the bottom of the tube is less than

that at the top boundary, unstable buoyancy forces exist which account for the mixing. The mathematical formulation of the boundary conditions includes: (1) no mass flux across the tube's upper boundary; and (2) the ambient density is constant at the inlet of the tube, i. e.,

$$\frac{\partial\theta}{\partial x} = 0 \quad \text{at} \quad x = 1 \tag{4.20}$$

and

$$\theta = 0 \quad \text{at} \quad x = 0 \ , \tag{4.21}$$

for all τ.

In addition, the initial distribution of θ, i. e., $\theta\{x, \tau=\tau_o\}$, must be specified to complete the boundary conditions. Since we can not solve the initial transient problem ($0 \leq \tau \leq \tau_o$), we do not know a priori what distribution $\theta\{x, \tau_o\}$ to use.

We can approach the problem in an approximate manner and find a solution for a particular initial distribution. This initial distribution will be found as part of our solution process and will later be shown to be very close to the experimental value.

The form of the solution is indicated by the form of Eq. (4. 19) which suggests that a separation of variable technique may be possible. We try:

$$\theta = H(\tau)F(x) \ , \tag{4.22}$$

where $H(\tau)$ can be thought of as the normalized density at the top of the tube and $F(x)$ as the density distribution present at $\tau = \tau_o$, which will remain constant throughout the test. The boundary and initial conditions now become

$$dF/dx = 0 \quad \text{at} \quad x = 1 \ , \tag{4.23}$$

$$F = 0 \quad \text{at} \quad x = 0 \ , \tag{4.24}$$

$$F = 1 \qquad \text{at} \qquad x = 1 \ , \tag{4.25}$$

and $$H = 1 \qquad \text{at} \qquad \tau = \tau_o \ . \tag{4.26}$$

The boundary conditions (4.24) and (4.25) normalize but do not specify $F\{x\}$.

Substituting θ, (4.22), in the diffusion equation, (4.18), and simplifying yields

$$\frac{\dot{H}}{H^{3/2}} = \left(\frac{3}{2}k\right)\frac{\dot{F}^{1/2}\ddot{F}}{F} = -\alpha \ , \tag{4.27}$$

where α is a positive constant obtained from the equality of both sides of the equation. Solving for H gives

$$H = \frac{4}{\left[\alpha(\tau-\tau_o)+A\right]^2}$$

where A is the constant of integration. The condition $H = 1$ at $\tau = \tau_o$ implies that $A = 2$ and therefore gives

$$H = \frac{1}{\left[\frac{\alpha}{2}(\tau-\tau_o)+1\right]^2} \ . \tag{4.28}$$

We must now solve for F from the equation

$$\frac{3}{2}k\dot{F}^{\frac{1}{2}}\ddot{F}/F = -\alpha \ .$$

If we let $P = \dot{F}$, then $P^{3/2}dP = -\frac{2}{3}\frac{\alpha}{k}FdF$, and the first integration gives $dF/dx = \left[-\frac{5}{6}\frac{\alpha}{k}F^2 + B\right]^{2/5}$ where B is the constant of integration. The conditions $F = 1$ and $\dot{F} = 0$ at $x = 1$ imply that $B = \frac{5}{6}\frac{\alpha}{k}$. Thus, the equation becomes

$$\frac{dF}{dx} = \left(\frac{5}{6}\frac{\alpha}{k}\right)^{2/5}(1-F^2)^{2/5} \ . \tag{4.29}$$

The quantity $\left(\frac{5}{6}\frac{\alpha}{k}\right)^{2/5}$ may be found by integrating (4.29) from $x = 0$ to $x = 1$. Thus, if $F \equiv \sin\theta$,

$$\left(\frac{5}{6}\frac{\alpha}{k}\right)^{2/5} = \int_0^{\pi/2} \cos^{1/5}\theta \, d\theta \quad . \tag{4.30}$$

The integral in (4.30) can be written in the form

$$\int_0^{\pi/2} \cos^{1/5}\theta d\theta = \frac{\sqrt{\pi}}{2} \frac{\Gamma\left(\frac{6}{10}\right)}{\Gamma\left(\frac{11}{10}\right)} \tag{4.31}$$

where Γ is the gamma function. Combining (4.30) and (4.31) and substituting the appropriate values for Γ gives

$$\left(\frac{5}{6}\frac{\alpha}{k}\right)^{2/5} = 1.3872 \quad . \tag{4.32}$$

We can now integrate (4.29) for this particular value of α. The equation can be rewritten as

$$\frac{dF}{dx} = 1.3872(1-F^2)^{2/5} \qquad 0 \le x \le 1 \tag{4.33}$$

with the boundary condition $F = 0$ at $x = 0$. This equation was solved numerically to obtain the particular function $F\{x\}$ which corresponds to the value of α given in (4.32).

The Adams-Moulton predictor-corrector method was used to solve numerically for $F\{x\}$. The fourth-order Runge-Kutta method was used to obtain the starting values and also when the step size was changed. The solution is shown in Fig. 4.9. The values of F are closely approximated by

$$F = \left[1 - (1-x)^{3/2}\right] .$$

Note that the diffusion constant, k, and the arrival time of the front, τ_o, may be found empirically now. The solution to the diffusion equation for θ at $x = 1$ can be written as follows:

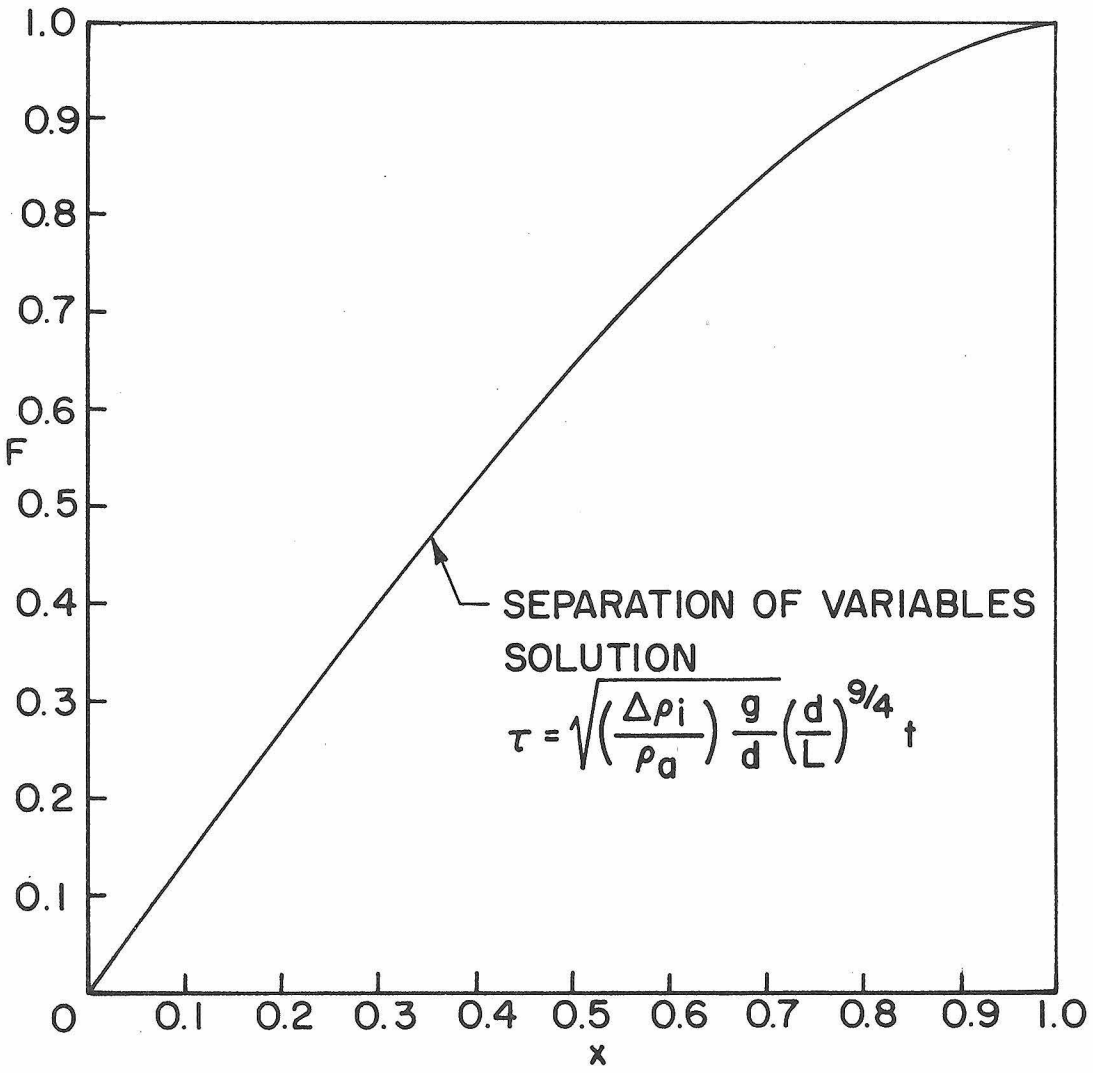

Fig. 4.9 Theoretical Density Distribution of the Separation of Variables Solution for $\tau \geq \tau_o$.

$$\sqrt{\frac{1}{\theta}}\Bigg|_{x=1} \equiv \sqrt{\frac{\overline{\Delta\rho_i}}{\Delta\rho}}\Bigg|_{x=1} = \left(\frac{\alpha}{2}\right)(\tau-\tau_o)+1 \quad . \tag{4.34}$$

If the experimental data are plotted in this manner, τ_o is the intercept of the abscissa and $(\alpha/2)$ is the slope of the linear plot. Then k may be found from (4.32), which can be simplified to give

$$k = .736(\alpha/2) \quad . \tag{4.35}$$

Equations (4.34) and (4.35) will be used when analyzing the experimental results in Chapter 6.

The solution to our problem is represented by Eqs. (4.22), (4.28), (4.32) and the integral of (4.33) for F(x) shown graphically in Fig. 4.9. What we have actually done is to solve Eq. (4.19) for the initial distribution $F\{x\} = \theta\{x, \tau_o\}$ and the conditions (4.20) and (4.21). Fortunately, as we will show later, $F\{x\}$ is a good representation of the experimentally observed distribution.

4.2.2.2 Initial time period, $\tau < \tau_o$. The separation of variables solution in the previous model was based on the premise that the initial front had reached the top boundary of the tube. We pointed out in Section 4.1 that the mixing mechanism subsequent to the arrival of the initial front appeared to be the same as that before its arrival. Based on observations of the mixing phenomena, it is reasonable to postulate that the propagation of the fronts prior to and after their arrival at the top boundary is dependent only on the local mixing in the tube. In essence, the propagation of the fronts is not influenced by the tube's length. However, the length of the tube, L, was used in the separation of variables solution first because a zero mass flux boundary condition was applied at z = L; and second be-

cause a factor $(L/d)^{1/4}$ was applied to the diffusion coefficient to successfully correlate the experimental results.

The first of these conditions does not apply here because we are interested in the propagation of the front up the tube before it reaches the end of the tube. If the second condition is generally correct, the diffusion coefficient should be rewritten as

$$E_z = k \sqrt{\frac{g}{\rho_a} \frac{\partial \rho}{\partial z}} \; (d^7 z_f)^{1/4} \quad . \tag{4.36}$$

Here, this expression is identical to (4.16) with z_f, the position of the front, substituted for the length scale L found in (4.16). The normalized equation is of the form:

$$\frac{\partial \theta}{\partial \tau'} = k \, (x_f')^{1/4} \, \frac{\partial}{\partial x'} \left(\frac{\partial \theta}{\partial x'} \right)^{3/2} \tag{4.37}$$

where

$$x_f' = z_f/d \quad , \quad x' = z/d \quad , \quad \text{and} \quad \tau' = \sqrt{(\Delta\rho_i/\rho_a)(g/d)}\, t \quad . \tag{4.38}$$

Solutions of (4.37) were sought using an integral technique based on the assumptions that

$$\begin{aligned} &\theta\{x', \tau'\} = \left[1 - (1 - x'\{\tau'\}/x_f'\{\tau'\})^2\right] , \\ &\theta\{x_f', \tau'\} = 1 \quad , \quad \text{and} \quad \frac{\partial \theta}{\partial x}\{x_f', \tau'\} = 0 \quad . \end{aligned} \tag{4.39}$$

Analysis is straightforward and leads to the result that x_f', the location of the front, propagates as $(\tau')^{4/9}$. As we shall show later, this is too weak a dependence; the experimental value is closer to $(\tau')^{0.6}$.

A second approach was also tried. This consisted of ignoring the additional factor of $(L/d)^{1/4}$ and looking for a self-similar solution for the equation

$$\frac{\partial \theta}{\partial \tau'} = k \frac{\partial}{\partial x'} \left(\frac{\partial \theta}{\partial x'} \right)^{3/2} \qquad (4.40)$$

with similar boundary conditions. The solution is again straightforward and the similarity parameter is found to have the form $x'/(\tau')^{0.4}$. Again, the dependence of x' on τ' is too weak.

Although neither approach leads to a good prediction, both suggest that z_f/d can be expressed as a function of

$$\tau' = \sqrt{\frac{\Delta\rho_i}{\rho_a} \frac{g}{d}}\, t \ .$$

Later, the experimental data show that this is true.

4.2.3 Stairwell-Corridor System. We pointed out in Chapter 2 (Section 2.1.3) that the mixing mechanism in the stairwell is altered if a long corridor is attached horizontally to the top of the tube. In this case, the dense fluid must flow from the horizontal attachment into the vertical portion of the tube and then into the less dense ambient fluid. However, if the fluid in the horizontal portion of the tube is assumed to be well mixed, the system can be modeled analytically. This assumption means that the corridor can be replaced by a volume of equal size and that less dense fluid entering the volume is mixed instantaneously and uniformly throughout it.

For the "well-mixed top," we assume that the change in mass of volume at the top of the tube is equal to its mass flux down the tube at that point. This assumption can be stated mathematically as follows:

$$-A_p E_z \frac{\partial \rho}{\partial z} = V_t \frac{\partial \rho}{\partial t} \qquad \text{at} \quad z = L \qquad (4.41)$$

where A_p is the cross-sectional area of the vertical duct and V_t is

the volume of the well-mixed top of the tube. This condition replaces the previous boundary condition, i.e., no mass flux across the top boundary used in the vertical tube system of Section 4.2.2.1. All of the rest of the system remains unchanged. Therefore, the system to be solved is as follows:

$$\frac{\partial\theta}{\partial\tau} = k\frac{\partial}{\partial x}\left(\frac{\partial\theta}{\partial x}\right)^{3/2} \qquad \tau \geq \tau_o \ ,$$

$$-V_r k\left(\frac{\partial\theta}{\partial x}\right)^{3/2} = \frac{\partial\theta}{\partial\tau} \qquad \text{at} \quad x = 1 \ , \tag{4.42}$$

$$\theta = 0 \ \text{ at } \ x = 0 \ , \quad \theta = \theta(x) \ \text{ at } \ \tau = \tau_o \ , \ \text{and} \ \ V_r = \frac{A_p L}{V_t}$$

where V_r is the ratio of the volume of the vertical duct to the volume of the upper horizontal tube. Here, the boundary condition at the top of the tube, $x = 1$, and the rest of the system have been normalized as before.

The solution to this problem is carried out in a manner very similar to the separation of variables solution of the stairwell model. That is, $\theta = F(x)H(\tau)$ where

$$H = \frac{1}{\left[\frac{\alpha}{2}(\tau-\tau_o) + 1\right]^2}$$

and

$$\frac{dF}{dx} = \left(\frac{5}{6}\frac{\alpha}{k}\right)^{2/5}(C-F^2)^{2/5} \ .$$

C is a constant of integration. The density ranges from $F = 0$ at $x = 0$ to $F = 1$ at $x = 1$, as before. Applying the top boundary condition, (4.42) yields

$$\dot{F}^{3/2}\Big|_{x=1} = \left(\frac{\alpha}{k}\right)\frac{1}{V_r} \ . \tag{4.43}$$

Since $F(1) = 1$, the constant of integration, C, can be found by com-

bining the above equations for $\dot{F}(1)$. Therefore,

$$C = \frac{\frac{6}{5}\left(\frac{\alpha}{k}\right)^{2/3}}{V_r^{5/3}} + 1 ,$$

and $\dot{F}$ becomes

$$\frac{dF}{dx} = \left(\frac{5}{6}\frac{\alpha}{k}\right)^{2/5}\left[\frac{6}{5}\frac{\left(\frac{\alpha}{k}\right)^{2/3}}{V_r^{5/3}} + 1 - F^2\right]^{2/5} . \qquad (4.44)$$

If the volume of the stairwell >> volume of the top, $V_r \to \infty$, then the differential equation, (4.44), reduces to the stairwell system with no mass flux across the top boundary. The above differential equation with the boundary conditions $F(0) = 0$ and $F(1) = 1$ was solved numerically using standard shooting methods. For example, (α/k) is initially estimated and the numerical integration starts with $F = 0$ at $x = 0$. The integration continues until $x = 1$. Now, if $F = 1$ at this point, then the initial value of (α/k) is correct. If not, (α/k) is re-estimated and the method is repeated until the top boundary condition is satisfied. The Runge-Kutta integration scheme was used to carry out the integration in this analysis. The results are plotted in Figs. 4.10 and 4.11.

Figure 4.10 shows the relationship between α and V_r. Since the density decreases according to the relation

$$\Delta\rho \sim \frac{\Delta\rho_i}{\left[\frac{\alpha}{2}(\tau-\tau_o)+1\right]^2} ,$$

smaller values of α imply that the mixing process is slower. α/k ranges from 2.72, $(V_{shaft} \gg V_{top})$, to 0, $(V_{shaft} \ll V_{top})$. Therefore, a larger volume on top will take a longer time to empty itself

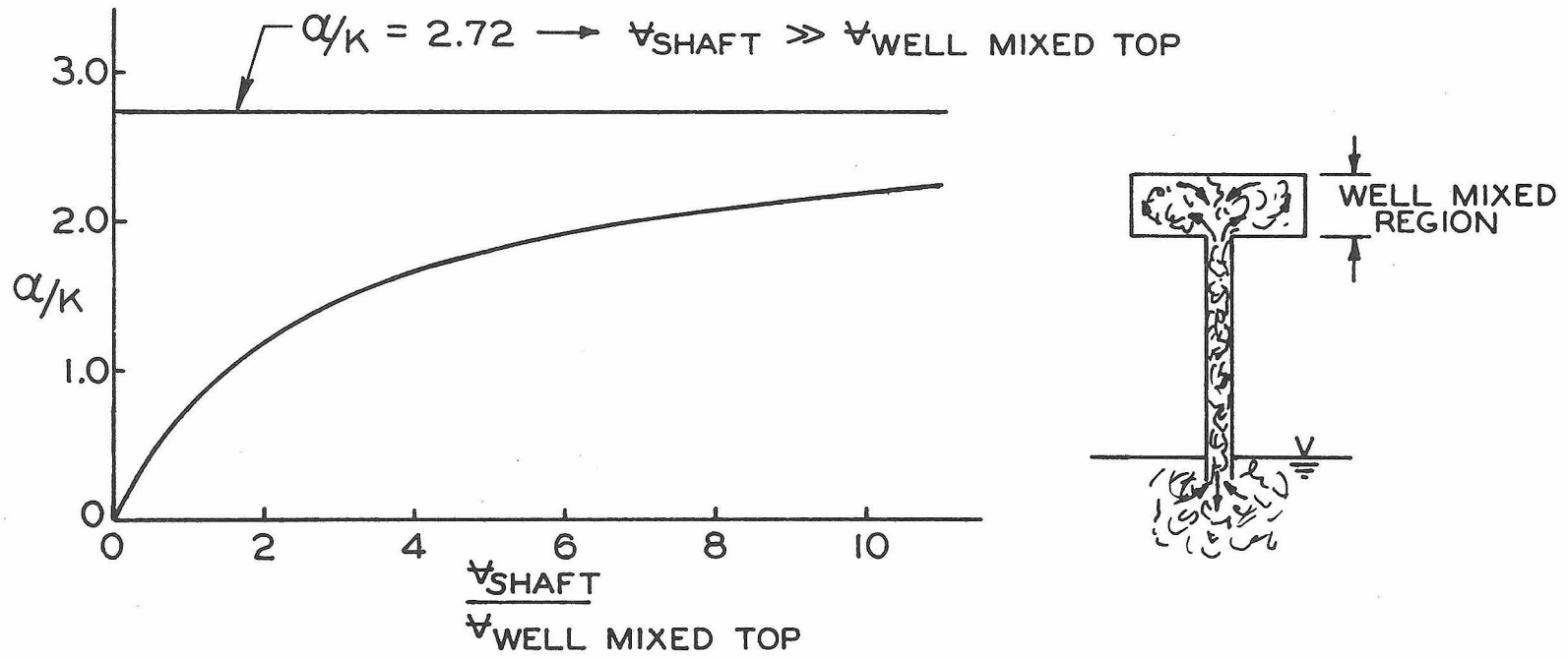

Fig. 4.10 Variation of α/k with Volume Ratio for the "Well-Mixed Top" Boundary Condition.

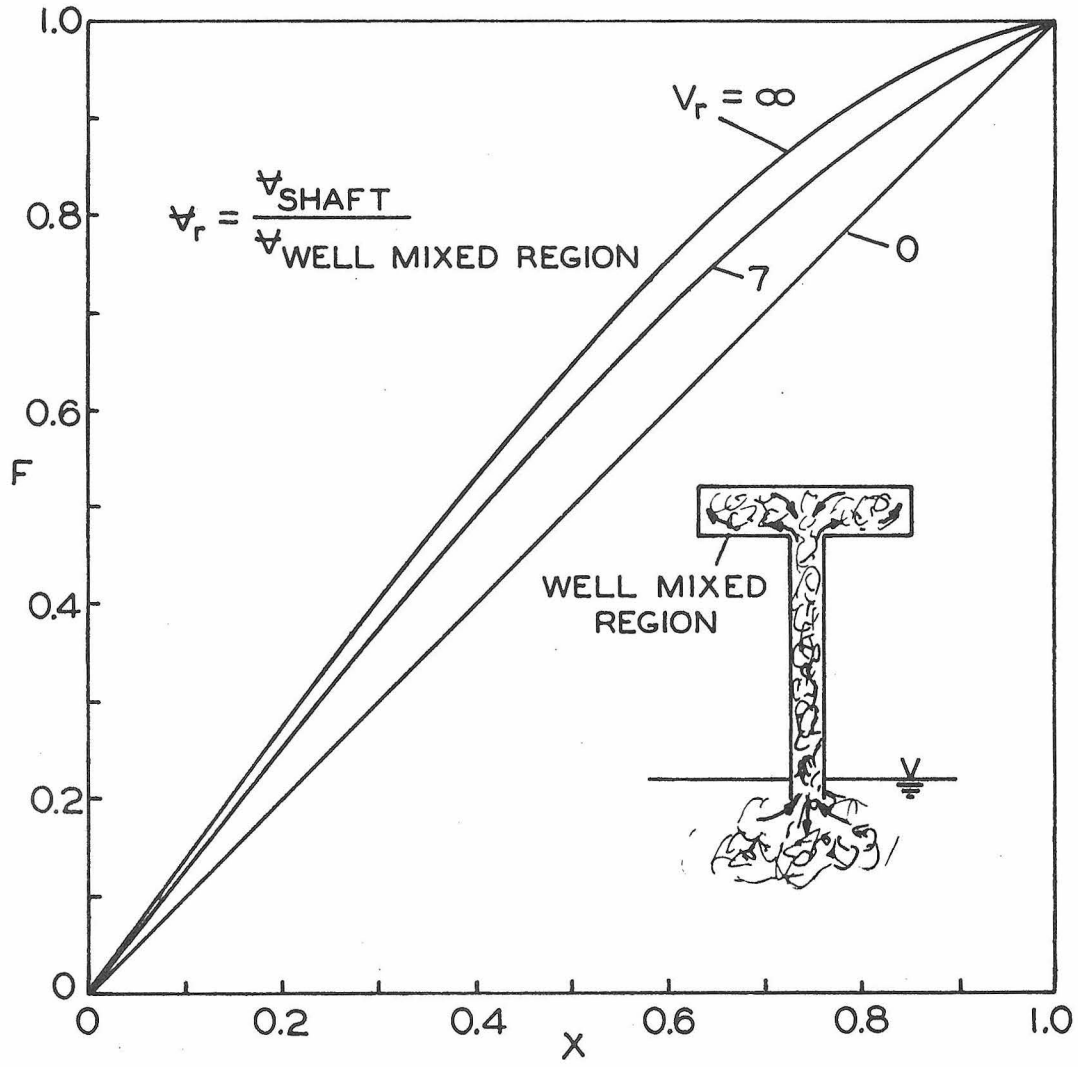

Fig. 4.11 Density Profiles for the "Well-Mixed Top" Boundary Condition.

as one would expect. The corresponding density profiles, F(x), are shown in Fig. 4.11. The extremes are no top volume, for which $V_r = \infty$ and mass flux = 0 at the top, and an infinite top volume, for which $V_r = 0$ and the density profile is linear. The function F(x) does not change very much from the stairwell model.

4.2.4 Stairwell-Basement System. The stairwell-basement system (Section 2.1.4) is just a modification of the vertical duct problem. Instead of a dense solution discharging from the duct into an infinite environment, the ambient (less dense) fluid is contained in a finite volume. Since the dense fluid leaving the tube mixes with the ambient fluid, the density of the solution in the finite volume increases with time. Then at some later time (after the initiation of the mixing process), the mixing ceases because the density of the fluid throughout the system becomes uniform. Mixing was present in the ambient volume of the stairwell problem, but it did not enter the analysis because the ambient volume was infinite, and hence there was always a source of buoyancy.

The spatial-time density distribution in the ambient volume is very complicated. However, the system can be simplified by making an assumption equivalent to the "well-mixed" hypothesis in the stairwell - corridor system. For instance, the finite ambient volume of less-dense fluid can be assumed to be well-mixed, and this problem nearly reduces to the previous model. Clearly, this "well-mixed" hypothesis is reasonable for a system where the volume of the vertical duct is comparable to the volume of the ambient fluid. With this assumption, the system to be solved is as follows:

$$\frac{\partial\theta}{\partial\tau} = k\frac{\partial}{\partial x}\left(\frac{\partial\theta}{\partial x}\right)^{3/2} \qquad \tau \geq \tau_o \ ,$$

$$\theta = \theta(x) \qquad \text{at} \qquad \tau = \tau_o \ ,$$

$$\frac{\partial\theta}{\partial x} = 0 \qquad \text{at} \qquad x = 1 \ ,$$

$$k\left(\frac{\partial\theta}{\partial x}\right)^{3/2} = V_r\frac{\partial\theta}{\partial\tau} \qquad \text{at} \quad x = 0 \ , \tag{4.45}$$

and

$$V_r \equiv \frac{V_{\text{ambient fluid}}}{V_{\text{tube}}} \ ,$$

where a well-mixed bottom assumption replaces the boundary condition, $\theta = 0$ at $x = 0$, which was used in the basic vertical tube system. In this analysis, it was convenient to redefine the volume ratio, V_r, and the density ratio, θ. V_r is the ratio of finite volume of the ambient fluid to the volume of the vertical tube. Now the density ratio is defined as

$$\theta \equiv \frac{\rho-\rho_f}{\rho_i-\rho_f} \ ,$$

where ρ_f is the final (equilibrium) density of the system, and replaces ρ_a of the previous model. Therefore, θ cannot equal zero at $x = 0$ as in the brine solution model. It is always less than zero in this case because the initial density in its bottom value, $\rho_o \equiv \rho(x=0, \tau=\tau_o)$, is such that $\rho_o < \rho_f < \rho_i$.

The solution again has the form

$$\theta = F(x)H(\tau)$$

where

$$H = \frac{1}{\left[\frac{a}{2}(\tau-\tau_o)+1\right]^2}$$

and

$$\frac{dF}{dx} = \left(\frac{5}{6}\frac{\alpha}{k}\right)^{2/5}\left(1-F^2\right)^{2/5} \quad . \tag{4.46}$$

Simplification of (4.45) yields

$$\frac{\dot{F}^{3/2}}{F}\Big|_{x=0} = -\left(\frac{\alpha}{k}\right)V_r \quad . \tag{4.47}$$

Now, combining (4.46) and (4.47) gives

$$\left(\frac{5}{6}\frac{\alpha}{k}\right)^{2/5} = -\frac{5}{6}\frac{\left(1-F_o^2\right)^{3/5}}{F_o V_r} \tag{4.48}$$

where $F_o = F(x=0)$. The system has been reduced to two equations and two unknowns. That is,

$$\frac{dF}{dx} = \left(\frac{5}{6}\frac{\alpha}{k}\right)^{2/5}\left(1-F^2\right)^{2/5} \qquad F_o \le x \le 1 \quad ,$$

boundary conditions: $F = F_o$ at $x = 0$, $F = 1$ at $x = 1$, and

$$\left(\frac{5}{6}\frac{\alpha}{k}\right)^{2/5} = -\frac{5}{6}\frac{\left(1-F_o^2\right)^{3/5}}{F_o V_r} \quad ,$$

where F_o is a negative number. α/k and F_o, which are functions of V_r, must be found before the differential equation can be integrated. They may be found by integrating the differential equation from F_o to 1 and substituting the value of $\left(\frac{5}{6}\frac{\alpha}{k}\right)^{2/5}$ from (4.48) into the relation. Then solving for V_r we get

$$V_r = \frac{-\frac{5}{6}\frac{\left(1-F_o^2\right)^{3/5}}{F_o}}{\int_{F_o}^{1}\frac{df}{\left(1-f^2\right)^{2/5}}} \quad . \tag{4.49}$$

The integral in (4.49) may be evaluated by noting that

$$= 1.3872$$

$$\int_{F_o}^{1} \frac{df}{(1-f^2)^{2/5}} = \int_{F_o}^{0} \frac{df}{(1-f^2)^{2/5}} + \int_{0}^{1} \frac{df}{(1-f^2)^{2/5}} \qquad (4.50)$$

The resulting integral may be solved graphically with the use of the separation of variables solution in Fig. 4.9. For example, the equation

$$\int_{0}^{F} \frac{df}{(1-f^2)^{2/5}} = 1.3872\,x \qquad (4.51)$$

is plotted as F against x in Fig. 4.9. Because of the symmetry of the integrands in (4.50) and (4.51), the integrals are equivalent. Therefore, the volume ratio may be written as

$$V_r = \frac{-\frac{5}{6}\frac{(1-F_o^2)^{3/5}}{F_o}}{1.3872\,(1+x_o)} \qquad (4.52)$$

where x_o is the value of x corresponding to a particular F, (F_o), in Fig. 4.9 (separation of variables solution). Now, α/k can be found from (4.48) since the relationship between V_r and F_o is given in (4.52). The density profile, F(x), was obtained by integrating the differential equation for $\dot{F}$ numerically. Figures 4.12 and 4.13 contain the results of this analysis.

The plot of α/k against V_r is given in Fig. 4.12. It shows that $\alpha/k \to 2.72$ as the volume of the ambient fluid becomes infinite, which is the same as that in the brine solution model. Also, $\alpha/k \to \infty$ as $V_r \to 0$, which implies that the mixing speeds up when the ambient volume of fluid is reduced to less than the tube's volume. In this case, the well-mixed assumption seems reasonable because the mixing in the

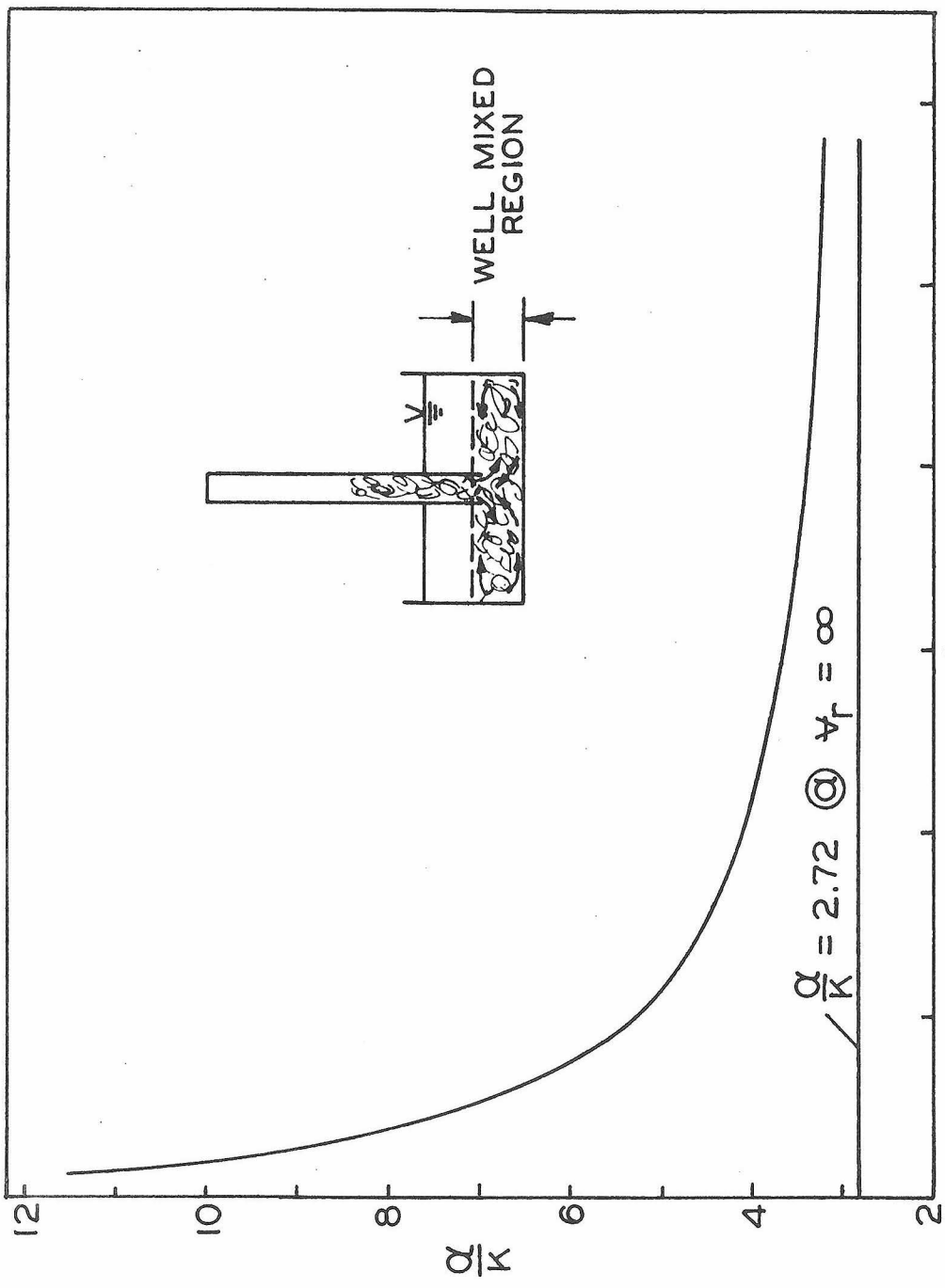

Fig. 4.12 Variation of α/k with Volume Ratio for the "Well-Mixed Bottom" Boundary Condition.

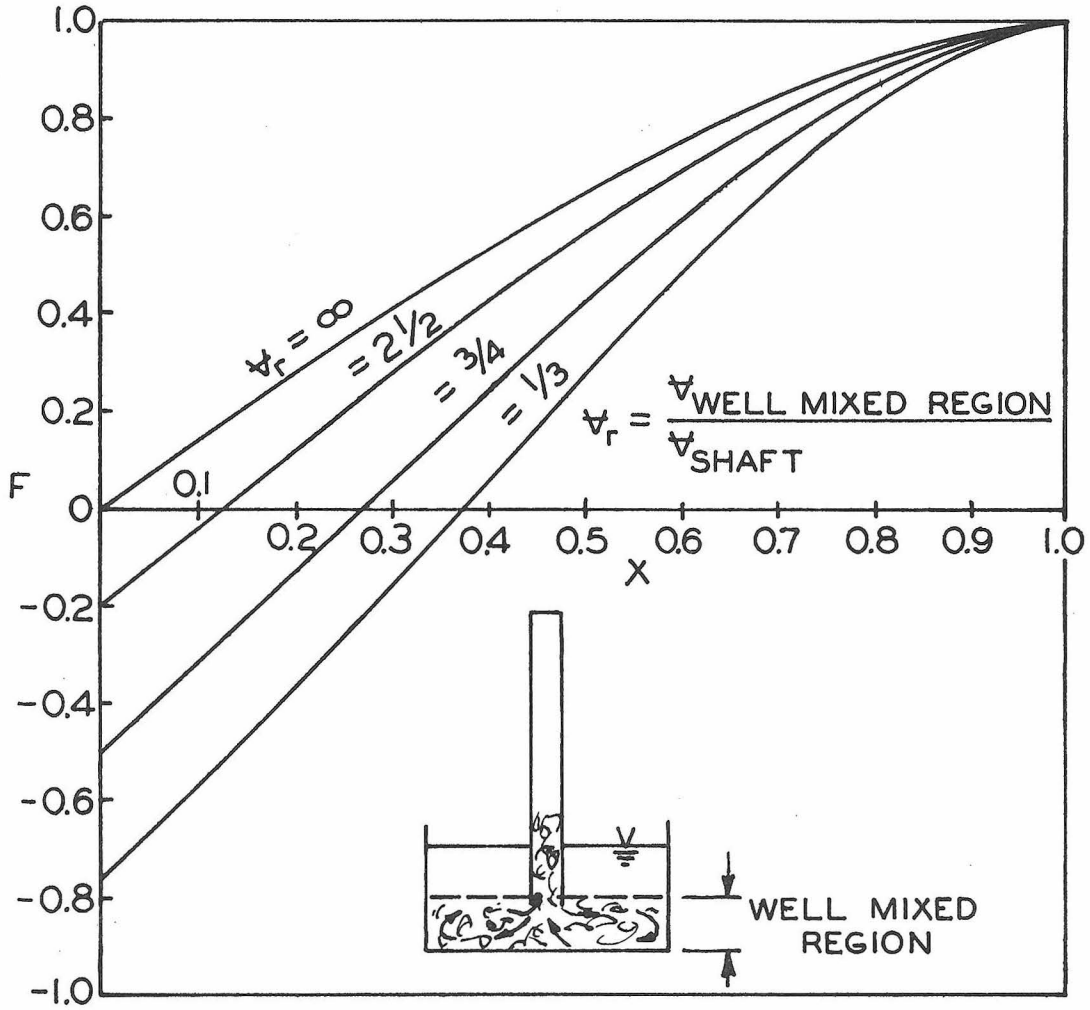

Fig. 4.13 Density Profiles for the "Well-Mixed Bottom" Boundary Condition.

ambient fluid is likely to be comparable to that in the tube. The corresponding density profiles, F(x), are plotted in Fig. 4.13. These profiles are different from the previous solutions because $F(0) < 0$. This implies that the density of the ambient fluid increases with time, and hence the buoyancy in the model decreases. Since $F \sim \frac{\rho - \rho_f}{\rho_i - \rho_f}$, the normalized density is zero at some cross section in the tube, and it remains that way because the function of time in the solution decreases the density at every point in the tube simultaneously after the initial profile has been established.

4.3 Heat Transfer Model

This section considers all modes of energy transfer that take place in the stairwell model as presented in Chapter 3. Only the effects of buoyancy were considered in the previous analysis and the density differences were due to specie changes rather than due to temperature changes as in the heat transfer model. Although the mixing phenomena are due to buoyancy forces, the diffusion equation must be derived in terms of temperature, rather than density, in order to analyze the effects of heat transfer in the system. An analytical model is presented in the following subsections that include the heat transfer through the walls of the duct as well as the mixing due to the strong buoyancy forces.

Two particular examples are examined here in detail for steady-state conditions. The first involves a tube with a constant temperature top and insulated walls; and the second, constant temperature top and walls. Solutions of both will be found by examining the latter problem and obtaining the solution to the former problem as a

special case. The equations developed here could be solved with other boundary conditions.

4.3.1 Energy Equation. Derivation of the energy equation in the heat transfer model is analogous to that of the turbulent diffusion equation in the buoyancy force model. Figure 4.14 schematizes the energy transfer mechanisms that take place as a result of hot gas propagating up a vertical duct. Balancing the turbulent transport of energy in the vertical direction with the convective heat flux through the walls of the duct yields:

$$\frac{\partial \bar{Q}}{\partial t} + \frac{\partial}{\partial z}\left(\overline{w'Q'}\right) = -\dot{q}\left(\frac{4}{d}\right) \qquad (4.53)$$

where $\overline{w'Q'}$ = turbulent energy transfer, and $\dot{q}$ = convective heat flux per unit area to the duct walls, and $\bar{Q} \equiv \rho c_p T$.

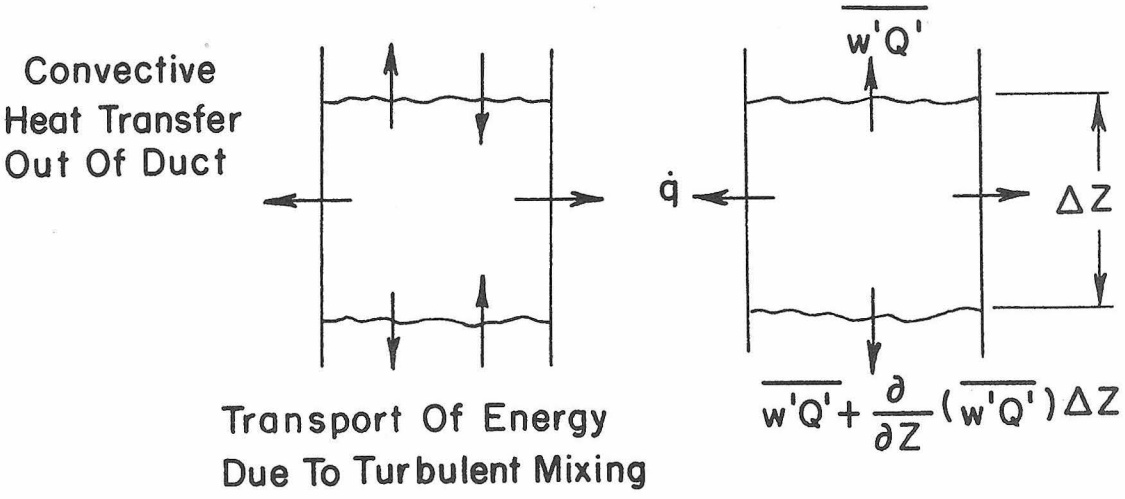

Fig. 4.14 Definition Sketch of Energy Transfer Mechanisms in the Heat Transfer Model.

All quantities such as ρ and T are understood to be averaged over time and cross-sectional area as in the previous analysis. $\overline{Q}$ is the average quantity of heat contained in the infinitesimal volume, and Q' is the deviation in time from the mean value. Note that the molecular transport terms were neglected in (4.53) as in the previous analysis. Using Reynolds' mixing analogy, we assume that the turbulent transport of heat can be written as

$$\overline{w'Q'} = -D \frac{\partial \overline{Q}}{\partial z} , \tag{4.54}$$

where D is the turbulent mixing coefficient. Also, the convective heat flux to the wall is assumed to have the form

$$\dot{q} = H(T-T_s) , \tag{4.55}$$

where H is the film coefficient and T_s is the surface temperature of the tube. Substituting (4.54) and (4.55) into (4.53) and simplifying yields

$$\frac{\partial}{\partial t}(\rho T) - \frac{\partial}{\partial z}\left[D \frac{\partial}{\partial z}(\rho T)\right] = -\frac{4H}{d\, c_p}(T-T_s) , \tag{4.56}$$

where c_p is assumed to be constant. The quantity (ρT) can be found from the equation of state and assuming that the pressure is distributed hydrostatically in the tube. That is,

equation of state: $$\rho T = P/R , \tag{4.57}$$

hydrostatic pressure distribution: $$\frac{\partial P}{\partial z} = -\rho g . \tag{4.58}$$

Combining (4.57) and (4.58) yields:

$$\frac{\partial}{\partial z}(\rho T) = -\frac{\rho g}{R} . \tag{4.59}$$

After substituting this result into (4.56), the energy equation becomes

$$\frac{\partial}{\partial t}(\rho T) + \frac{g}{R}\frac{\partial}{\partial z}(\rho D) = -\frac{4H}{d\,c_p}(T-T_s) \ .$$

4.3.2 Solution for Steady-State. In Section 3.2 we pointed out that the heat capacity of the walls of the stairwell is much greater than the heat capacity of the gas contained in it. Therefore, we assumed the temperature of the walls of the stairwell to be constant and uniform during the initial stages of the fire. This assumption allows a steady-state solution to exist in the duct. For instance, hot gas entering the duct is cooled (due to heat transferred to the wall) as it propagates upward. Heat transferred from the hot gas causes the system to always be unstable; i.e., dense (cool) gas is always above the less dense (hot) gas.

Therefore, using the steady-state assumption, the energy equation is as follows:

$$\frac{d}{dz}(\rho D) = \frac{4HR}{d\,c_p g}(T_s-T) \ . \qquad (4.60)$$

The equation of state is the second equation in this system, since the energy equation contains two unknowns, ρ and T. Differentiating (4.59) and simplifying it yields

$$\frac{dT}{dz} = -\frac{g}{R} - \frac{T}{\rho}\frac{d\rho}{dz} \qquad (4.61)$$

where the term $-g/R$ is the hydrostatic contribution.

The system to be solved is as follows:

energy equation: $$\frac{d(\rho D)}{dz} = \frac{4HR}{d\,c_p g}(T_s-T) \ ,$$

equation of state: $$\frac{dT}{dz} = -\frac{g}{R} - \frac{T}{\rho}\left(\frac{d\rho}{dz}\right) \ ,$$

boundary conditions: $T = T_a$ and $\rho = \rho_a$ at $z = 0$,

and $T = T_s$ at $z = L$.

The nature of the solution to the system of equations depends on the choice of mixing coefficient D and film coefficient H. One logical choice for the form of the diffusion coefficient is the same as that used in the brine solution model. Therefore,

$$D \equiv D_o \sqrt{\frac{L}{\rho} \frac{d\rho}{dz}} \quad , \tag{4.62}$$

where D_o is a scaling parameter defined as

$$D_o = \frac{1}{4} \sqrt{g/L} \; (d^7 L)^{1/4} \quad . \tag{4.63}$$

There is no information available from previous work concerning the nature of the film coefficient for the type of flow under consideration. Qualitatively, one expects the film coefficient H to be a function of the turbulence in the flow. Therefore, H is assumed to be of the form

$$\frac{H}{(\rho_a c_p / d)} = hD \quad , \tag{4.64}$$

where h is a heat transfer constant and D is the turbulent diffusion coefficient discussed above. This form of H seems reasonable since D is a measure of the turbulence in the system.

Note that by setting h to zero, the special case of insulated side walls can be obtained from this analysis.

The equations can be normalized by making the following substitutions:

$$\theta \equiv T/T_a \; , \quad \phi \equiv \rho/\rho_a \; , \quad x \equiv z/L \; , \quad \text{and} \quad \theta_s \equiv T_s/T_a \quad .$$

After simplification the system can be written as follows:

energy equation: $$\ddot{\phi} + \frac{\dot{\phi}^2}{\phi} + 2h\beta \frac{\dot{\phi}}{\phi} (\theta - \theta_s) = 0$$

equation of state: $$\dot{\theta} = -\gamma - \theta \frac{\dot{\phi}}{\phi}$$

$$\theta = 1 , \ \phi = 1 \text{ at } x = 0 \ ; \ \theta = \theta_s \text{ at } x = 1$$

where

$$\gamma \equiv \frac{gL}{RT_a} \quad \text{and} \quad \beta \equiv \frac{4}{\gamma} \left(\frac{L}{d} \right)^2 .$$

In the energy equation, $(\ddot{\phi} + \dot{\phi}^2/\phi)$ represents the diffusion and $2\beta h \dot{\phi}/\phi \, (\theta - \theta_s)$ is the heat flux out of the tube. Two extreme cases exist depending on the magnitude of $h\beta$. As $h\beta \to 0$ the diffusive terms are dominant and the system should be very turbulent as in the buoyancy model. However, as $h\beta \to 0$ the heat flux to the tube walls is dominant and there may be very little mixing. The value of β is about 10^5 for cases examined experimentally, and nothing is known about h. Therefore, the system was solved for $0 \leq h \leq 10^{-3}$. Standard shooting methods (Section 4.2.3) were used to solve the two-point boundary value problem. $\dot{\phi}$ at $x = 0$ was estimated initially in order to solve the corresponding "initial value" problem. The fourth order Adams-Moulton predictor-corrector method was the numerical scheme used.

The solution is given in Fig. 4.15. The plot of temperature against distance along the central axis of the tube is the solution to the heat transfer model for $T_s = 203^{\circ}K$ and $T_a = 296^{\circ}K$. The two extremes in this plot are the temperature profiles for $h = 0$ and $h = 10^{-3}$. The profile for $h = 0$ corresponds to an insulated tube with the heat flux through the top surface as shown in Fig. 4.16. This solution is for a steady state since the heat flux, Q, that enters the mouth of the tube leaves through the top surface. A schematic of the constant tem-

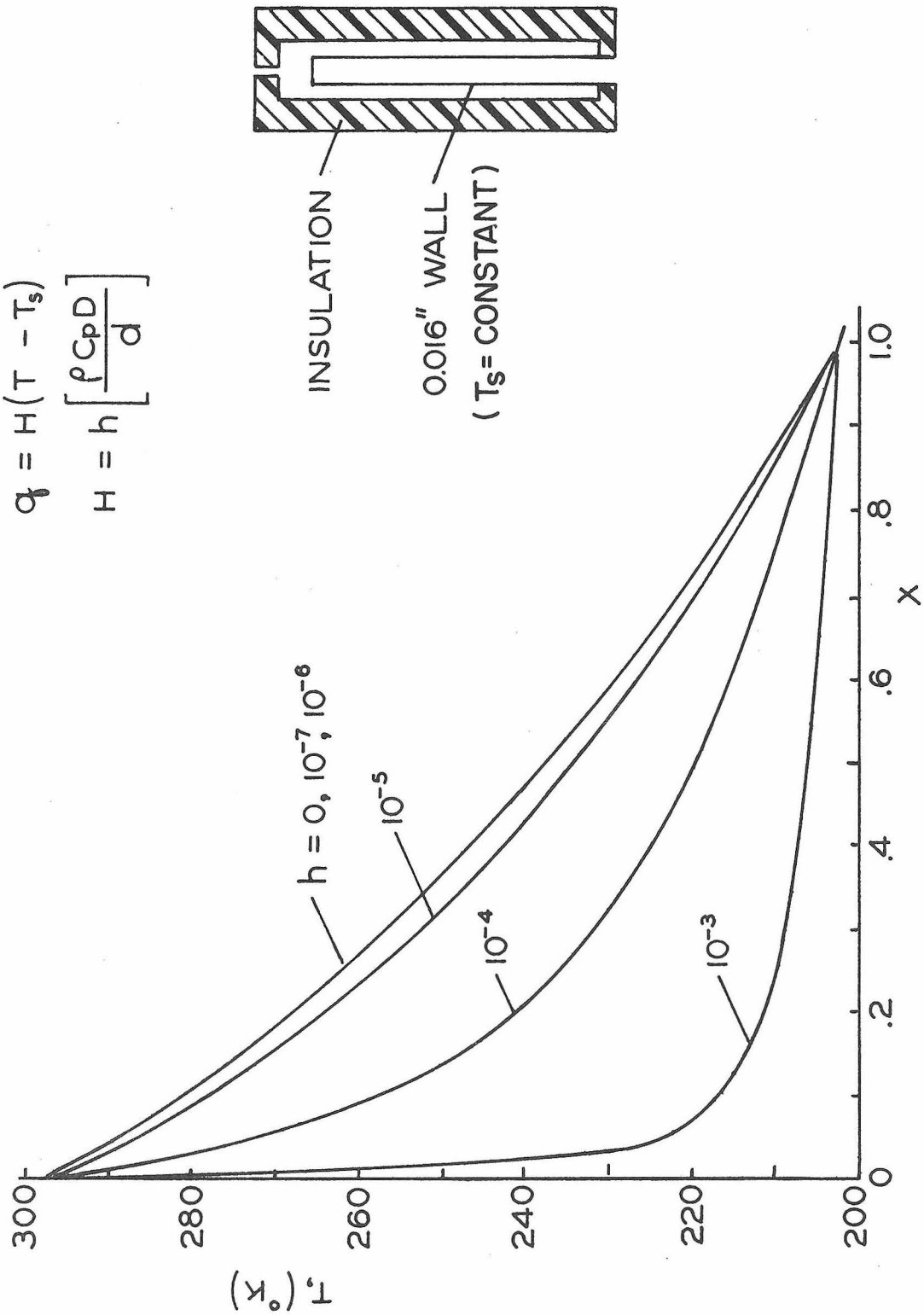

Fig. 4.15 Theoretical Temperature Profiles of the Heat Transfer Model for $T_s = 203^{\circ}K$ and $T_a = 296^{\circ}K$.

perature tube for which $h > 0$ is shown in Fig. 4.17. The mixing in this case is also steady, but heat is transferred through the walls of the duct as well as through the upper surface.

The temperature profile for $h = 10^{-3}$ (see Fig. 4.15) is particularly interesting. Heat transferred to the walls of the tube drains a large amount of energy from the system. This leads to a strong temperature gradient near the mouth of the tube which results from the strong mixing in that region produced by those strong gradients. Near the top of the tube the temperature is nearly uniform, and mixing will be weak. Thus, we end up with a tube with almost constant temperature throughout and with steep gradients near the exit.

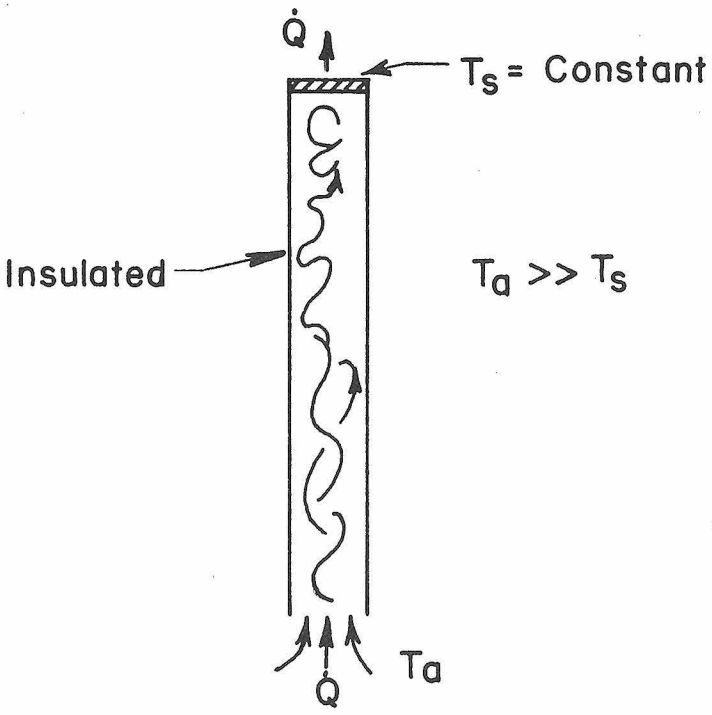

Fig. 4.16 Definition Sketch of Mixing Patterns in the Insulated Tube of the Heat Transfer Model.

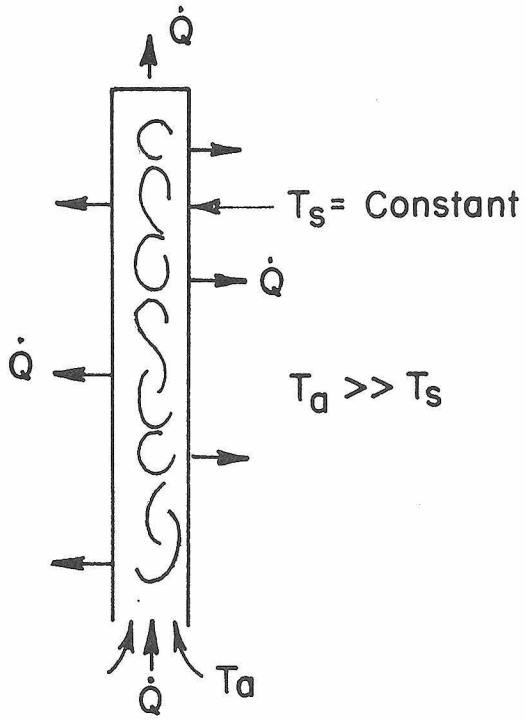

Fig. 4.17 Definition Sketch of Mixing Patterns in the Constant Temperature Tube of the Heat Transfer Model.

5. EXPERIMENTAL EQUIPMENT AND PROCEDURES

Laboratory experiments were performed to simulate the energy transfer mechanisms that occur in the stairwell of a burning high rise building. Three sets of experiments were considered. In each case, a vertical tube filled with a dense fluid discharged into an environment of a lighter miscible fluid. Brine solutions and dense gases mixed with tap water and air, respectively, in the buoyancy force model. The heat transfer model made use of low temperature air mixing with room temperature air. The purpose of the experimental model was to obtain a fundamental time scale that characterizes the mixing in the prototype and to check the validity of the analytical models presented in Chapter 4.

This chapter gives a complete description of the experimental apparatus and procedures for each set of experiments. Also, a summary of all the experimental runs is included in this chapter.

5.1 Brine Solution Experiments

A brief description of the brine solution model was given in Chapter 3. Figure 5.1 is a photograph of the experimental setup. It consists of a cylindrical tube filled with a salt solution in a basin of tap water. The concentration at selected points in the tube was recorded by means of a conductivity probe and Sanborn recorder system. The apparatus and procedures are described in detail in the following sections.

5.1.1 Apparatus.

(1) Experimental duct. Cylindrical tubes made of lucite were used for the experimental duct. The nominal wall thickness of

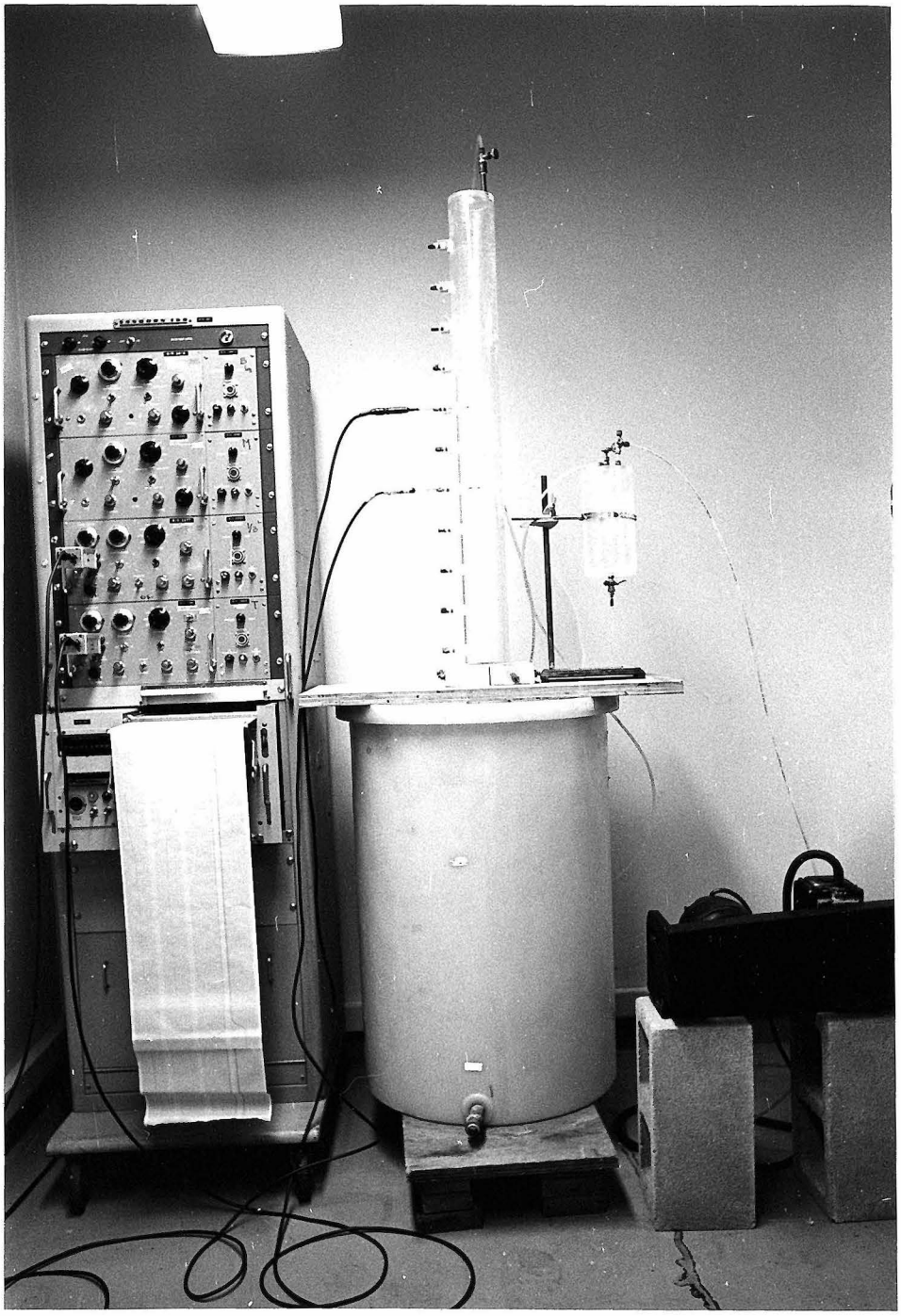

Fig. 5.1 The Experimental Setup for the Brine Solution Model.

each tube was 1/4". The lengths varied from 2' to 9', and the diameters from 1 1/2" to 7 1/8". Therefore, it was possible to consider a wide range of aspect ratios, 7.5 - 30. A photograph of a typical tube is shown in Fig. 5.2. Fittings to hold the conductivity probes are at selected locations along the tube.

The bottom plug that sealed the inlet of the tube is shown in Fig. 5.3. An "O" ring on the plug was used to ensure a vacuum tight fit.

(2) Experimental tank. The purpose of the experimental tank, in most instances, was to simulate an infinite environment of constant density fluid. A fluid environment whose density would not change during the course of the experiment was desired. Therefore, only two tanks were used. They were a 11' × 13' × 3' basin and a 70-gallon plastic tank with a 3' diameter. The plastic tank was used only for the smallest of the tubes. A volume ratio, V_{tube}/V_{tank}, less than 10^{-2} was adequate to achieve a constant density reservoir.

(3) Conductivity probe. The concentration or density at a point in the tube was measured by means of a conductivity probe. The probe design and a photograph are shown in Fig. 5.4. It was designed and constructed by Elton Daly of the Keck Hydraulics and Water Resources Laboratory at the California Institute of Technology. A probe of this type is ideal for the measurement of conductivity at a point. The electrodes are small and the spacing between them is not critical. They were kept in distilled water between runs and were cleansed and platinized whenever the readings became erratic. The platinization and cleansing processes were performed according to a standard

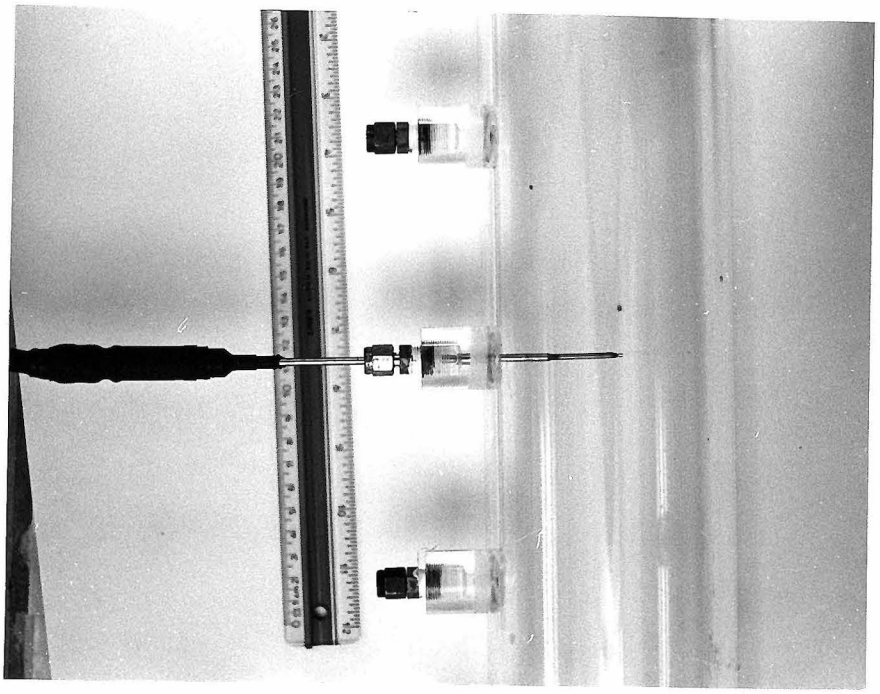

Fig. 5.2 A Typical Duct Used in the Brine Solution Model.

Fig. 5.3 A Typical Bottom Plug for the Vertical Duct of the Brine Solution Model.

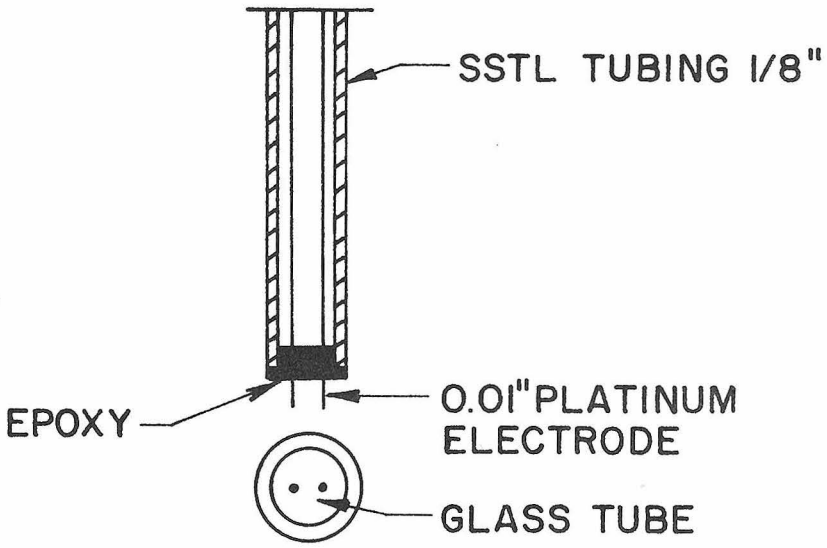

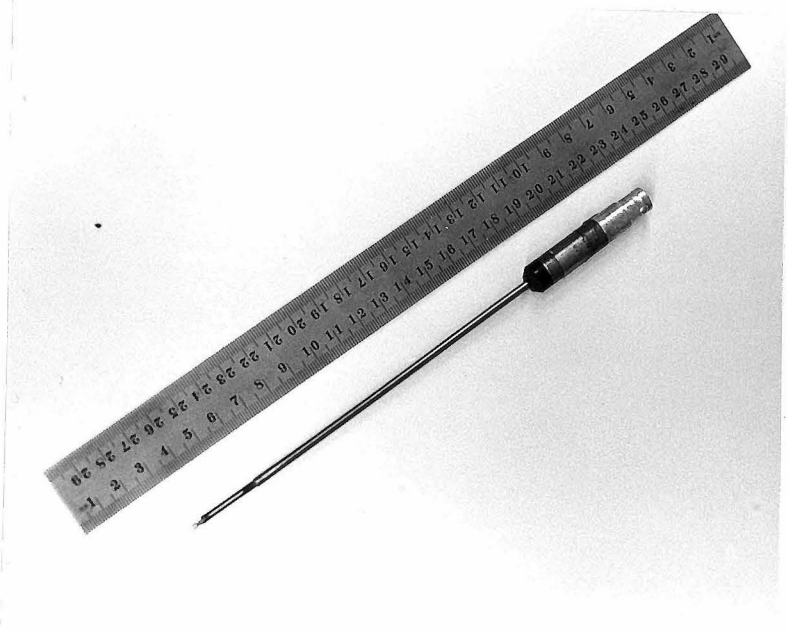

Fig. 5.4 The Conductivity Probe.

chemical method[8].

(4) Sanborn recording system. The Sanborn recording system Series 150 was used for all of the conductivity measurements. It makes use of the Wheatstone bridge circuit shown in Fig. 5.5 . All of the resistors are precision wire wound. They are needed to eliminate the drift that is common to all tube-type recording systems. The conductivity probe is part of an arm of the Wheatstone bridge circuit. The bridge was balanced internally by the use of the Sanborn preamplifiers. The out-of-balance voltage of the probe was recorded whenever the conductivity of the solutions changed.

The system was calibrated by means of standard solutions of different conductivities. The specific gravity of each standard solution was obtained by a hydrometer. A typical calibration curve is shown in Fig. 5.6. The stylus deflection of the recorder is plotted against the specific gravity of the solution.

5.1.2 Procedure. A photograph of the experimental setup is shown in Fig. 5.1. Prior to each run the basin was mixed thoroughly with compressed air to insure that its density was uniform. The cylindrical tube was attached to a vertical stand over the tap water reservoir. It was filled with a salt solution by means of a vacuum pump, which was used to suck salt solution in through a pipe in the closure plug. The mouth of the tube was approximately 2" below the surface of the tap water reservoir during all of the runs. The tube was allowed to stand until all of the excess oxygen was out of the brine solution and for the ambient fluid to become motionless. Then the plug was gently pulled out of the mouth of the tube so that the ambient

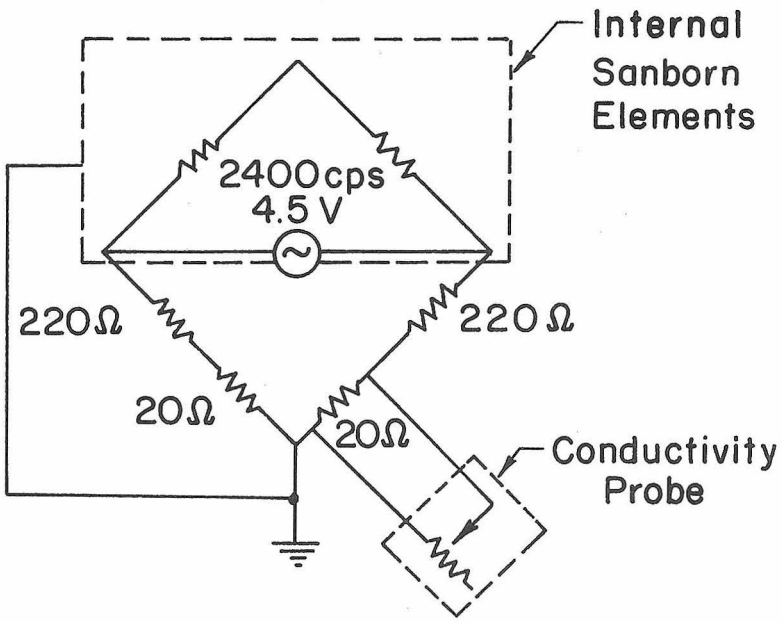

Fig. 5.5 The Bridge Circuit Used in Conjunction with the Sanborn Recorder for the Measurement of Conductivity.

fluid would not be disturbed excessively. The initial front that propagates up the duct was timed at selected positions. Also, the concentration of the solution was recorded at different points along the tube. The concentration was recorded until it was reduced to a predetermined value.

5.1.3 Density-Concentration Relationship. In Chapter 4 (Eq. (4.4)), we pointed out that the density of the salt-water mixture, ρ, can be related to the concentration of salt, c, in the following manner:

$$\rho - \rho_o = \beta(c - c_o) \qquad (4.4)$$

where ρ_o is the density of water at some reference temperature and c_o is zero in this case. This relation is only a first order approxima-

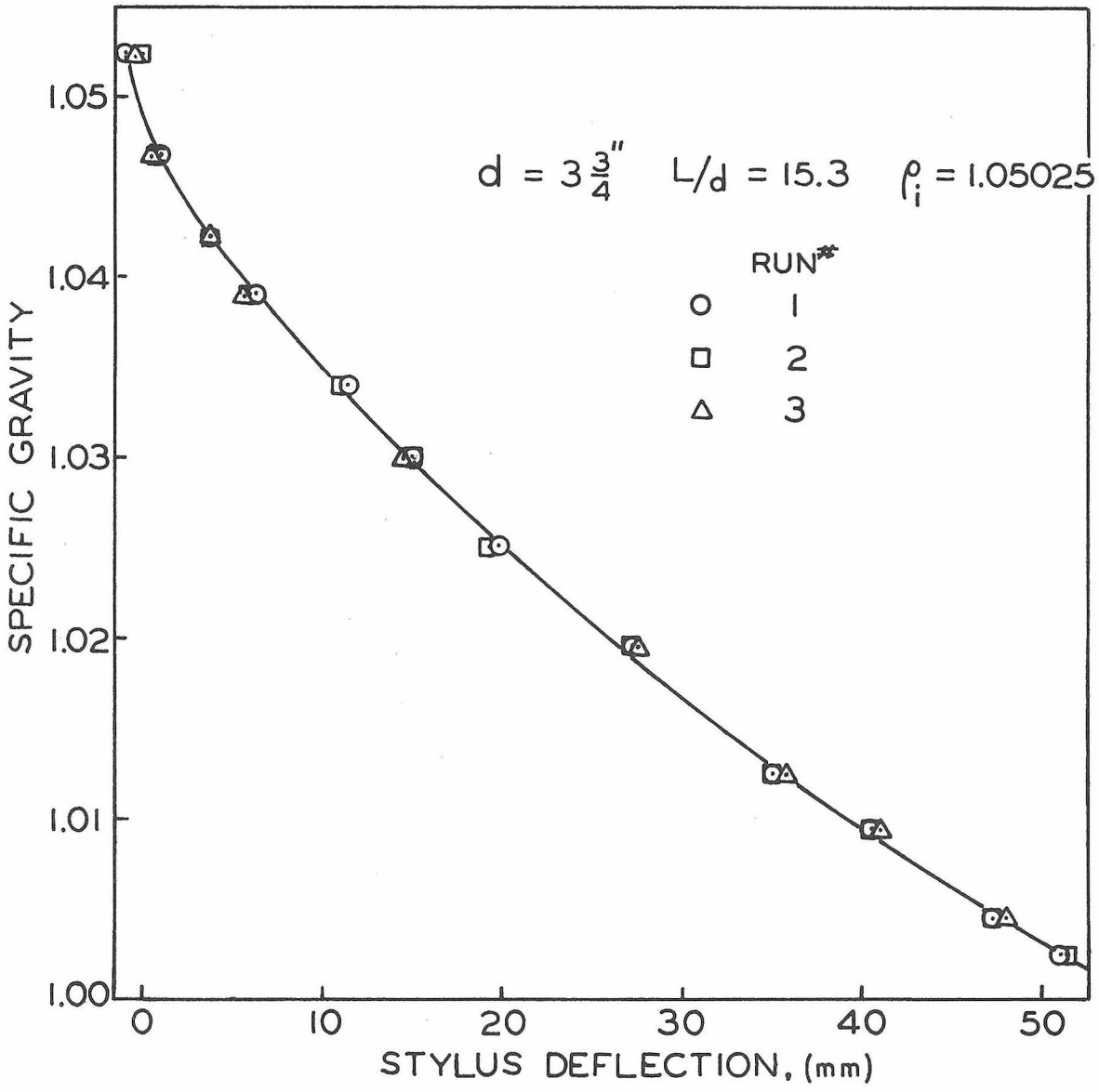

Fig. 5.6 A Typical Calibration Curve for the Brine Solution Experiments.

tion. Figure 5. 7 contains a plot of ρ against c for a salt-water mixture at room temperature. The curve drawn through the points is linear. Careful inspection of the graph reveals that the curve is not exactly linear, but for all practical purposes we will assume it to be so. The linearity of the relation is important because the gases used in the buoyancy model obey the equation of state. That is,

$$\rho - \rho_a = \frac{P}{R_o T}(M - M_a) \qquad (4.5)$$

which states that the density of the gas mixture is a linear function of the average molecular weight of the mixture. In this case, β' is defined as $P/R_o T$ and has a value of 2.48×10^{-3} (at $T = 25^{o}C$), and $\beta = .691 \times 10^{-3}$ from Fig. 5.7.

Because of these linear relationships, mixing of two volumes containing fluids with different densities will lead to a mixture with an intermediate density which will occupy a volume exactly equal to the sum of the original volumes. In this sense, constant volume mixing will occur, and hence no volume flux from the system will occur due to the mixing process.

5.2 Gas-Gas Experiments

The experimental setup for the gas-gas experiments was similar to that in the previous model. Instead of brine solutions mixing with tap water, mixtures of dense gases and air diffused into the ambient air in this case. A schematic of the system is shown in Fig. 5.8. It consists of a vertical tube, Beckman OM-11 oxygen analyzer, Sanborn recorder system, and a mixing chamber.

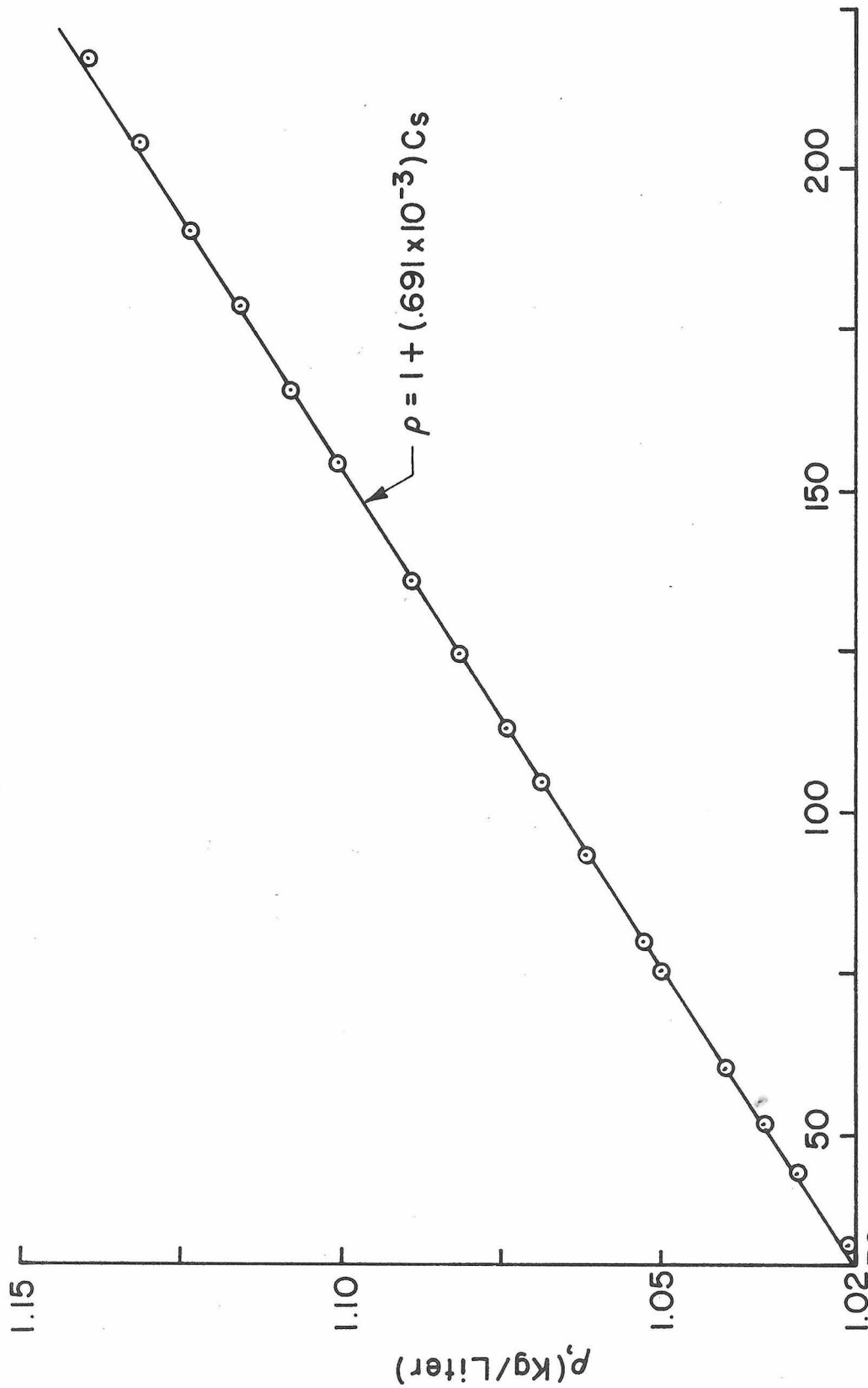

Fig. 5.7 Density-Concentration Relationship for Salt Water Mixtures.

A 1/2' × 6' glass tube was suspended vertically by means of a tripod and the open end (bottom) of the tube was approximately 2' above the surface of the floor. The OM-11 detector was connected to the top of the tube by a piece of tygon tubing, 1/8" I. D. and 1' long. The response time of the oxygen analyzer ranged from .1 to 1 second. Sampling gas was drawn from the test tube at a rate of 500 cc/minute, which is very small. During an experimental run of five minutes, less than 1/12 of the total volume of gas in the test tube was drawn from it. The sample gas passed through a membrane of the oxygen detector that is only sensitive to the partial pressure of oxygen in the sample. The voltage output of the detector was recorded by the Sanborn recorder.

The test tube was filled with a dense gas that had been premixed with air in a chamber to obtain the desired molecular weight. Argon (M = 40) and sulfur hexafluoride (M = 146) were used to produce the dense gas. The gas was bled into the test tube until the oxygen analyzer indicated that no air was present. After the turbulent motion due to filling of the test tube had died out, the bottom plate was removed to allow mixing with the ambient air to take place. The results were recorded on the Sanborn recorder.

Prior to each experiment the system was calibrated. Predetermined amounts of air and a dense gas (Ar or SF_6) were mixed in a large mixing chamber. The kinetic energy of the gases entering the chamber aided the mixing. Pressure gauges in the system were used to determine the number of moles of each gas present. The oxygen analyzer was used to sample the gas mixture in the chamber after it

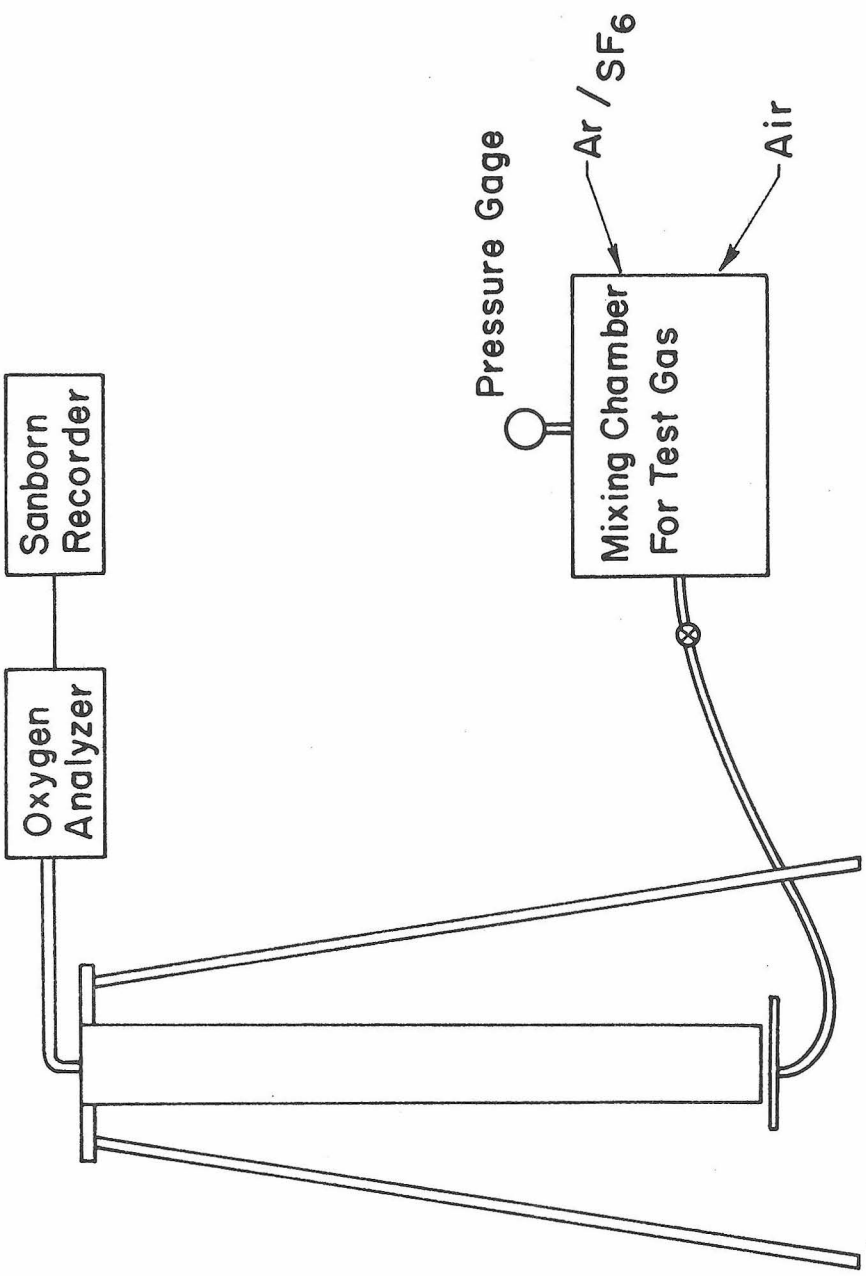

Fig. 5.8 Schematic of Experimental Setup for the Gas-Gas Experiments.

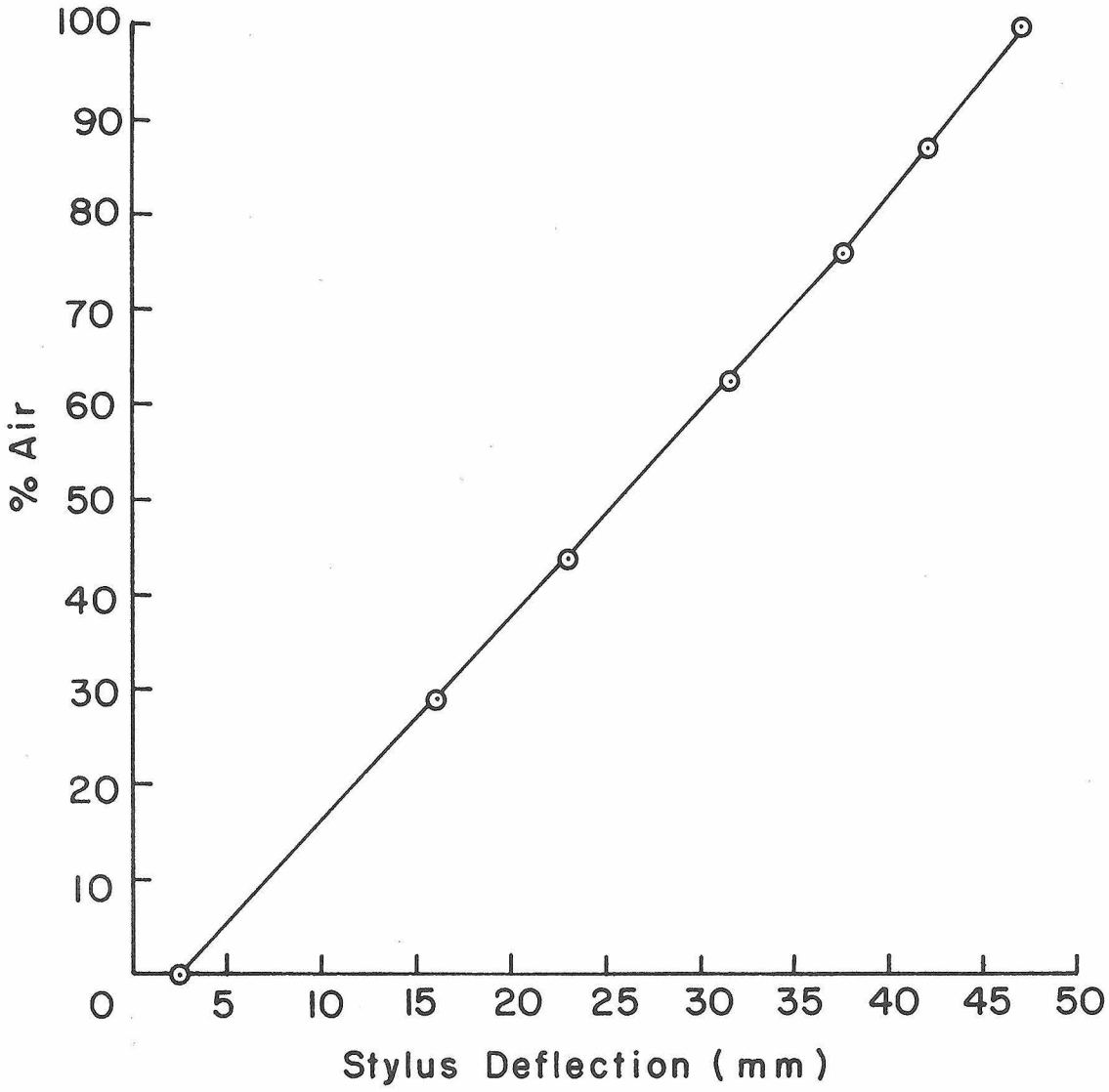

Fig. 5.9 A Typical Calibration Curve for the Gas-Gas Experiments.

was allowed to stand for 15 minutes. Figure 5.9 is a typical calibration curve for the system.

5.3 Heat Transfer Experiments

Two heat transfer experiments were conducted: (1) an insulated tube with the heat flux through the top surface, and (2) a constant temperature tube with small density differences, $T_s > 200^{o}K$. The insulated tube corresponds to the solution of the energy equation (heat transfer model) for which $h = 0$, and the constant temperature tube corresponds to $h > 0$ in the energy equation. Also, we attempted to measure the heat transfer out of the constant temperature tube by using the thin skin approximations.

5.3.1 Insulated Tube with Heat Transfer through the Upper Surface. A photograph of the experimental setup is shown in Fig. 5.10. It consists of a vertical insulated tube, Sanborn recorder system, thermocouples, and a thermocouple switch. The test tube was constructed from four 3' sections of polyurethane pipe covering glued together to form a 6' tube (5" I.D., 2" wall thickness). The top of the tube was closed with the bottom surface of a steel cup, and the bottom portion of the tube was open. Iron-constantan thermocouples, d = .005", were located along the tube's central axis and spaced 5" apart. The voltages from the thermocouples were amplified and recorded on the Sanborn recorders.

The experiment started when the steel cup was filled with liquid nitrogen. It was added frequently in order to keep the top surface at a constant temperature. Measurements were taken over a period of 5 hours to insure that a steady state existed. The voltages

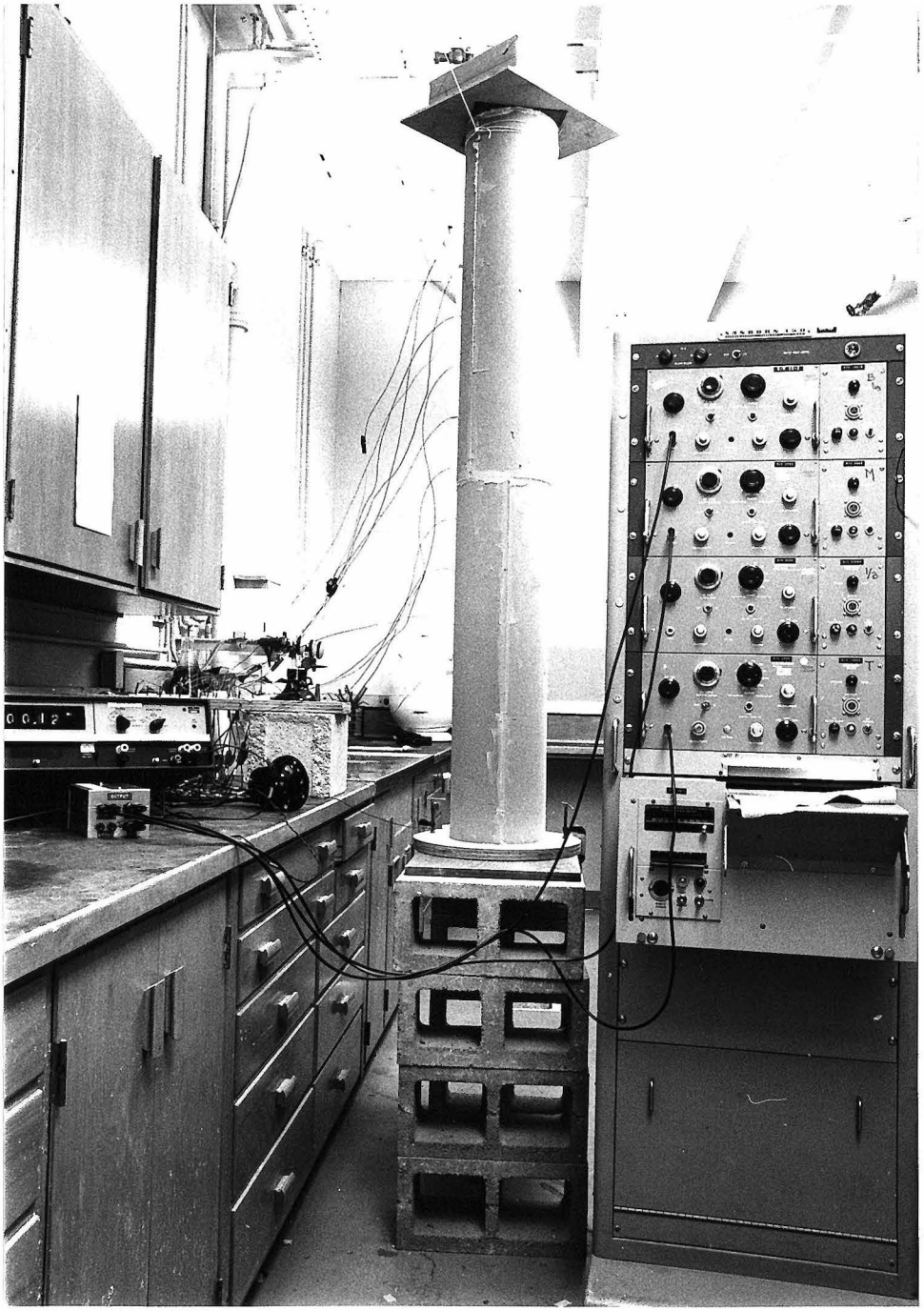

Fig. 5.10 The Experimental Setup for the Insulated Tube.

were recorded on a single channel of the recorder with the use of a thermocouple switch.

5.3.2 Constant Temperature Tube. The experimental setup was identical to that in the previous case. Design details of the tube system are shown in Fig. 5.11. It consists of two concentric steel tubes with the top of the inner cylinder sealed. The 3" inner tube (test tube) has a wall thickness of .016" and is made of stainless steel. The 5" outer cylinder has a 1/8" wall thickness and is covered with insulation on its outer surface. This arrangement made it possible to fill the cavity between the tubes with a liquid in order to keep the test tube at a constant temperature.

The procedure consisted of two parts. Initially, the cavity was filled with a solution of dry ice and acetone. The temperature of the test tube and the air inside it was monitored with the thermocouples during the mixing process. After a steady state existed, the axial temperature profile of the air in the tube was recorded, and then the cavity was drained. The latter part of the procedure consisted of recording data during the transient period following the draining process. The temperature - time history of the tube's surface and the air in it at selected points was recorded on a single-channel recorder with the use of the thermocouple switch. The measurements taken during the transient period were used to calculate the heat transfer out of the tube.

5.4 Summary of Experimental Runs

The experimental runs can be categorized in the following manner: (1) brine solution - tap water, (2) gas - gas, and (3) heat

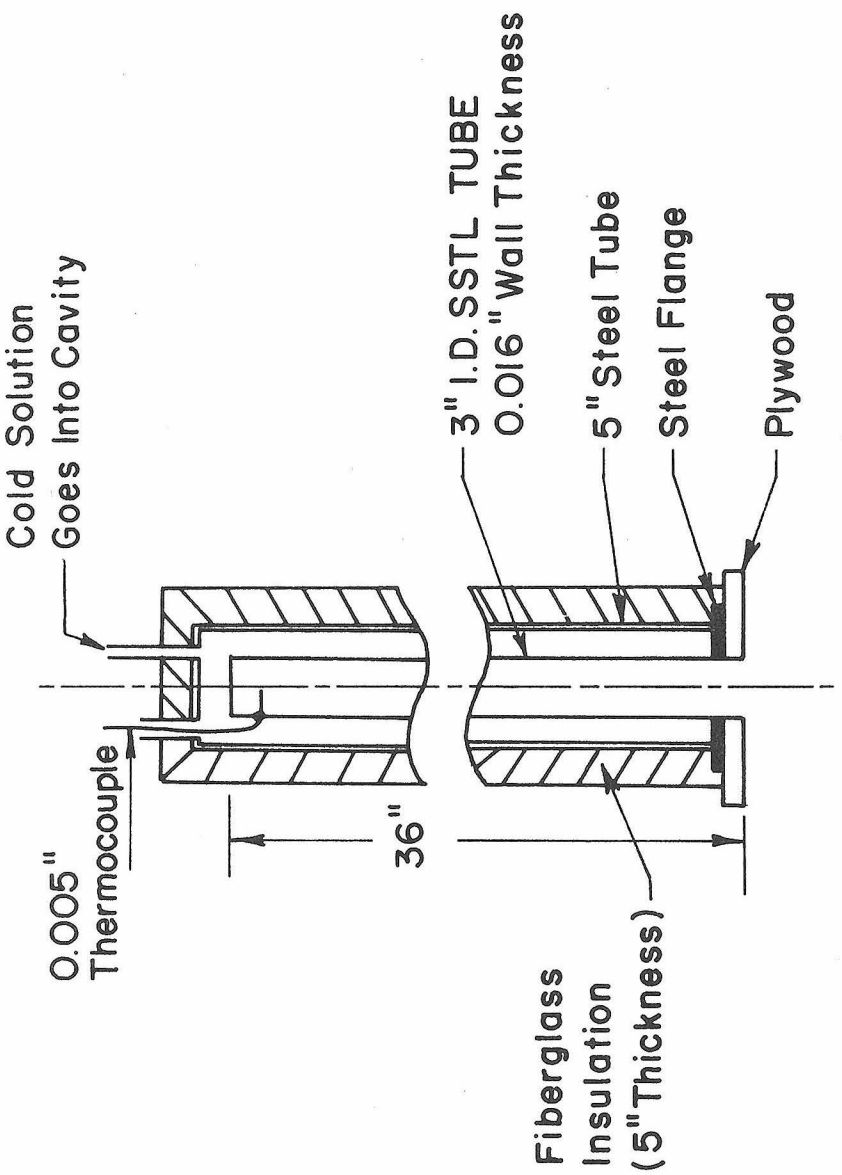

Fig. 5.11 The Constant Temperature Tube.

transfer. The brine solution model was investigated in more detail than the other experiments. All of the brine solution - tap water experiments that dealt with the mixing phenomena in the stairwell model are listed in Tables 5-1 and 5-2. Figure 5.12 is a typical graph of an experimental run for the data listed in Table 5-1.

Table 5-1. Summary of Brine Solution Experiments Performed in Order to Obtain τ in the Stairwell Model.

$\frac{\Delta\rho_i}{\rho_a}$ / $\frac{L}{d}$	7.8	11.5	15.3	20	25	29
1%	7 1/8"		1 1/2"			
2%			3 3/4", 1 1/2"			
3.5%		5 1/2", 7 1/8"				
5%	7 1/8", 3 3/4"	2", 5 1/2", 7 1/8"	2", 3 1/2", 7 1/8"; 3 3/4", 1 1/2"	3 1/2", 2"	2"	2"
7.6%			1 1/2", 3 3/4"			
8.5%		5 1/2", 7 1/8"				
10%	7 1/8", 3 3/4"		1 1/2", 3 3/4", 7 1/8"			
12.5%		5 1/2", 7 1/8"				
15%	3 3/4", 7 1/8"	5 1/2", 7 1/8"	1 1/2", 3 3/4", 7 1/8"	3 1/2"		

Note: Concentration measurements were taken at x = 1. Entries in the table are the diameters of the various tubes.

TABLE 5-2. Summary of Brine Solution Experiments Performed in Order to Obtain the Density Stratification in the Stairwell Model.

(z/L lists axial position of probes.)

d = 1 1/2", L/d = 15.3 ρ_i = 1.050	d = 3 1/2", L/d = 15.3 ρ_i = 1.050
z/L = 1.0	z/L = 1.0
.8	.87
.6	.74
.38	.61
	.47
	.36

d = 5 1/2", L/d = 11.5 ρ_i = 1.050	d = 7 1/8", L/d = 15.6 ρ_i = 1.050, 1.100
z/L = 1.0	z/L = 1.0
.82	.58
.64	
.46	
.25	

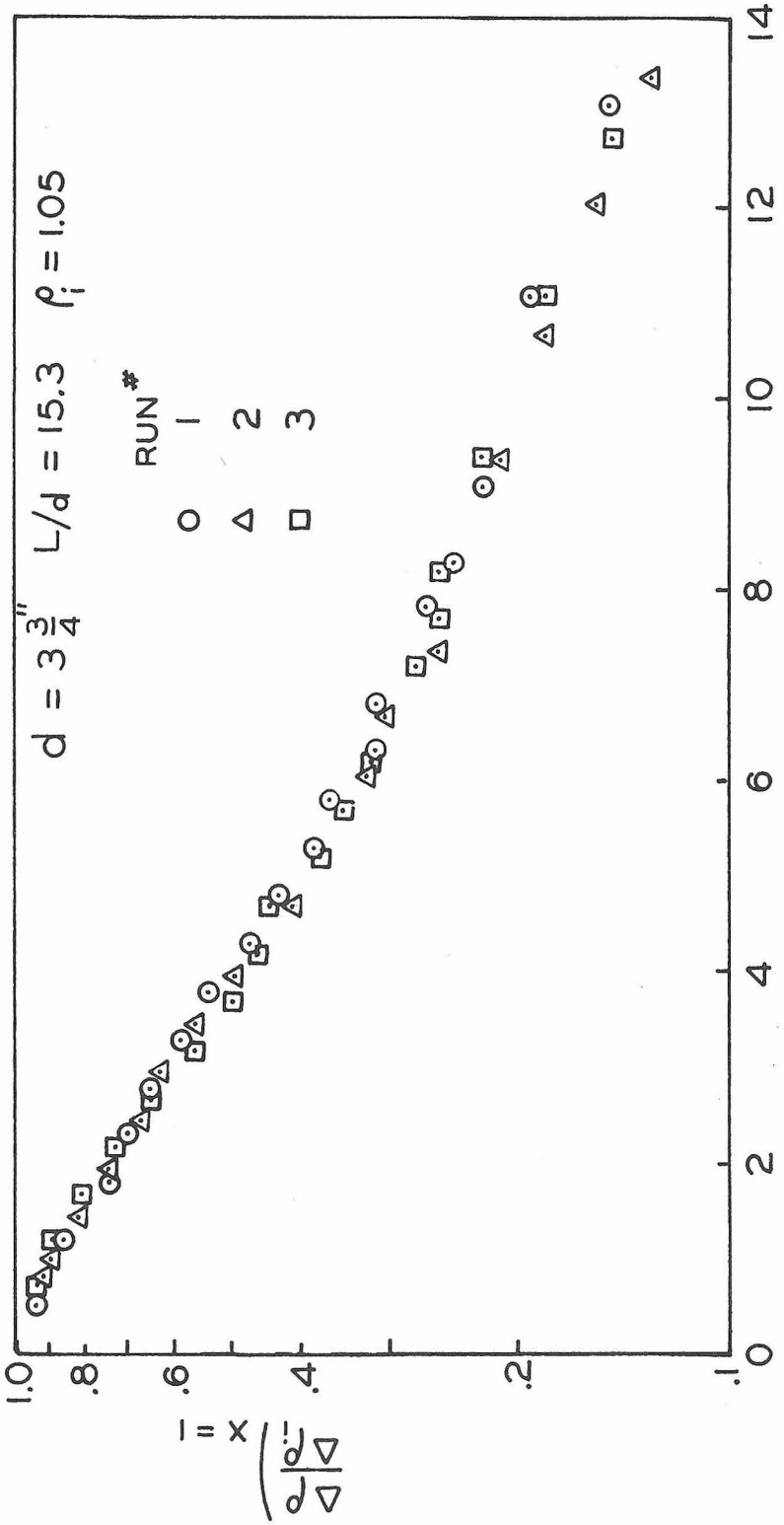

Fig. 5.12 A Typical Plot of Density Versus Time for the Brine Solution Experiments.

6. PRESENTATION AND DISCUSSION OF RESULTS

The results of the small scale models are presented and discussed in this chapter. Each problem stated in Chapter 2 was investigated, but the buoyancy model was considered in more detail than the heat transfer model. This was partly due to the difficulty of performing the experiments in the heat transfer model. All of the results of the buoyancy and heat transfer models are contained in Sections 6.1 and 6.2, respectively. A more critical discussion of all aspects of this study is given in Section 6.3.

6.1 Buoyancy Force Model

The buoyancy model was concerned primarily with the mixing phenomena associated with natural convective flows in vertical ducts and, to a much smaller extent, in stairwell-corridor systems, stairwell - basement systems, and stairway systems. This section contains the results of the small scale models for each system, and they are compared to the analytical results of Chapter 4 in most cases. Since the mixing phenomenon in vertical ducts is fundamental to this subject matter, it was investigated in greater detail than the other problems. The stairwell-corridor and stairwell - basement systems are just extensions of the stairwell problem, and they were not completely solved.

6.1.1 Stairwell (Vertical Duct) System. The major portion of this section deals with the mixing in vertical tubes with an unlimited source of buoyancy where salt-water mixtures were used to produce the unstable buoyancy forces. Initially, dimensional analysis is used to correlate the experimental results and to find the fundamental time

scale, τ. Then the analytical results of Chapter 4 are applied to the small scale models. The latter part of this section contains the results of the gas-gas model, which are compared to the results of the brine solution model.

In finding τ, the arrival times for the various tubes were not taken into account, and this caused some scatter in the results. This point will be discussed in Section 6.1.1.3.

6.1.1.1 Scaling relations. In Section 3.1.1 the density was written as $\Delta\rho/\Delta\rho_i = G(x, \tau)$, where τ is the fundamental time scale that characterizes the mixing phenomena in the stairwell model. From dimensional arguments (Section 3.1), τ was assumed to be a function of $\sqrt{\left(\frac{g}{d}\right)\frac{\Delta\rho_i}{\rho_a}}\ t$ and L/d. However, it is possible for the density ratio to be scaled in some other manner, especially if $\Delta\rho_i >> \rho_a$. Therefore, the simplest form for the fundamental time scale is

$$\tau = \left(\frac{\Delta\rho_i}{\rho_a}\right)^{\beta}\left(\frac{d}{L}\right)^{\gamma}\sqrt{\frac{g}{d}}\ t \quad ,$$

where power laws have been assumed. The exponents β and γ are given in Figs. 6.1 and 6.2, respectively. β is the slope of the line drawn through the data points in the graph of t_ρ versus $\Delta\rho_i/\rho_a$ (Fig. 6.1), i.e., $t_\rho \sim (\Delta\rho_i/\rho_a)^{\beta}$. The time constant, t_ρ, was obtained from a normalization method to scale the experiments for different values of $\Delta\rho_i/\rho_a$. For instance, different curves for $\Delta\rho_i/\rho_a$ can be plotted on the same plot as $\Delta\rho/\Delta\rho_i$ against t. t_ρ is the multiplication factor that moves all of the data points of one curve onto the other curves. $t_{d/L}$ was obtained by this same scaling method, and hence

Fig. 6.2 indicates that $t_{d/L} \sim (d/L)^{\gamma}$.

In Fig. 6.1, β has a value of 1/2. A priori, this value of β was expected because physical arguments necessitate $\frac{\Delta\rho_i}{\rho_a} g$ as a variable, and hence $t_\rho \sim \left(\frac{\Delta\rho_i}{\rho_a} g\right)^{\frac{1}{2}}$. This result indicates that $\Delta\rho_i/\rho_a$ does not appear as an independent parameter here. There is a lot of experimental scatter for $\Delta\rho_i/\rho_a < 2.5$ % (Fig. 6.1). This is partly due to the difficulty of running the experiments for such small initial density differences. Initial disturbances in the system for low values of $\Delta\rho_i/\rho_a$ are more likely to interfere with the mixing process, since the flow is not as turbulent as for larger values of $\Delta\rho_i/\rho_a$. Also, the nature of the mixing process is different for smaller $\Delta\rho_i/\rho_a$ (this will be discussed in detail in Section 6.3). The graphs in Fig. 6.3 were selected to show the accuracy of the 1/2 exponent over a large initial density range. L/d was held fixed, and $\Delta\rho_i/\rho_a$ varied roughly by a factor of 4 for each curve. There is some scatter, but the agreement is good. These plots are typical of all the data taken.

The slope of the curve drawn through the data points in Fig. 6.2 has a value of 9/4. In these experiments, d varied roughly by a factor of 4 1/2, L/d ranged from 7 1/2 to 30, and $\Delta\rho_i/\rho_a$ was held constant at 5 per cent. Note that the data points corresponding to d = 3 3/4" fall slightly below the curve, but a curve with the same slope can be drawn through them. These points could have been displaced due to error in the initial density difference or by some other experimental errors that will be discussed later. Also, note that the data point for the largest tube (d = 7 1/8") coincides with that of the

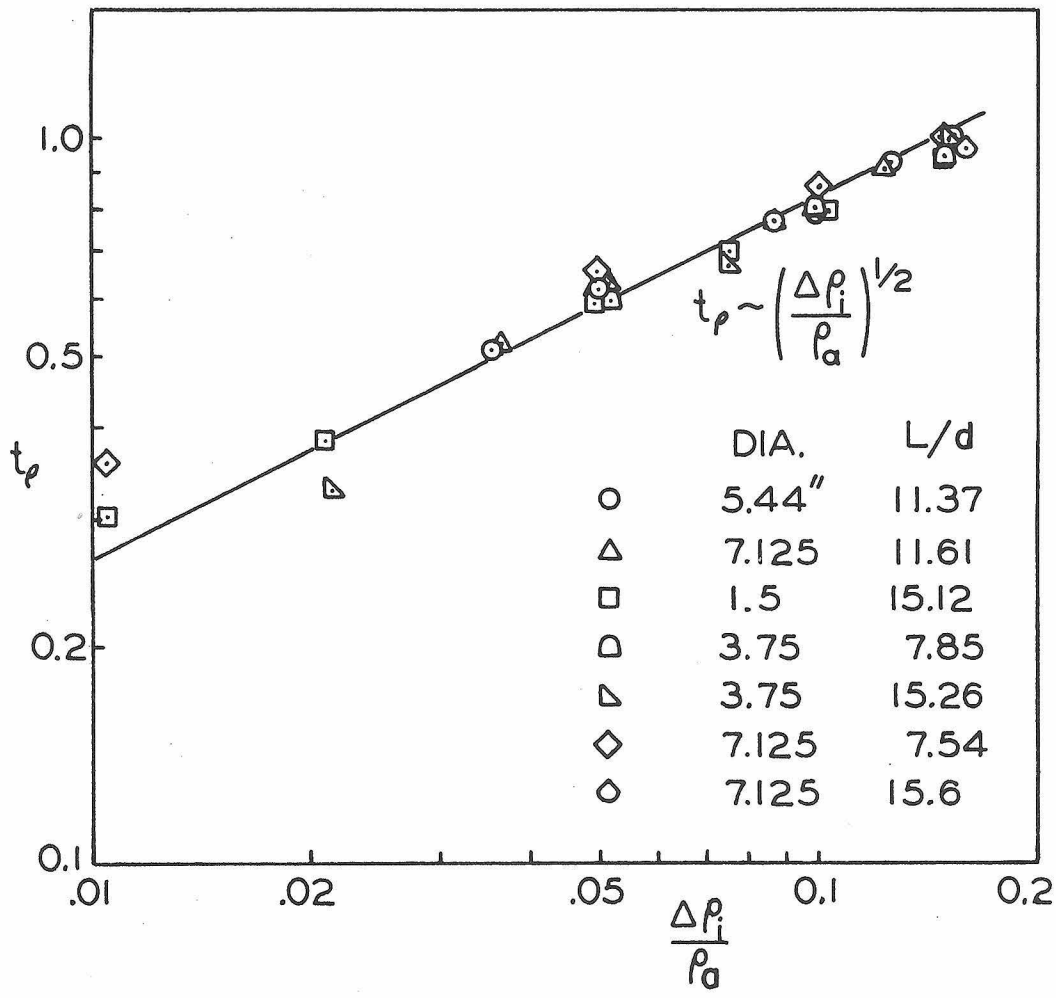

Fig. 6.1 The Dependence of τ on $\Delta\rho_i/\rho_a$.

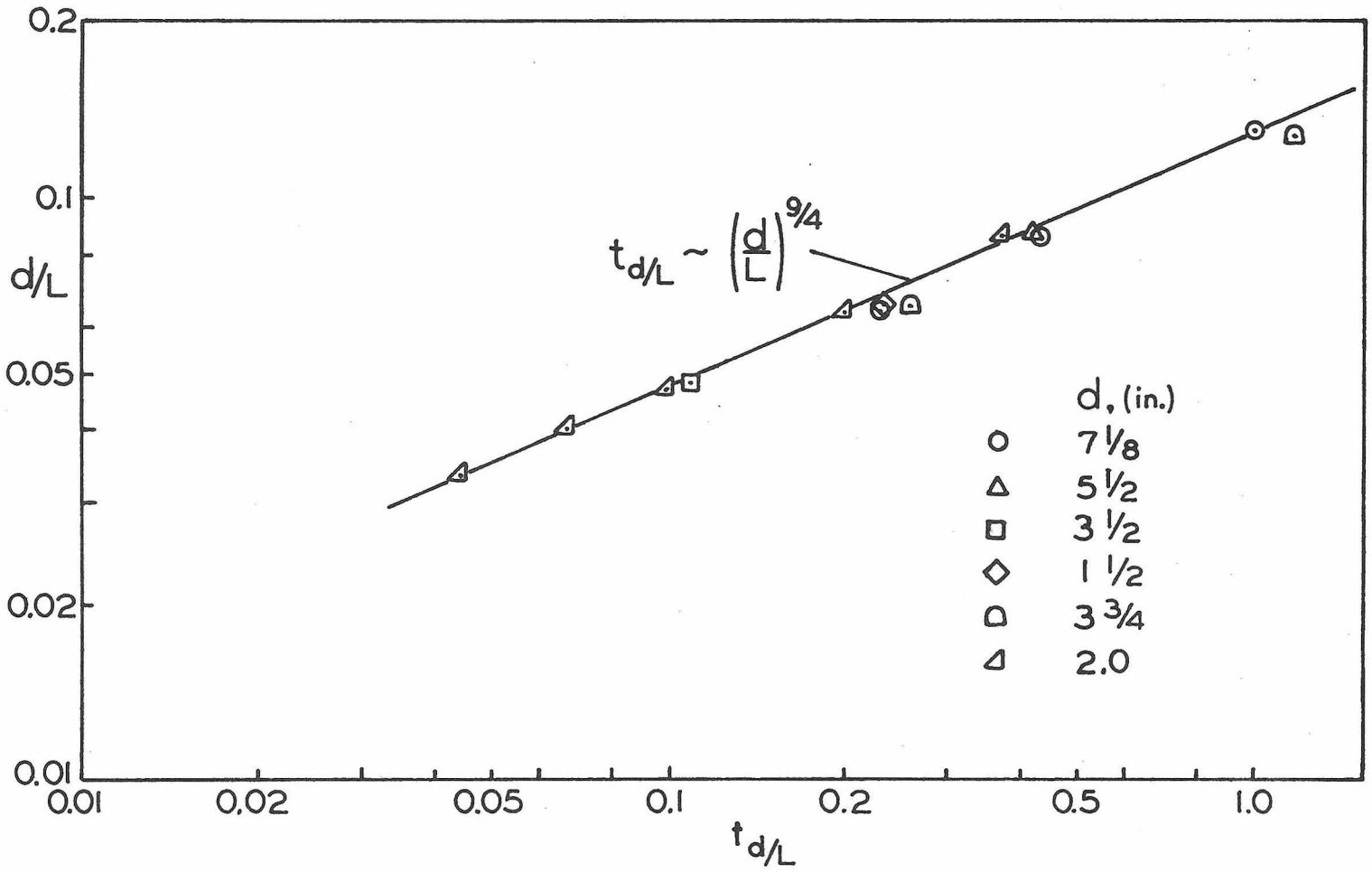

Fig. 6.2 The Dependence of τ on d/L .

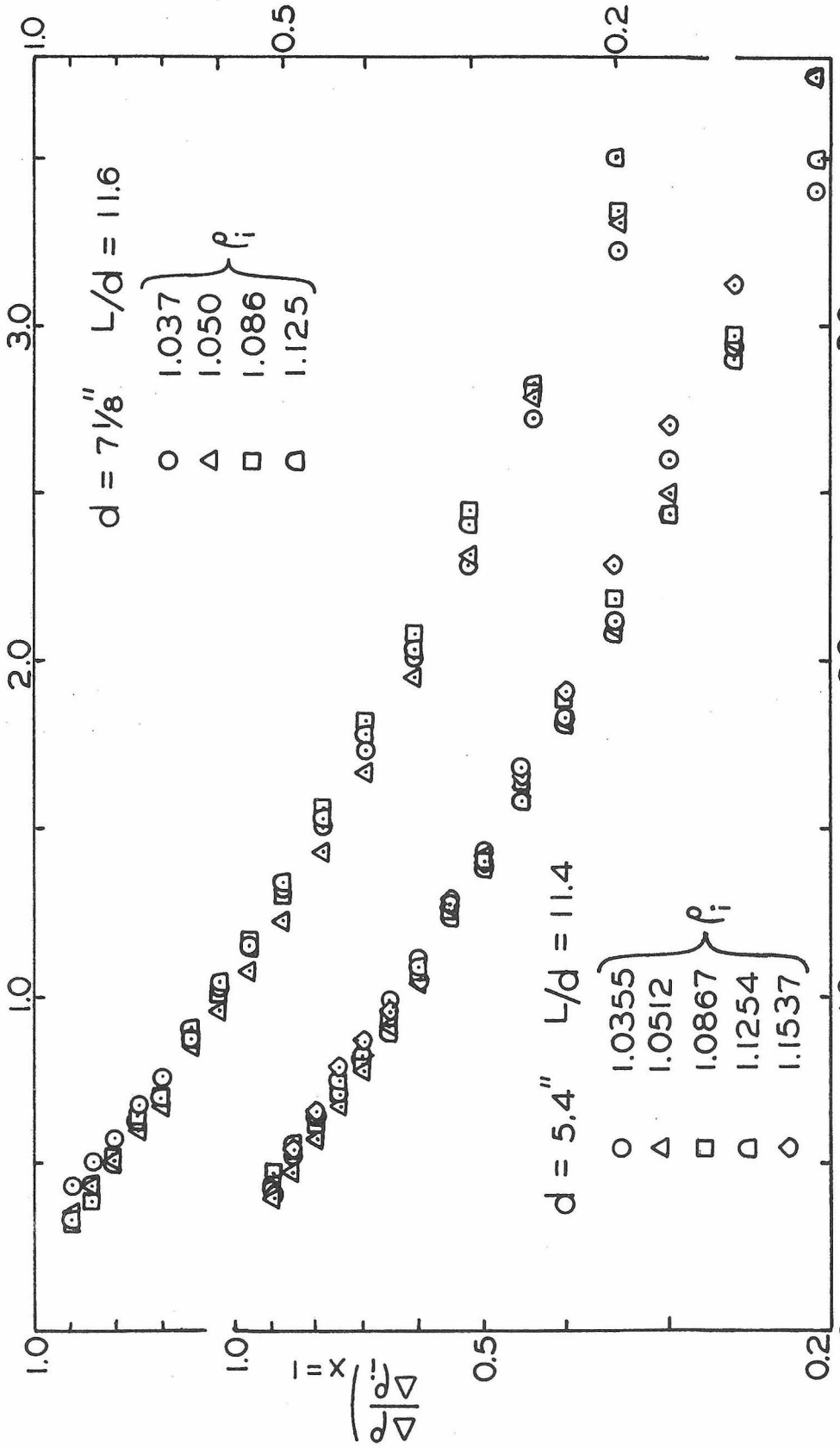

Fig. 6.3 Correlation of Data for Various $\Delta\rho_i/\rho_a$.

smallest tube (d = 1 1/2"). Since the mixing in the 7 1/8" tube can be characterized by a Reynolds number, which is more comparable to those found in fires than any of the other tubes, there is a tendency to give more weight to the larger tubes. However, if viscous effects are present, they are not evident from this plot. Figure 6.4 is a plot that shows how the 9/4 exponent correlates the data for selected tubes. The scatter in the plot increases as τ increases, but the relative error is not large. Other exponents for d/L were used, but $(d/L)^{9/4}$ was the best fit for all of the data.

All of the results presented thus far apply only at the top of the tube (x = 1). The above results indicate that $\theta\{x=1, t\} = H\{\tau\}$, where

$$\tau = \sqrt{\left(\frac{\Delta\rho_i}{\rho_a}\right)\frac{g}{d}}\ \left(\frac{d}{L}\right)^{9/4} t \quad .$$

Since the system is unstable throughout the mixing process, the density at the top of the tube is always a maximum there. Therefore, it was convenient to present the data obtained at different positions along the central axis of the tube in the form of a plot of $\Delta\rho_z/\Delta\rho_L$ against x for different values of time in Fig. 6.5. The plot consists of data taken from three different tubes and also at different positions along the tube. The graph indicates that $\Delta\rho_z/\Delta\rho_L$ is approximately constant for all time at any point along the axis of the tube. The constant, which is a weak function of time, varies about 15 per cent in some of the worst cases. Although there is a certain amount of scatter, a smooth curve can be drawn through the data points in the plot. There was a trend in all of the data that $\Delta\rho_z/\Delta\rho_L$ decreases as time increases. This is shown in the plot by the line

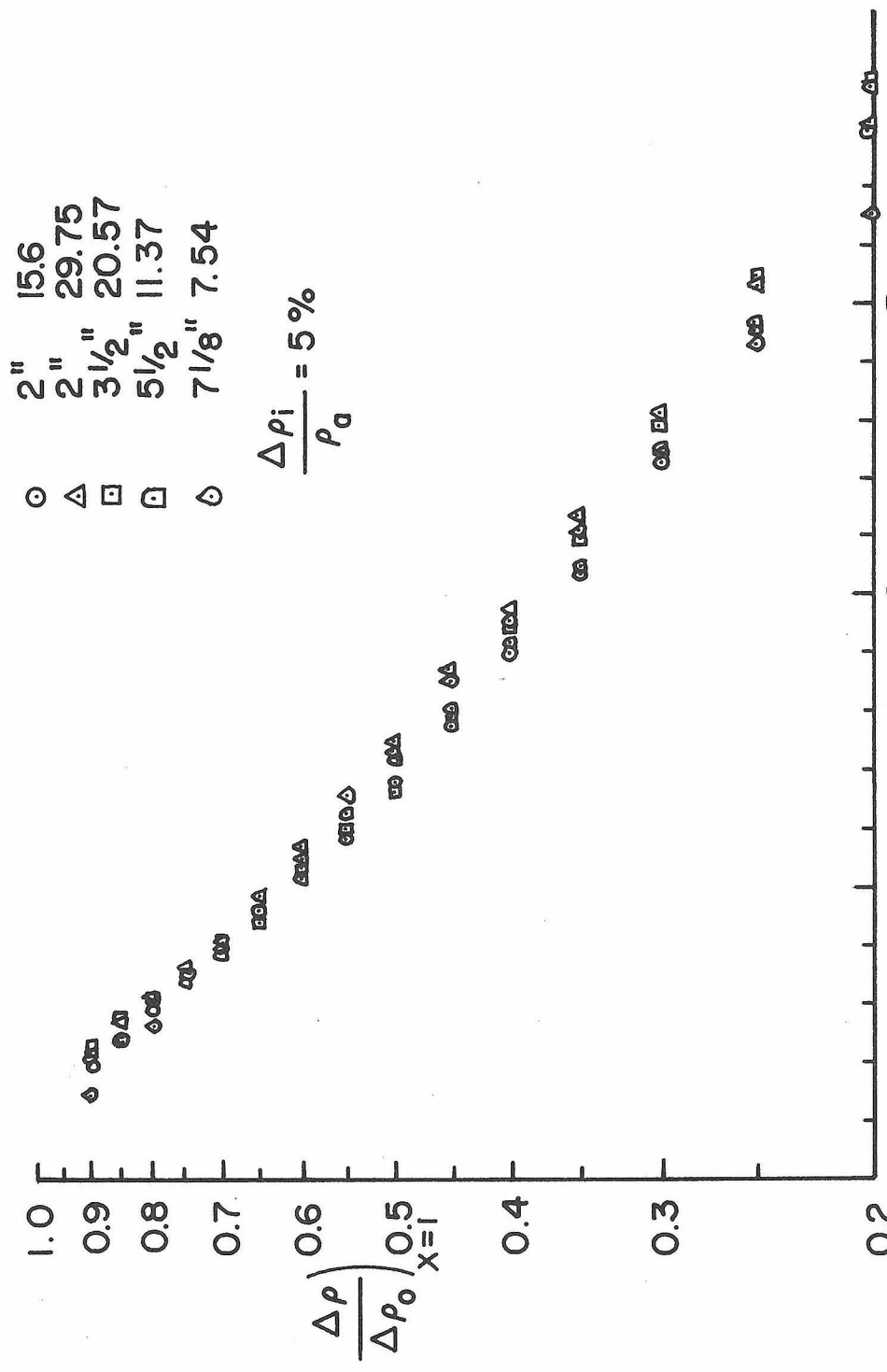

Fig. 6.4 Correlation of Data for Various d/L.

connecting the points. Table 6-1 contains the data shown in Fig. 6.5. We have not determined why this trend exists.

The results of Fig. 6.5 indicate that the density at any cross section below the top surface of the tube is always nearly proportional to the density at the top for all times. This may be stated mathematically as:

$$\Delta\rho_z(\tau) = \Delta\rho_L(\tau)F(z/L),$$

where $F(z/L)$ is the value of the constant in Fig. 6.5. This relation is very important because the solution of the stairwell model (Section 4.1.1) for $\tau > \tau_o$ was based on a separation of variables analysis. The above relation can be reduced to the normalized solution of the stairwell model by letting $\Delta\rho_L = \Delta\rho_i H(\tau)$. Therefore, $G(x, \tau)$ can be written as $G = H(\tau)F(x)$, where $H(\tau)$ is the normalized density at the top of the tube. If this form is correct, it is obvious that the shape of the density profile would not change with time, and that the density at each point in the tube would always be a constant fraction of the density at the top of the tube, $H(\tau)$.

A plot of $H(\tau)$ is shown in Fig. 6.6, which contains data for a wide range of values of both L/d and $\Delta\rho_i/\rho_a$. The scatter is about the same as that in the previous plots where these parameters were varied separately.

6.1.1.2 The empirical diffusion constant, k. In the previous section, the density along the axis of the vertical duct was shown to have the form $\Delta\rho/\Delta\rho_i = H(\tau)F(x)$, where $H(\tau)$ is the value of the density at the top of the tube and $F(x)$ is the shape of the density distribution along the tube axis. The analytical solution of the stair-

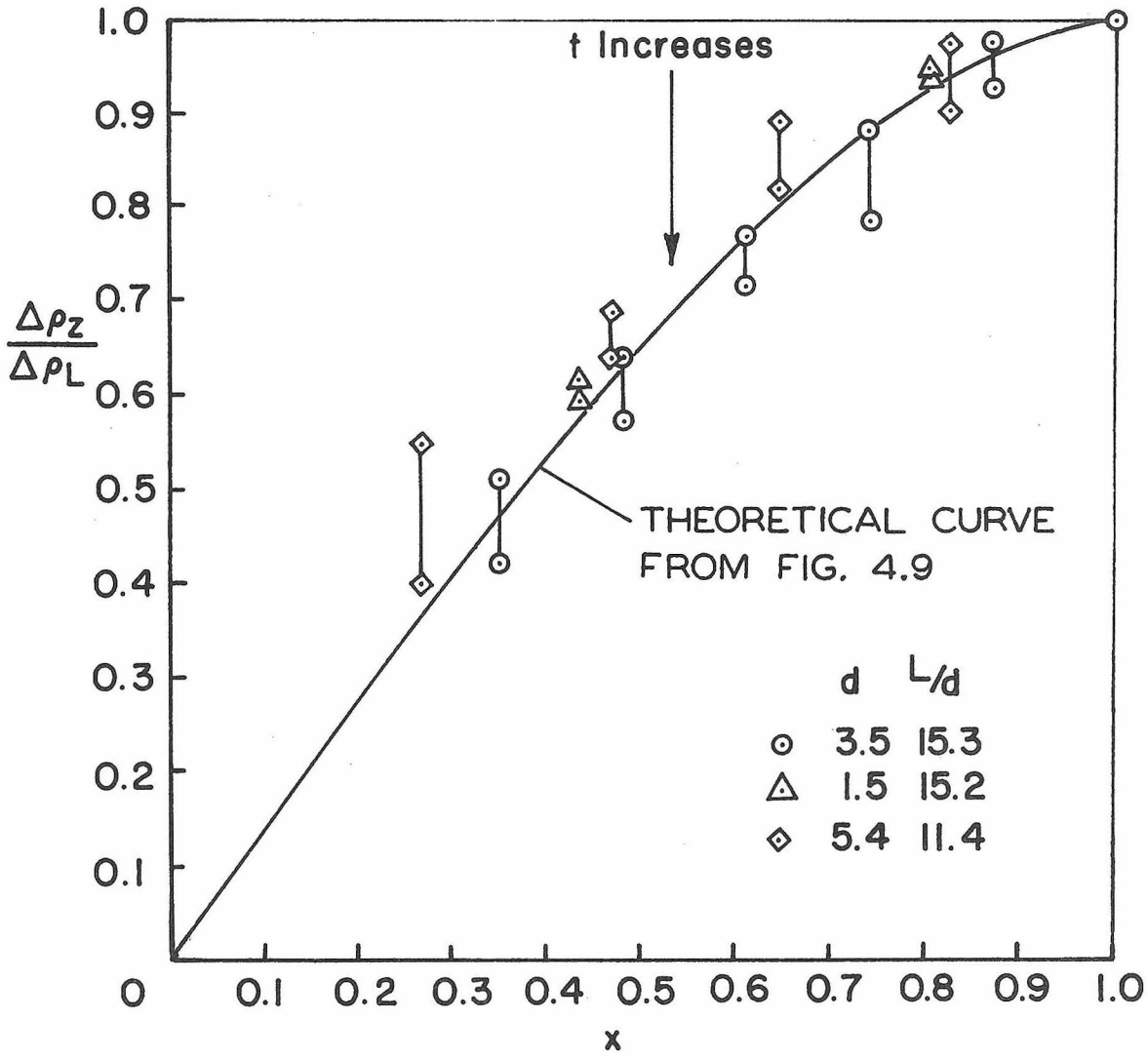

Fig. 6.5 The Density Stratification in Selected Tubes.

Table 6-1. Variation of the Density Stratification, $\Delta\rho_z/\Delta\rho_L$, with Time.

$d = 3\ 1/2''$
$L/d = 15.3$
$\frac{\Delta\rho_i}{\rho_a} = 5\%$

t (minutes)	x	1.5	2	3	4	5	6	7	8
	1.0	1.0	1.0	1.0	1.0	1.0	1.0	1.0	1.0
	.87	.978	.938	.968	1.0	.954	.973	.938	.928
	.739	.841	.826	.855	.88	.837	.811	.812	.786
	.608	.739	.713	.742	.76	.767	.73	.734	.714
	.477	.625	.612	.63	.64	.605	.595	.578	.572
	.347	.512	.463	.50	.48	.465	.433	.421	.375

$d = 5\ 1/2''$
$L/d = 11.4$
$\frac{\Delta\rho_i}{\rho_a} = 5\%$

x	.75	1.0	1.5	2.0	2.5	3.0	3.5
1.0	1.0	1.0	1.0	1.0	1.0	1.0	1.0
.824	.977	.974	.969	.930	.90	.904	.904
.643	.894	.896	.86	.842	.82	.831	.849
.265	.553	.546	.50	.445	.40	.41	.37

$d = 1\ 1/2''$
$L/d = 15.2$
$\frac{\Delta\rho_i}{\rho_a} = 5\%$

x	1.0	2.0	3.0	4.0	5.0
1.0	1.0	1.0	1.0	1.0	1.0
.802	.95	.934	.956	.943	-
.429	.617	.60	.556		.594

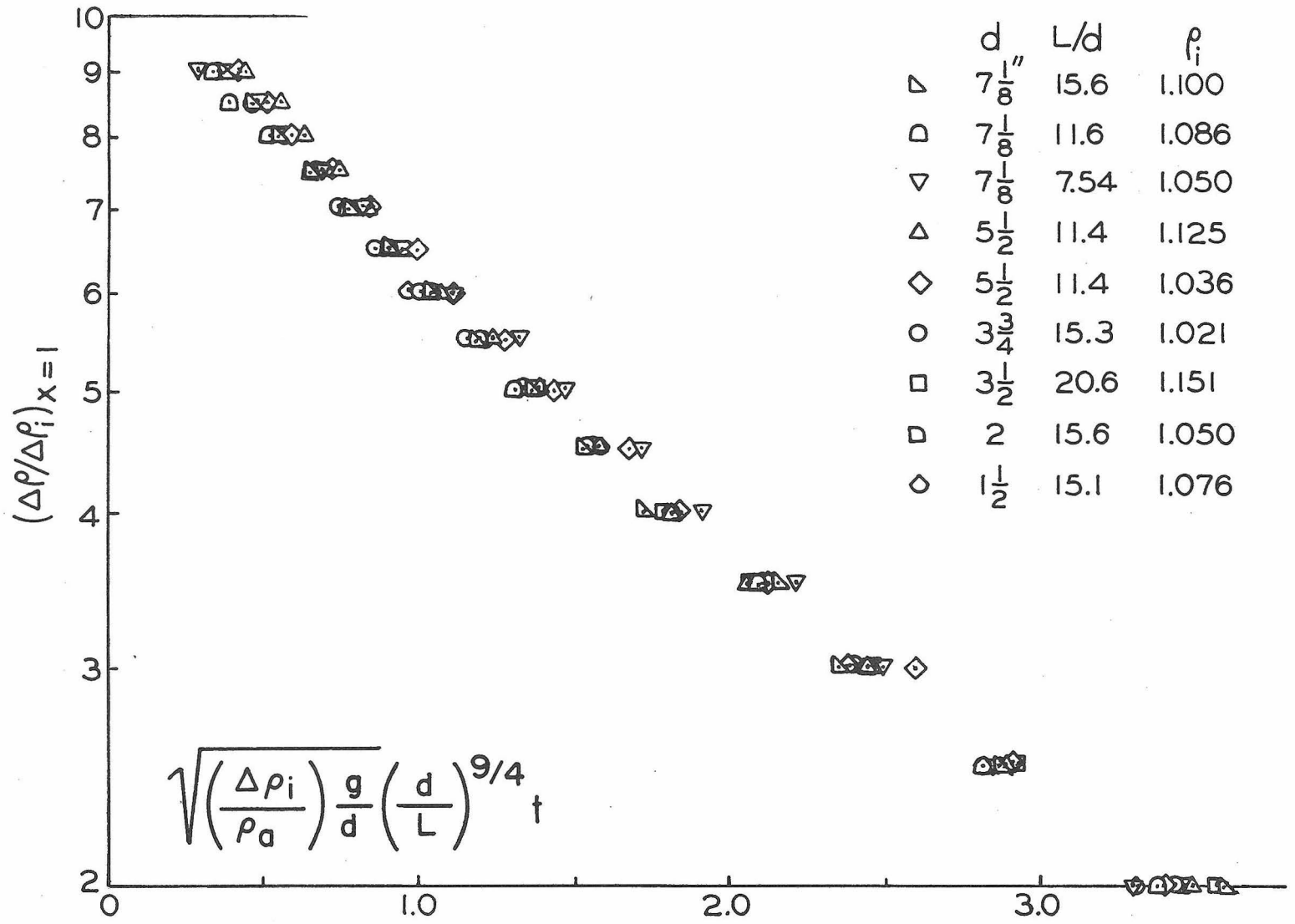

Fig. 6.6 Correlation of Data for Various $\Delta\rho_i/\rho_a$ and d/L.

well model for $\tau \geq \tau_o$ (Section 4.2) has this form also. The theoretical analysis gave the following results:

$$\frac{\Delta\rho}{\Delta\rho_i} = \frac{F(x)}{\left[\frac{\alpha}{2}(\tau-\tau_o)+1\right]^2}$$

where

$$H = \frac{1}{\left[\frac{\alpha}{2}(\tau-\tau_o)+1\right]^2}$$

and $F(x)$ is the density profile in Fig. 4.9 for which $\tau \geq \tau_o$. The diffusion constant, k, was derived in the analysis and found to have the form $k = 0.736(\alpha/2)$. Given these definitions, the above density profile can be written in the form

$$\sqrt{\frac{\Delta\rho_i}{\Delta\rho}F(x)} = \left(\frac{\alpha}{2}(\tau-\tau_o)+1\right) ,$$

which is convenient when analyzing the experimental results because the experimental data should be linear when plotted in this manner, provided that the analytical model is valid. Also, k can be found empirically, since it equals 0.736 times the slope of the linear plot.

Figures 6.7 and 6.8 contain plots of $\sqrt{\Delta\rho_i/\Delta\rho\,|_{x=1}}$ against τ_{avg} for most of the experimental data. τ_{avg} is the average value of τ at a particular value of $\Delta\rho/\Delta\rho_i$ for different values of $\Delta\rho_i/\rho_a$. There were several different initial density differences for each tube, as shown in the previous graphs. In this case, $\sqrt{\Delta\rho_i/\Delta\rho\,|_{x=1}} = 1/\sqrt{H}$, since $F(1) \equiv 1$. Note that all of the curves are linear, as the model predicts. Figure 6.9 is a plot of $\sqrt{\Delta\rho_i/\Delta\rho}$ versus τ for a typical experimental run ($d = 3\ 1/2''$, $L/d = 15.3$, $\rho_i = 1.050$) that shows a linear relationship exists for each value of x, but the slope is different in each case. This is exactly what the theoretical analysis

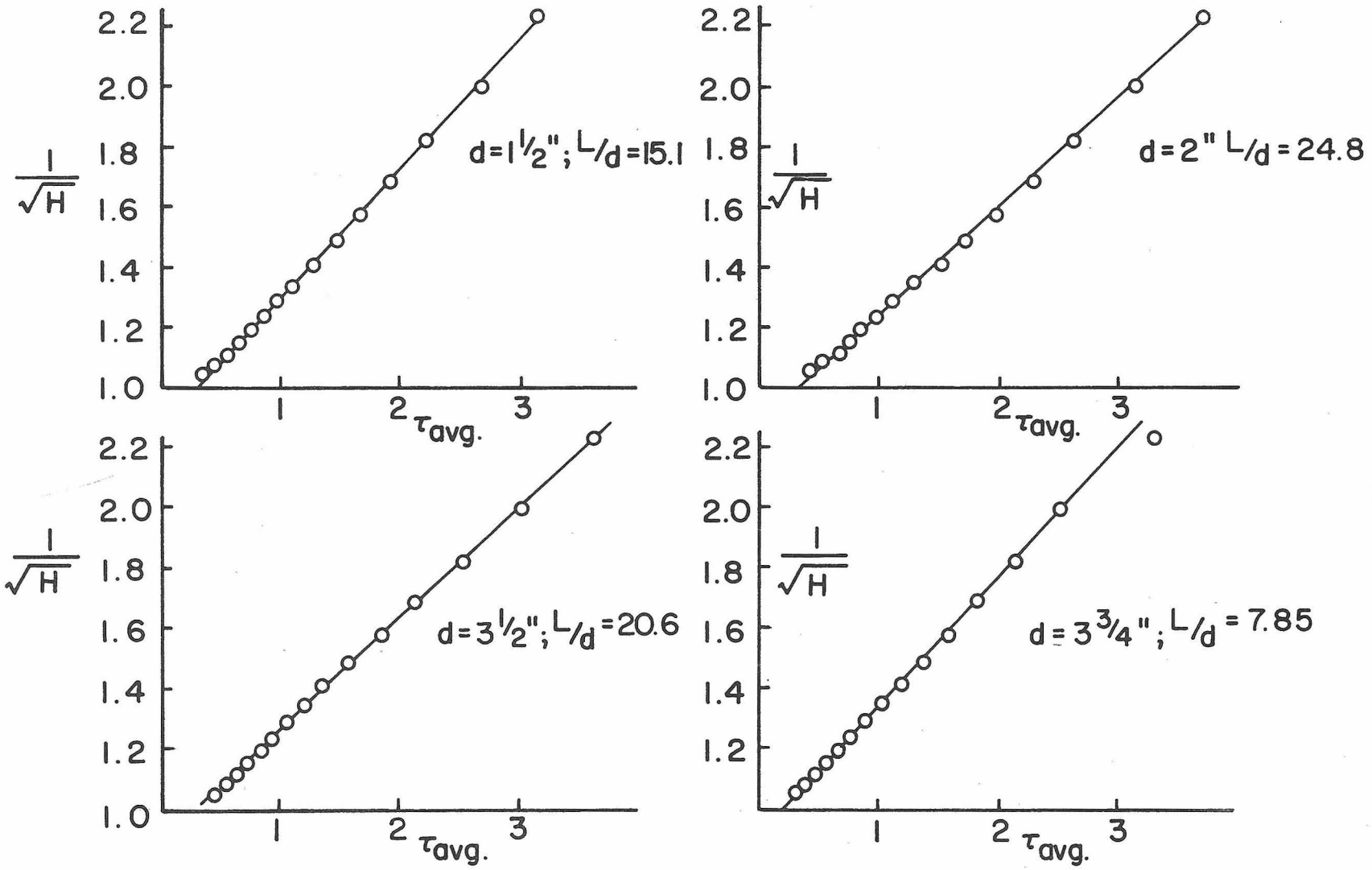

Fig. 6.7 Variation of $\sqrt{\Delta\rho_i/\Delta\rho\big|_{x=1}}$ with τ_{avg} for Selected Tubes.

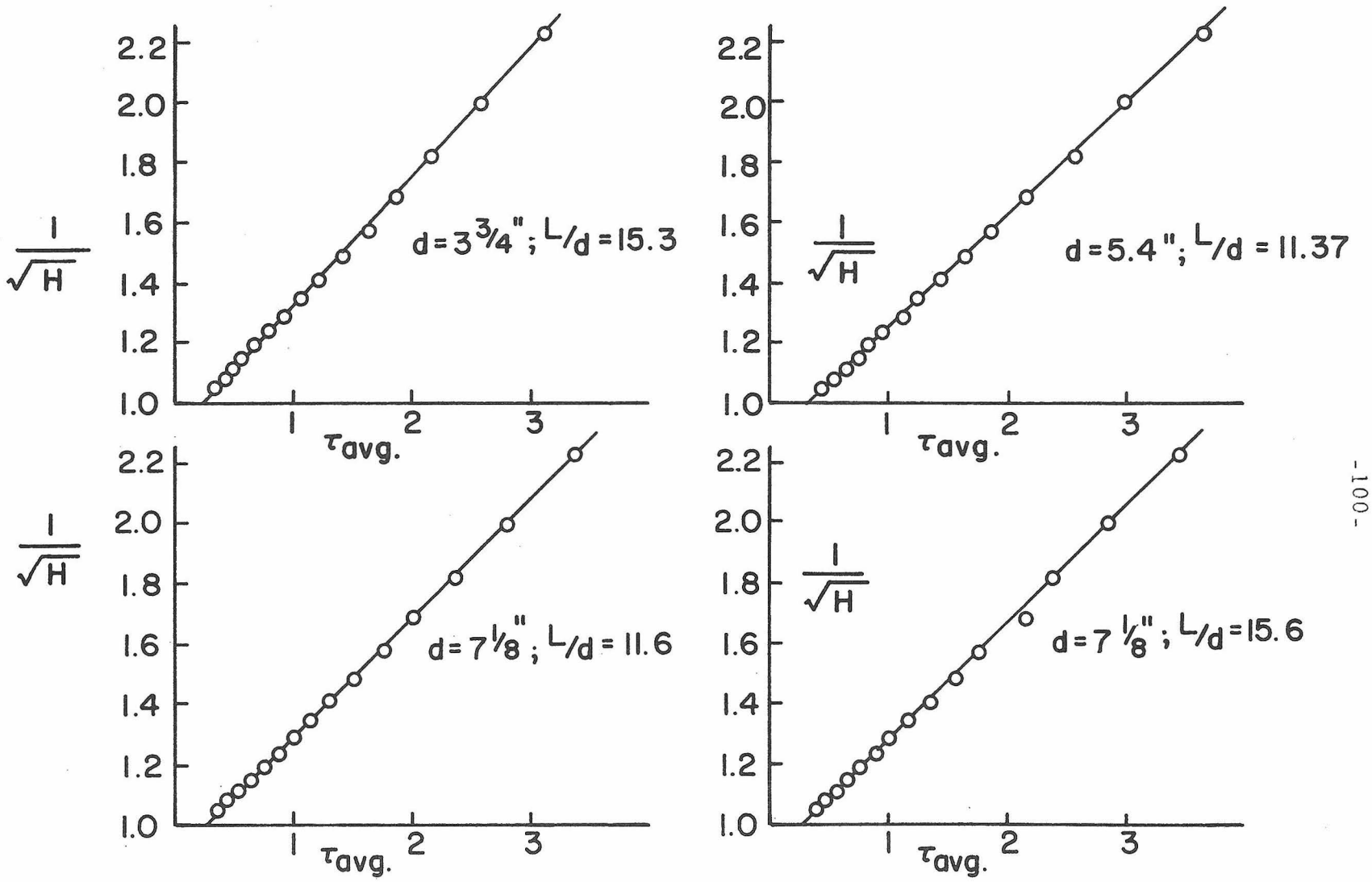

Fig. 6.8 Variation of $\sqrt{\Delta\rho_i/\Delta\rho}\Big|_{x=1}$ with τ_{avg} for Selected Tubes.

predicts because

$$\sqrt{\frac{\Delta\rho_i}{\Delta\rho}} = \frac{\frac{\alpha}{2}(\tau-\tau_o)+1}{\sqrt{F(x)}} ,$$

which shows that the slope of each curve should be $\alpha/2\sqrt{F(x)}$ when the data are plotted in this manner. However, if the data in Fig. 6.9 are plotted as

$$\sqrt{\frac{\Delta\rho_i}{\Delta\rho} F(x)}$$

against τ where the values for F are taken from the theoretical curve (Fig. 4.9), then all of the lines coincide, as shown in Fig. 6.10. Note that for

$$\sqrt{\frac{\Delta\rho_i}{\Delta\rho} F(x)} > 1.0 ,$$

the curves in the plot collapse onto a single curve. However, below this point, each curve for different values of x is different. The reason for this behavior is that $\Delta\rho/\Delta\rho_i = 1.0$ at the instant the initial front reaches the top of the tube (i.e., $\tau = \tau_o$), and the theoretical model is not valid prior to this time.

The turbulent mixing coefficient was defined as follows:

$$E_z \equiv k\sqrt{\frac{g}{\rho_a}\left(\frac{\partial\rho}{\partial z}\right)}\,(d^7L)^{1/4}$$

where k is the diffusion constant. The length scaling in the mixing coefficient is correct because τ was obtained from the theoretical model based on this form of the mixing coefficient which was verified in the previous section. However, if the length scaling was incorrect, k would be a function of L/d. Earlier we stated that k can be found empirically from the linear plots already presented (Figs. 6.7, 6.8,

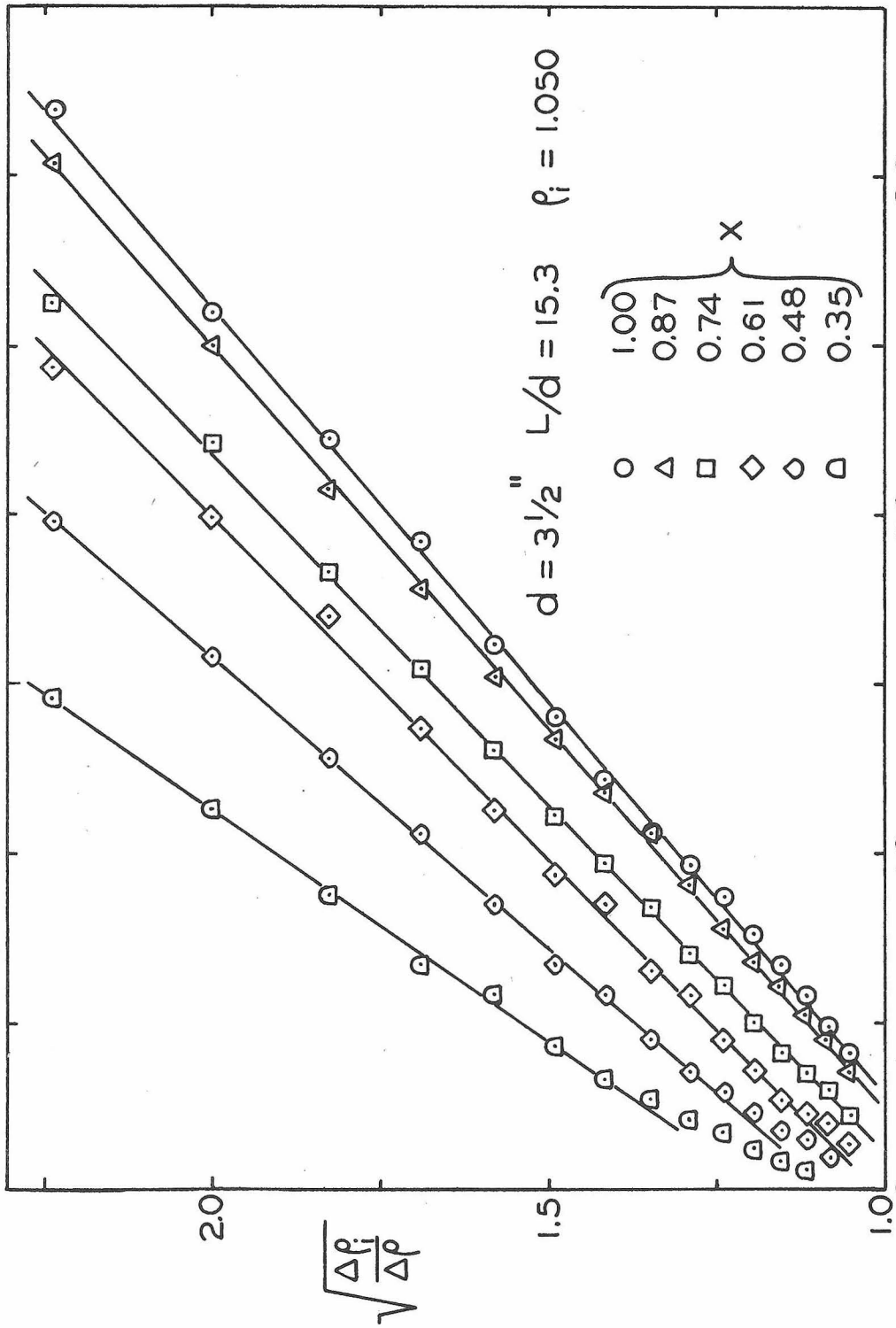

Fig. 6.9 Variation of $\sqrt{\Delta\rho_i/\Delta\rho}$ with $\mp$ for $.35 \leq x \leq 1.0$.

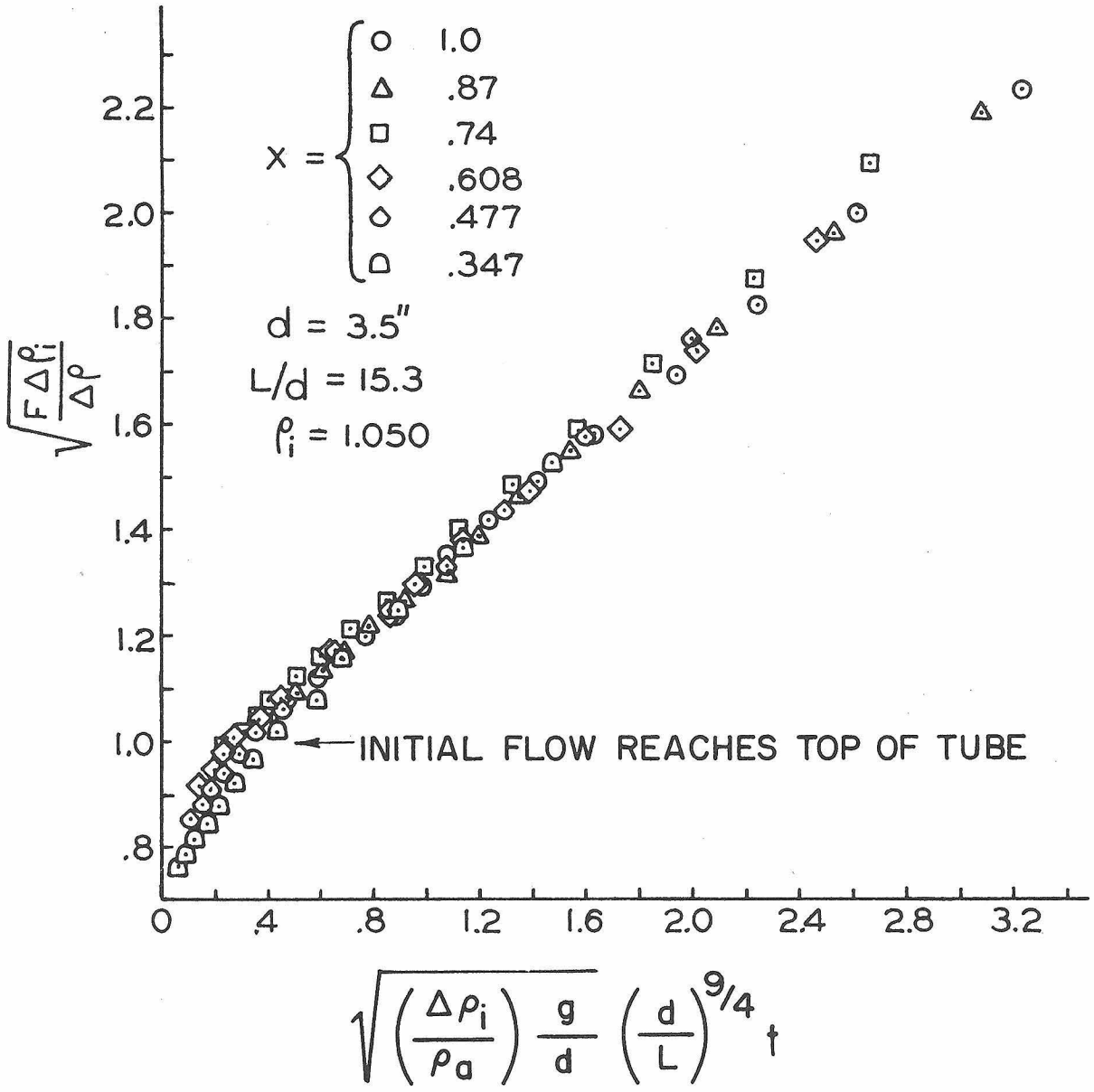

Fig. 6.10 Variation of $\sqrt{F\Delta\rho_i/\Delta\rho}$ with τ for Data from Fig. 6.9.

6.9, and 6.10) since $k = .736(\alpha/2)$, where $\alpha/2$ is the slope of the curve $1/\sqrt{H}$ against τ. The data plotted in Fig. 6.6, which is representative of all the data taken for this system, were plotted as $1/\sqrt{H}$ versus τ in Fig. 6.11. A linear curve was drawn through the data points, and it has a slope of 0.383. Therefore, from the above expression, $k = 0.28$. The scatter in the plot is the same as that in Fig. 6.6.

Note that the intercept of the abscissa in Fig. 6.11 is the theoretical value of τ_o. It has an average value of about 0.27. The actual arrival times for the initial front are listed in Table 6-2. The values in this table indicate that the experimental value of τ_o is a function of L/d. The reason for this behavior will be discussed in the next section.

The agreement between the experimental results and the analytical model is remarkably good. The value of the diffusion constant makes the order of magnitude arguments used in the development of the model more convincing, since it is of the right order of magnitude, i.e., close to one. However, the theory and experiments are not in agreement for small values of x. This is shown in Fig. 6.12, which is a plot of $\sqrt{\frac{\Delta\rho_i}{\Delta\rho}}\,F(x)$ versus τ for one of the short tubes (d = 5.4", L/d = 10.9, and $\rho_i = 1.052$) where experimental data were taken for small x. In this graph, F(x) is not large enough for small x in order to make the data points fall onto one curve. This can be explained by noting that the theory assumes $\rho = \rho_a$ at $x = 0$, which is not exact in the experimental model. Since the diluted brine solution ($\rho > \rho_a$) leaves and the tap water ($\rho = \rho_a$) enters the tube simultaneously, the

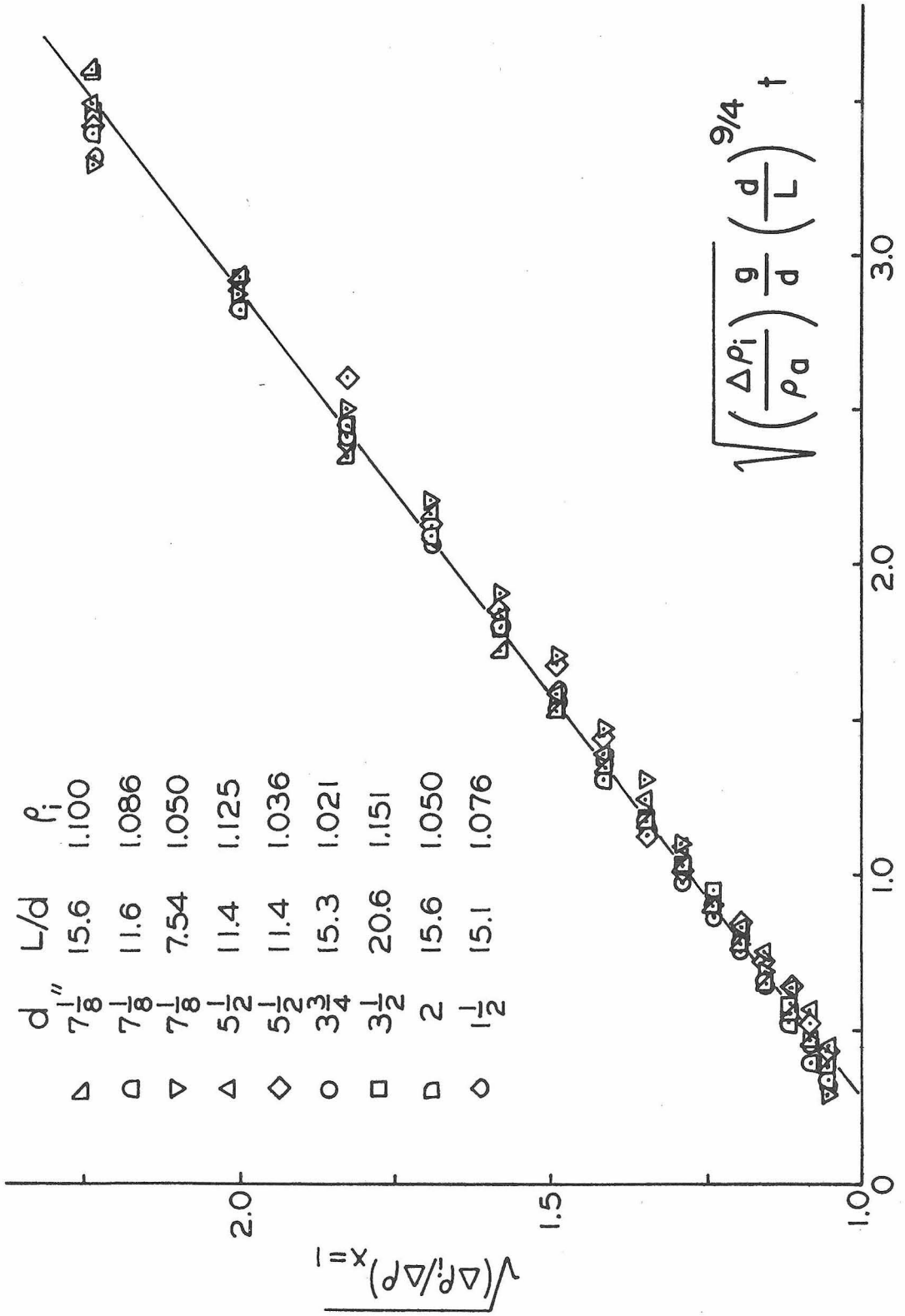

Fig. 6.11 Variation of $\sqrt{\Delta\rho_i/\Delta\rho}\Big|_{x=1}$ with τ for Data from Fig. 6.6.

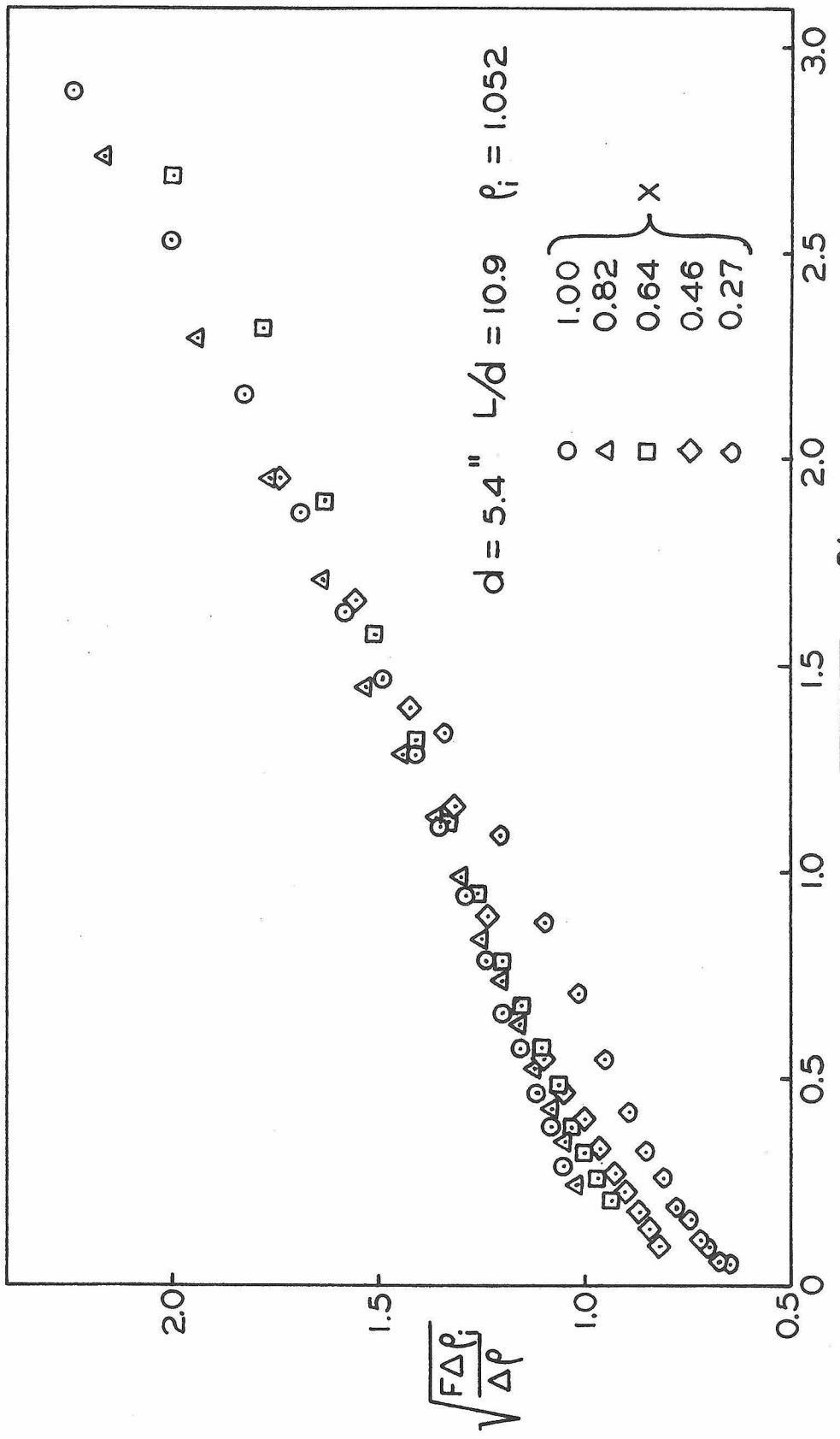

Fig. 6.12 Variation of $\sqrt{F\Delta\rho_i/\Delta\rho}$ with τ.

density at $x = 0$ is the average density of the two solutions, and hence is greater than ρ_a. The data suggest that this boundary condition should be applied at an effective tube inlet which would lie a few diameters below the real inlet.

In essence, if the inlet of the tube is considered to lie one diameter below the real inlet (i.e., d is added to L in order to increase the length of the tube), then $\sqrt{F(x)}$ increases for all x, but the increase is much larger for smaller values of x than for larger values because the density distribution is flat near $x = 1$ (see Fig. 4.9). The net effect of adding length to the tube is to move the lower curves for smaller x (Fig. 6.12) onto the rest of the curve without changing the slope of the upper curves a great deal.

The effective length of the tube is probably near L+d, but the exact value was not found because of the lack of data for small values of x. The data for small x were difficult to analyze without the use of digital methods because the turbulence intensity increases as x approaches zero and fluctuations as large as 10 per cent were present for $z/d < 3$.

6.1.1.3 Propagation of the initial front. In the theoretical model for the initial time period, $\tau < \tau_o$ (Section 4.2.2.2), a self-similar and an integral solution were found. The mixing coefficient in each case was proportional to $\sqrt{\partial\rho/\partial z}$, but the length scaling was changed in order to examine several approaches and because it is not understood how the mixing coefficient should be scaled. The mixing coefficient used in the integral solution was exactly the same as that for $\tau \geq \tau_o$. However, the mixing coefficient in the self-similar solu-

tion was taken to be independent of L or front location. The solutions obtained in both cases were approximately equivalent; that is, the solutions predicted that the location of the front, z_f, depended on the time as $z_f \sim t^{2/5}$ for the self-similar solution, and as $z_f \sim t^{4/9}$ for the integral solution. Thus, the predicted exponents differ by about 10 per cent.

The characteristic time scale in each of the theoretical models for the initial time period was defined as follows:

$$\tau' \equiv \sqrt{\left(\frac{\Delta\rho_i}{\rho_a}\right)\frac{g}{d}}\; t \;,$$

which is obviously not a function of the tube's length.

Figure 6.13 contains a plot of the position of the front, z_f, against τ' for a wide range of experimental runs. The correlation is good for $z/d > 5$, and a wide range of parameters is covered by the data.

The scatter for small z/d was expected because of the experimental error during the development of the initial front. That is, when the plug was removed from the inlet of the tube in order to start the experiment, tap water rushed in to fill the void left by the plug. The removal of the plug aided the mixing process by increasing the turbulence in the system and hence decreasing the speed of the front during its initial stages. This is shown in the plot, because the times corresponding to most of the data points for $z/d < 5$ are too large. The graph in Fig. 6.13 shows that the propagation of the initial front is independent of the tube's length. Nearly all of the data in this plot represent experiments which were aimed at determining the

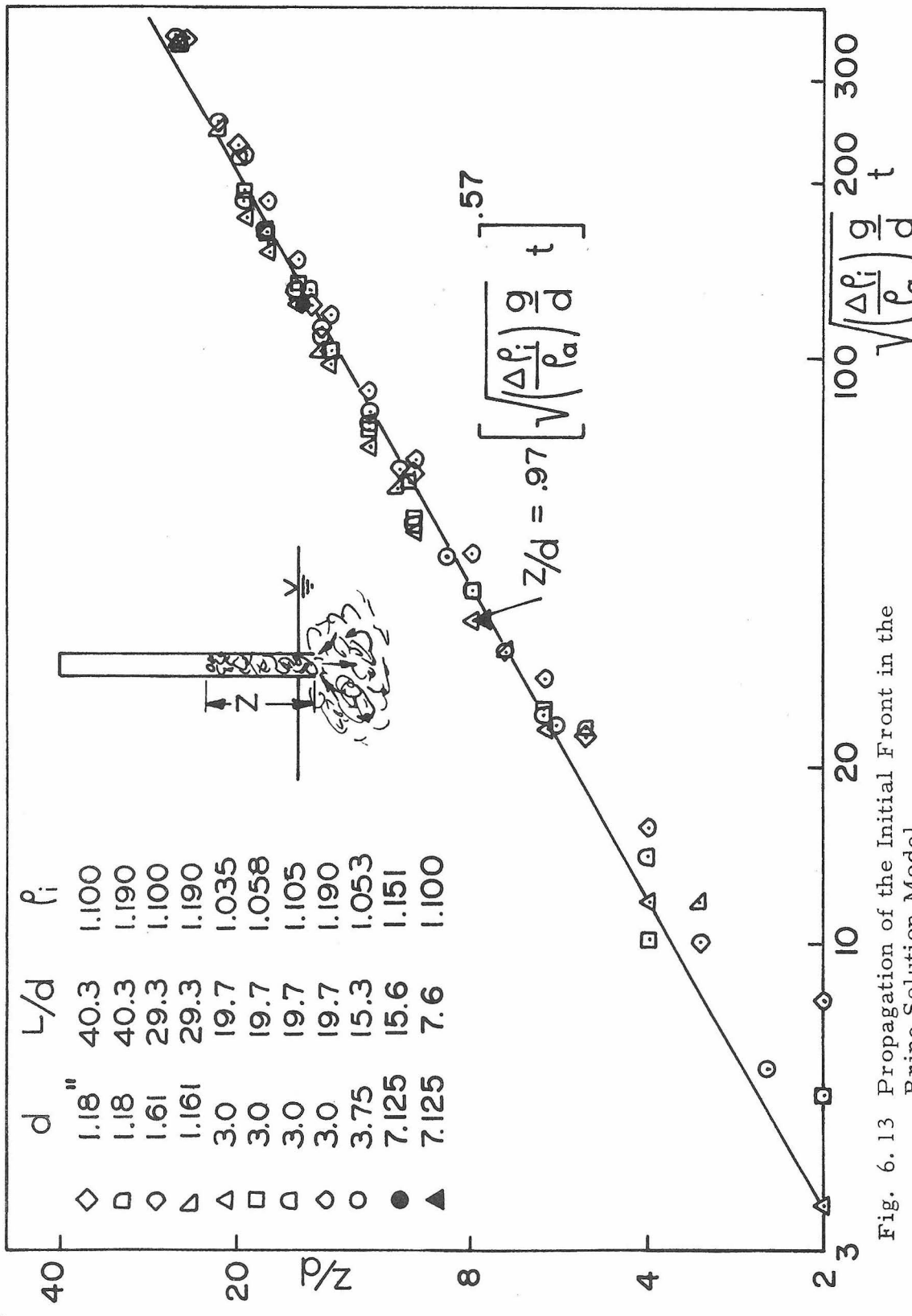

Fig. 6.13 Propagation of the Initial Front in the Brine Solution Model.

speed of the initial front, and to facilitate these measurements tubes with $L/d \geq 15$ were used. However, the arrival times for the tubes used to find τ for which $L/d \leq 15$ are plotted also in Fig. 6.13. The values of these particular points are listed in Table 6-2, and they are in agreement with the rest of the data.

The propagation of the front can be described by the relation

$$z_f \sim t^{3/5} ,$$

which is faster than that predicted by either of the analytic solutions. This means that the proposed mixing model for $\tau < \tau_o$ is not valid. However, the characteristic time scale suggested by the analysis is correct.

The above results indicate that the mixing mechanism for $\tau < \tau_o$ and for $\tau > \tau_o$ may be different because the characteristic time scale for each period is different. Thus, the time scale corresponding to the initial period before the front reaches the top of the tube is

$$\tau' \equiv \sqrt{\frac{\Delta\rho_i}{\rho_a} \frac{g}{d}}\ t ,$$

and the time scale for the period following the arrival of the front is

$$\tau \equiv \sqrt{\frac{\Delta\rho_i}{\rho_a} \frac{g}{d}} \left(\frac{d}{L}\right)^{9/4} t .$$

This result has an impact on the analysis of the experiments discussed previously for which we examined the phenomena for $\tau > \tau_o$. The data for this period were presented as values of θ versus τ rather than $\tau - \tau_o$. Since τ_o values depend on L/d, the difference between τ and $\tau - \tau_o$ will change between experiments as L/d is

Table 6-2. Arrival Times for the Initial Front

	ρ_i	t_o (sec)	$\tau_o \equiv \sqrt{\frac{\Delta\rho_i}{\rho_a}\frac{g}{d}}\left(\frac{d}{L}\right)^{\frac{9}{4}} t_o$	$\tau_o' \equiv \sqrt{\frac{\Delta\rho_i}{\rho_a}\frac{g}{d}}\, t_o$	
d = 1 1/2" L/d = 15.1	1.021	42	.216	97.1	
	1.050	26	.207	93.0	
	1.076	22.5	.220	98.9	
	1.102	21	.238	107.2	
	1.150	17.5	.241	108.5	
d = 3 3/4" L/d = 7.8	1.052	15.5	.348	35.8	
	1.102	11.5	.362	37.3	▲
	1.151	10.1	.368	37.9	
d = 3 3/4" L/d = 15.3	1.021	83	.254	117.5	
	1.052	46	.229	106.0	
	1.076	40	.242	112.0	
	1.099	35	.242	112.0	
	1.151	28	.240	111.2	
d = 7 1/8" L/d = 15.6	1.050	71.5	.243	121.0	●
	1.100	51.5	.247		
	1.151	42	.248		
d = 7 1/8" L/d = 7.6	1.0105	36	.288	27.6	
	1.050	26.5	.454	43.5	
	1.100	15.5	.383	37.0	▲
	1.150	13.3	.403	38.6	

Note: t_o is the physical time necessary for the initial front to reach the top of the tube. Also, the values of τ' plotted in Fig. 6.13 are represented by the symbols opposite them.

changed, and consequently some scatter is introduced in the curves such as those shown in Fig. 6.11. The arrival times for some of the experimental data are given in Table 6-2, where both time scales are presented for selected data. Note that for the arrival time data shown in Table 6-2, values of τ_o vary by about less than $\pm$ 0.1, and hence the scatter will be of this order.

6.1.1.4 Gas - gas experiments. The initial density differences between the gas mixtures and air were much greater than those used in the brine solution model. We pointed out in Section 4.1 that the mixing (when visible) in the gas-gas experiments was very turbulent and had characteristics similar to the mixing phenomena observed in the salt-water experiments. The results of the gas-gas model are plotted in Fig. 6.14. L/d and d were fixed in these experiments at 12 and 6", respectively, and the initial density ratio ranged from 0.22 to 4.0. The graph shows that the density correlation (i.e., $\tau \sim \sqrt{\Delta\rho_i/\rho_a}$) is good except for the data points corresponding to the largest density ratio ($\Delta\rho_i/\rho_a = 4.0$) because they are displaced from the rest of the points. Note that a curve with approximately the same slope can be drawn through both sets of points. Also, the curve from Fig. 6.11 that was used to calculate the diffusion constant is drawn in the graph. The general agreement between the gas-gas experiments and the brine solution experiments is good, as indicated by the line. The dashed line in the plot has the same slope as the solid line, but a different value of τ_o. It is a good fit for the results corresponding to a value of 4.0 for $\Delta\rho_i/\rho_a$. The reason why these data ($\Delta\rho_i/\rho_a = 4.0$) are displaced to the right of the other results is not known. Since the

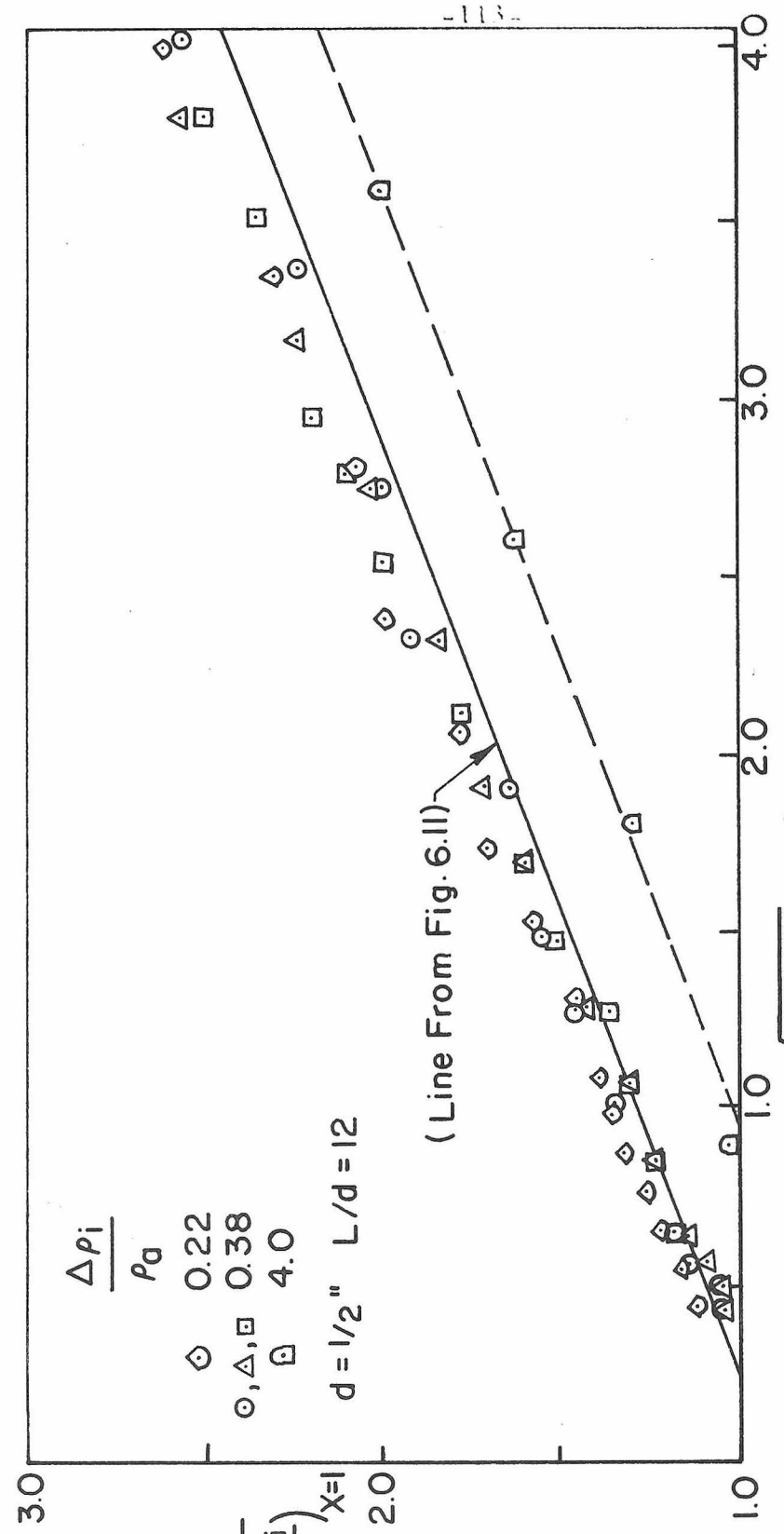

Fig. 6.14 Variation of $\sqrt{\Delta\rho_i/\Delta\rho}\Big|_{x=1}$ with τ for the Gas-Gas Experiments.

mixing rates increase as $\sqrt{\Delta\rho_i/\rho_a}$ increase, the experimental error also increases in this same manner because of the slow response time of the system used to measure the density of the gas mixtures. The density recorded at any time had roughly a 1 1/2 second time lag from its actual value because the gas sample was drawn from the tube to an O_2 analyzer which fixed the response time of the system. This time lag is important in the initial phase of the experiments (especially in those with $\Delta\rho_i/\rho_a = 4.0$, since the characteristic velocities increased by a factor of 4), because the density differences are large, and therefore disturbances propagate rapidly in the vertical tube.

Thus, it is reasonable to conclude from the results in Fig. 6.14 that the mixing phenomena in the gas-gas model are the same as those in the brine solution model. In general, natural convective flows resulting from unstable buoyancy forces in vertical ducts are independent of the fluid used to produce the density differences. Initially, this result was expected because the conservation equations for each model are identical.

6.1.2 Corridors. The vertical tubes in the brine solution model were used to model the movement of hot gases in corridors. They were filled with a dense brine solution and submerged horizontally in a large basin of tap water. The experiment started when the cap on the "open end" of the tube was removed. Tap water rushed in and propagated along the upper half of the tube, while the diluted brine solution exited at the open end. When the front of the less dense solution arrived at the end of the tube, the remaining dense solution in the bottom layer flowed out of the tube. This process took about

the same time as the initial transient period. Then the entire tube was full of the less dense solution.

The movement of the front was timed until it reached the end of the tube. The results are plotted in Fig. 6.15, and indicate that the front propagated at a constant speed. Its speed, v, is as follows:

$$v = 0.45 \sqrt{\frac{\Delta\rho_i}{\rho_a} gd} \quad .$$

Note that the above expression is the same as that used in the dimensional arguments to find the diffusion velocity. Another point worth noting is that very little mixing was observed at the interface of the two-layered flow. Also, these results are in agreement with the work of Benjamin[6].

6.1.3 Stairwell-Corridor System. The model of the stairwell-corridor system consisted of two cylindrical lucite tubes of equal length joined together at right angles. The horizontal end was closed and the inlet was the bottom of the vertical portion. The tube was filled with a dense brine solution, as in the other experiments, and the mixing began when the bottom plug of the vertical tube was removed.

Figures 6.16 - 6.18 are a sequence of photographs of the turbulent mixing that took place in the stairwell-corridor system. Basically, the same mixing mechanism existed in the vertical direction as before, but the mixing was more intense at the top. The momentum of the lighter fluid changed direction at that point and propagated laterally after mixing with some of the heavier solution at the top. This is shown in frames A - H of Figs. 6.16 and 6.17. In frames

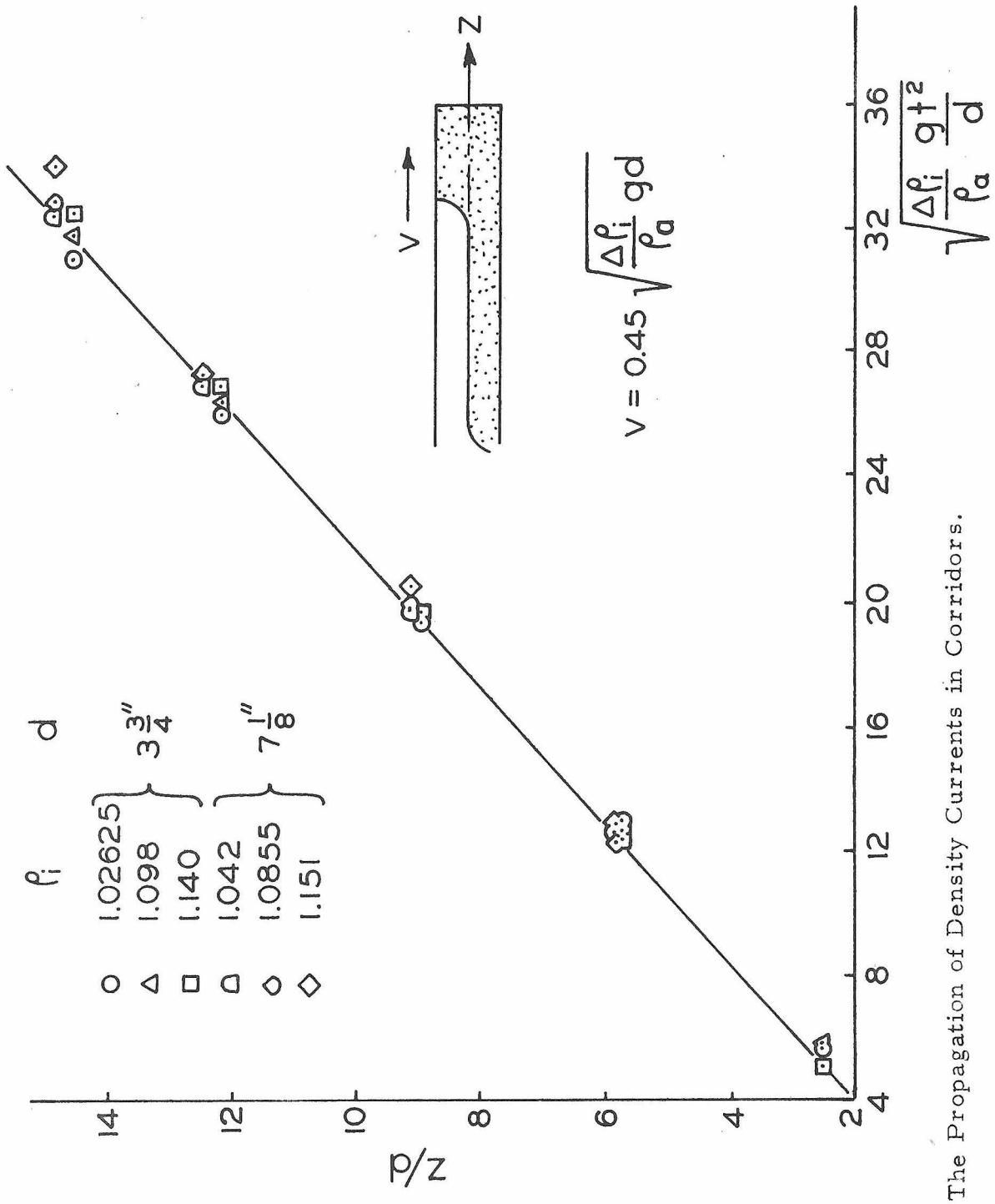

Fig. 6.15 The Propagation of Density Currents in Corridors.

C and D, the less dense fluid has reached the top and is beginning to flow laterally into the horizontal tube. Frames E and F show the development of a two-layered flow system, described in the previous section. At the top of the vertical tube in these photographs, the two fluids are well mixed because of the intense mixing at that point. After the two-layered flow had fully developed in the horizontal tube, frames G and H, the mixing patterns at the top of the vertical tube changed. The momentum of the dense fluid in the bottom layer caused it to pass over the vertical tube and impinge on the far side of it. In essence, this flow pattern increased the mixing at that point.

The less dense fluid in the top layer in the horizontal tube had a well-defined front or head preceding it. The head was identical to that found in density currents[6] of other flows. Also, as expected, we observed very little mixing between the two layers in this flow. Figure 6.18 (frames I - L) shows how the less dense fluid propagated to the end of the horizontal tube and reversed its direction. When the fluid in the top layer struck the end of the tube, an eddy developed at that point. The eddy mixed the fluid in that region and then the adverse pressure gradient, which was very small, caused the fluid to propagate laterally in the opposite direction. This mixing mechanism continued until the system was stable.

Figure 6.19 is a plot of $\Delta\rho/\Delta\rho_i\big|_{x=1}$ against time which compares the vertical tube with/without the horizontal attachment. The addition of the attachment slowed down the mixing process. However, the important point is that the density at the end of the horizontal tube is nearly equal to that at the top of the vertical portion of the tube.

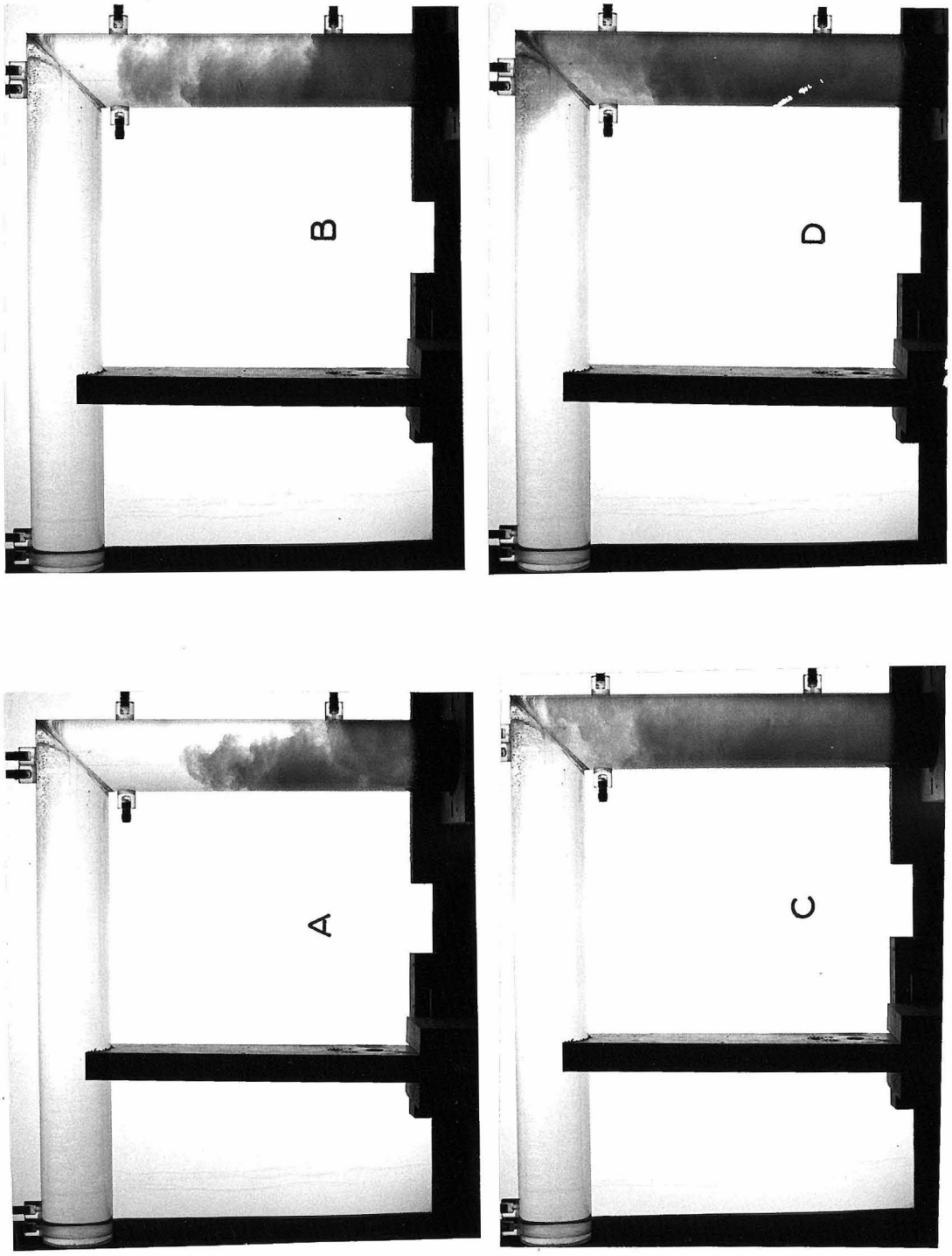

Fig. 6.16 Mixing Patterns in the Stairwell-Corridor System (I).

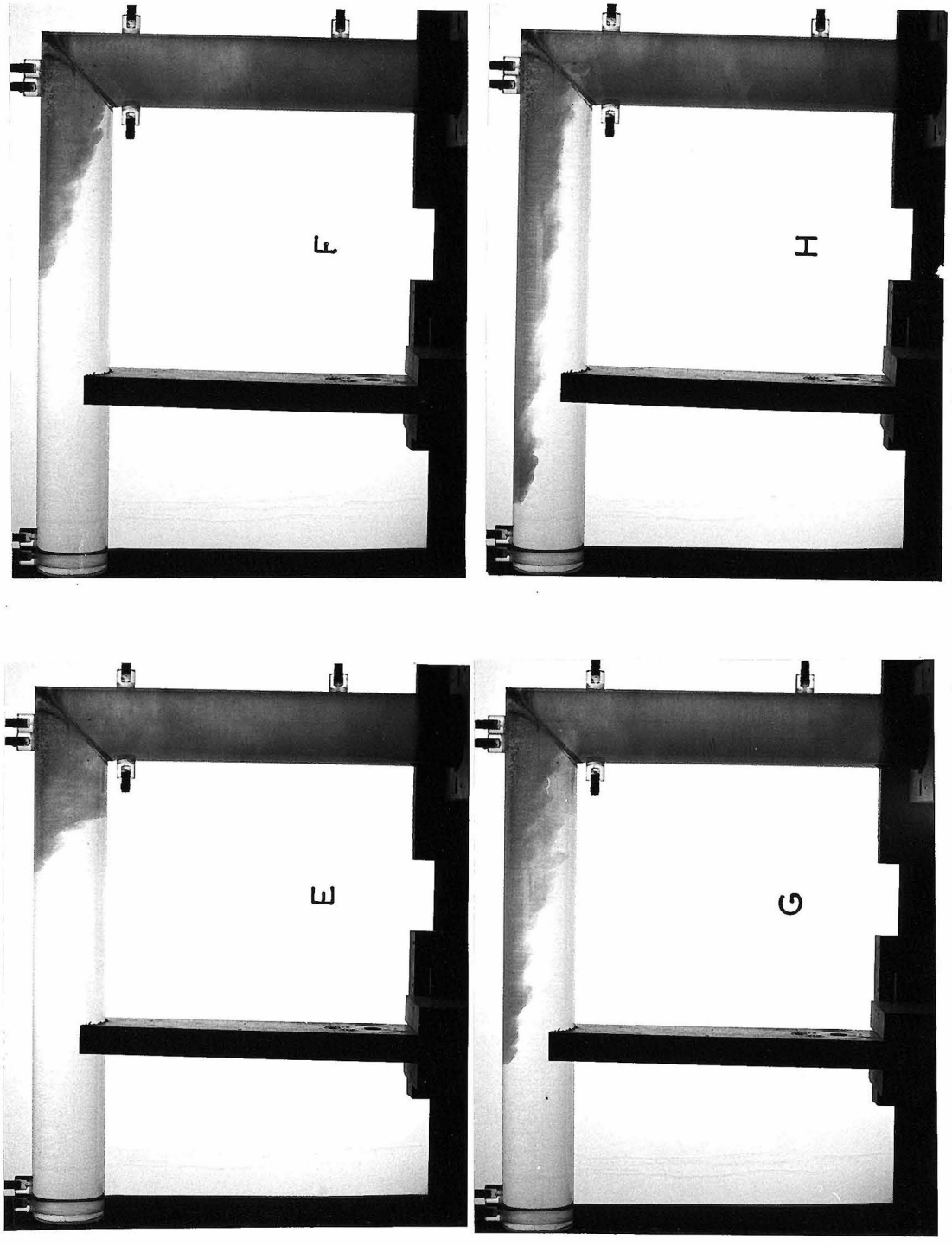

Fig. 6.17 Mixing Patterns in the Stairwell-Corridor System (II).

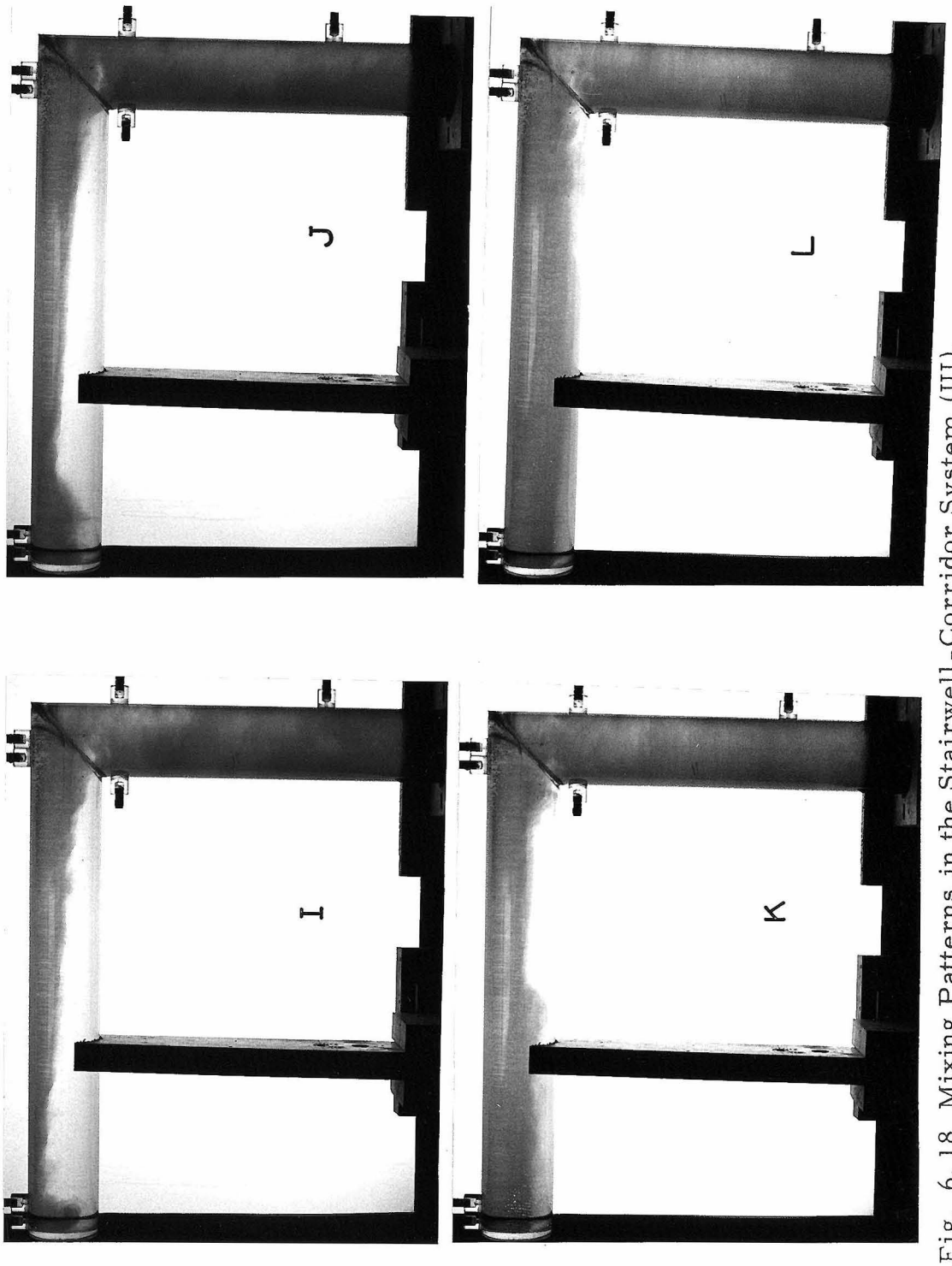

Fig. 6.18 Mixing Patterns in the Stairwell-Corridor System (III).

For small $\Delta\rho/\Delta\rho_i$, the time lag between the density at the two points increased, but not by a substantial amount. A small time lag was expected because the less dense fluid propagated to the end of the horizontal tube and then returned to the same point, where the density had changed slightly. The mixing between the two layers did not affect the stratification in the system. In essence, it appears that the upper portion of the tube system was well mixed. The well-mixed top assumption in Section 4.2.3 was based on this observation.

The theoretical results are applied to the experimental results of the stairwell-corridor system in Fig. 6.20. In this case, the volumes of the horizontal and vertical tubes were equal. The theoretical curve in Fig. 4.10 (based on $V_r = 1$) predicts that $\alpha/k = 3/4$ for this system. Since k is an empirical diffusion constant obtained from the brine solution and gas-gas models, it is the same for this system. Therefore, the slope, $\alpha/2$, of the curve drawn through the data points in Fig. 6.20 should be .105. However, the slope of the line drawn in the graph is approximately twice the predicted value. The reason for this disagreement is not understood. That the general mixing model is correct is suggested by the result that a linear curve can be drawn through the data points. Also, the top boundary condition (well-mixed top) does not change the form of the solution, i.e., $\theta = H(\tau)F(x)$, but it fixes the slope, $\alpha/2$. The increased turbulence at the top of the tube due to the addition of the horizontal attachment may be the reason for the high mixing rate in the small scale model. Previously, we pointed out that the flow mechanism changed at the top of the tube. In the vertical tube system with zero mass flux across the top surface,

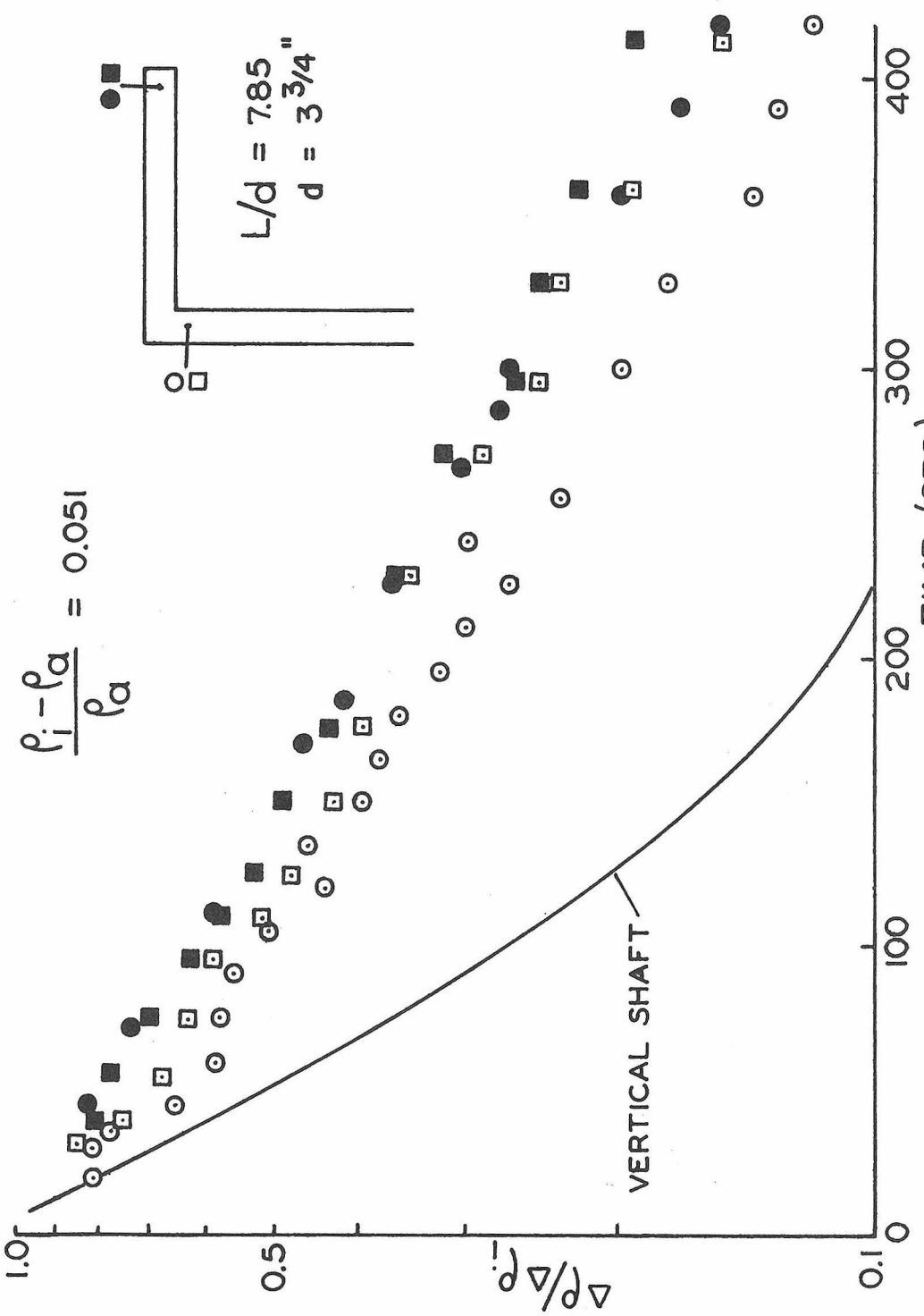

Fig. 6.19 Variation of $\Delta\rho$ with t for the Stairwell-Corridor System.

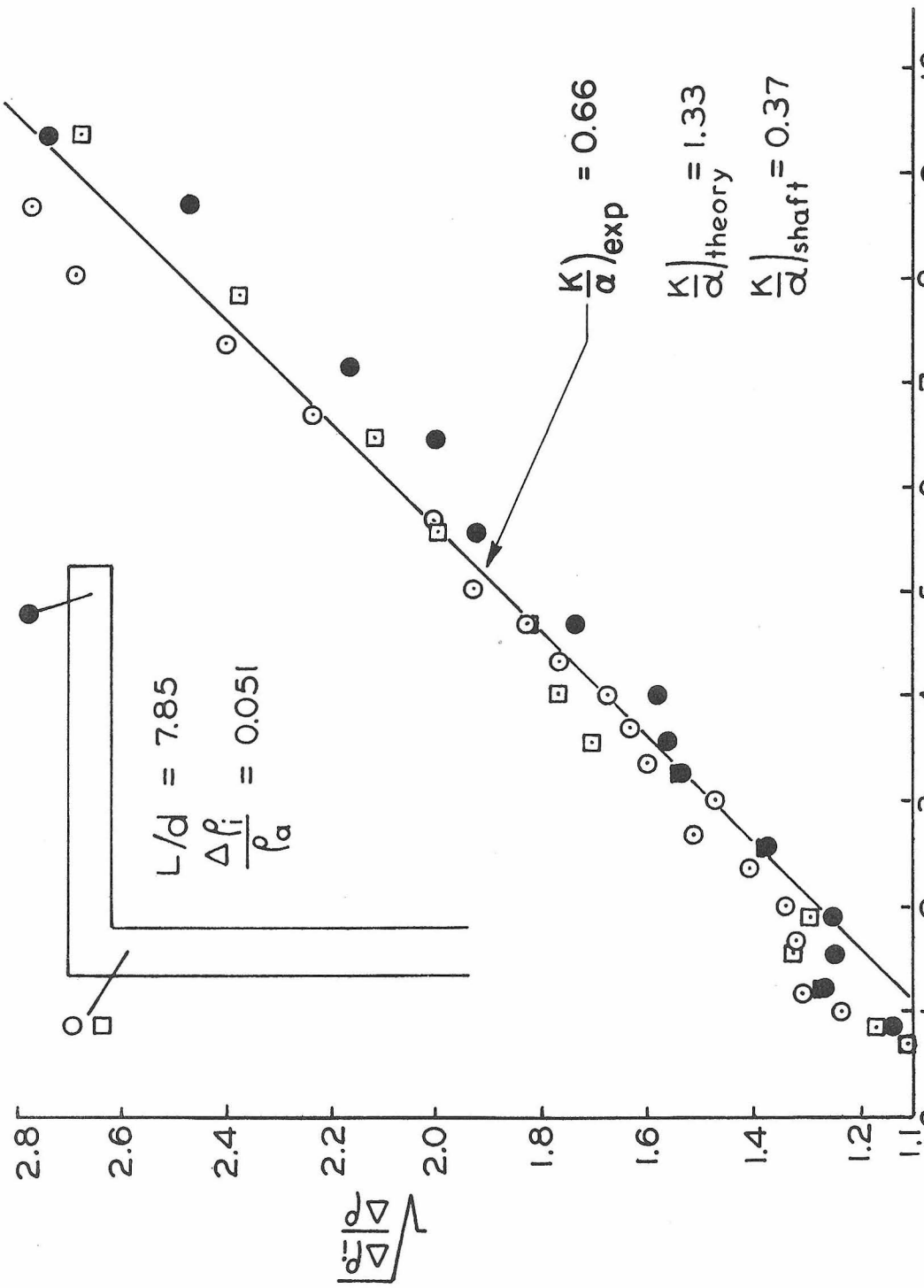

Fig. 6.20 A Comparison of Theory and Experiments for the Well-Mixed Top, $V_r = 1$.

the turbulence was dampened as x increased. However, the turbulence in this case increased as x increased, and the theoretical model could not take this into account. It only allowed mass to diffuse out of the top volume. Also, it is possible that the horizontal attachment caused the effective length scaling in τ to change. For example, instead of being proportional to $(d/L)^{9/4}$, the exponent could have increased to 5/2, which would increase the mixing rate by a factor of 1.7. Or a 35 per cent increase in effective length would give the same change. Sufficient data were not taken in order to clarify this point.

6.1.4 Stairwell-Basement System. In all of the previous models, excluding the gas-gas experiments, salt-water mixtures diffused out of the tube into an infinite fluid environment (tap water basin). This is analogous to a continuous source of buoyancy, such as a fire would supply, which is responsible for the mixing in the unstable density field. However, a finite ambient volume of less dense fluid corresponds to a limited source of buoyancy. The stairwell-basement system was based on this point. The experimental setup and procedure were the same as that for the vertical tube system except for the volume of the ambient fluid. The tap water basin was replaced by a container of tap water of volume comparable to that of the tube.

The mixing observed in the vertical tube was exactly the same as in the previous models. However, the salt-water mixture leaving the mouth of the tube mixed vigorously with the solution in the tap water container. The fluid flow leaving the tube resembled a plume.

Less dense fluid was entrained into it. Later, the exiting fluid impinged on the bottom surface of the container and spread rapidly over it. The size of the volume of ambient fluid had a profound effect on the mixing phenomena in this system. It is shown in Fig. 6.21, which is a plot of $\Delta\rho/\Delta\rho_i$ versus t for three experimental runs (d = 1 1/2", L/d = 15.3) where the volume ratio ($V_{ambient}/V_{tube}$) ranged from 12 to ∞. The plot indicates that the mixing rate decreased as the volume of the ambient fluid decreased. Measurements taken at the end of the experiment revealed the entire system to be of uniform density. This can be seen in Fig. 6.21 because the data points corresponding to $V_r = 12$ level off for large t as the system becomes stable.

In the above experiments, the bottom of the vertical tube was approximately 2" below the surface of the ambient fluid. However, other experiments were performed in the same container with a larger tube (d = 3 3/4", L/d = 7.85), but the inlet of the tube was approximately 6" above the bottom of the container. This configuration is shown in Fig. 6.22 along with its experimental results. In this case, the volume of less dense fluid below the tube was twice the volume of the tube, i.e., $V_r = 2$, and the mixing in the ambient fluid was confined to the region below the tube. The upper (less dense) fluid did not mix with the salt-water mixture leaving the tube. The graph in Fig. 6.22 indicates that the density of the fluid in the tube approached an equilibrium value as in Fig. 6.21 when the volume of the ambient fluid was comparable to that in the tube. Later, the mixing in the entire system ceased, and the density of the fluid in the tube was the

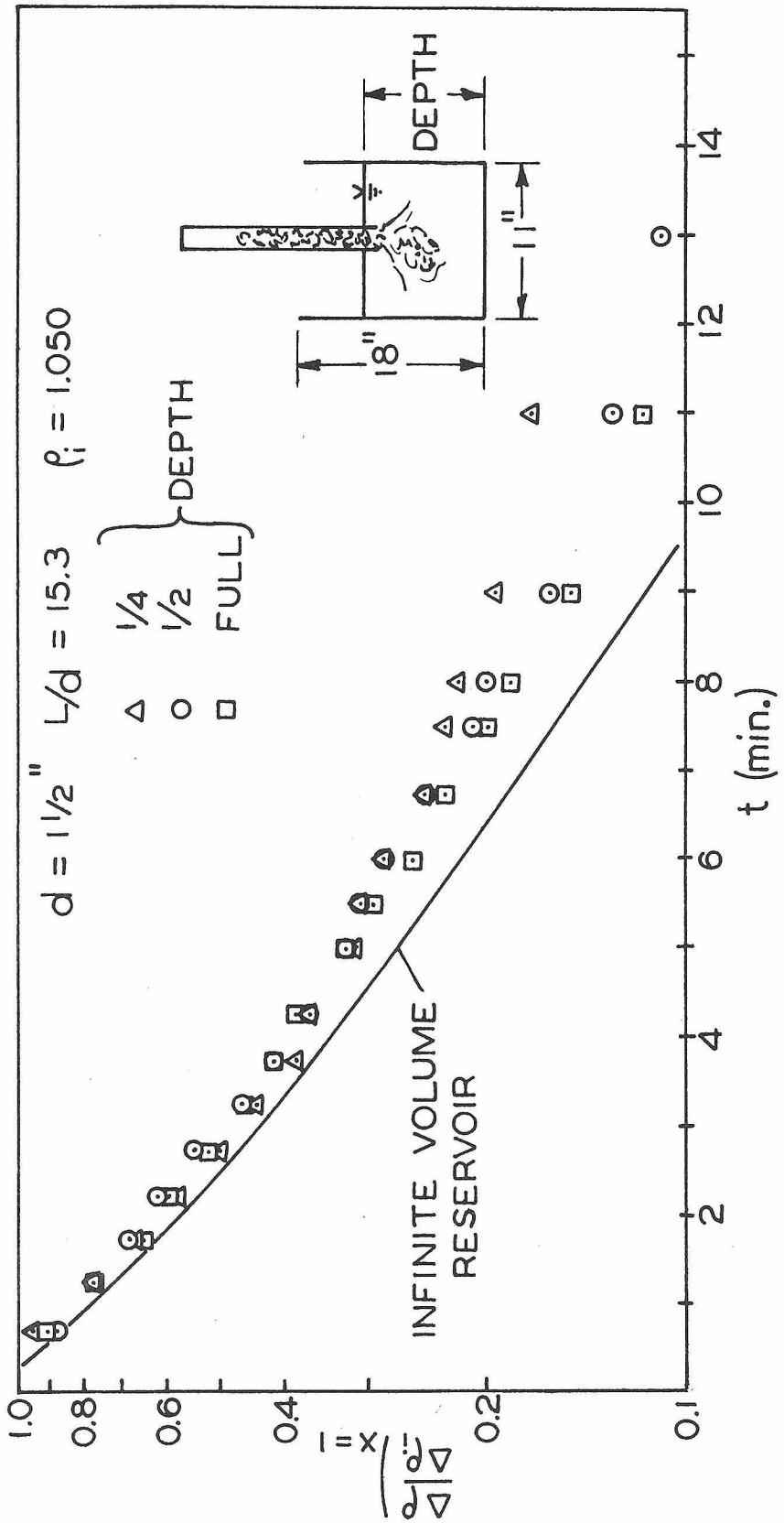

Fig. 6.21 Variations of $\Delta\rho$ with t in the Stairwell-Basement System for $V_r > 12$.

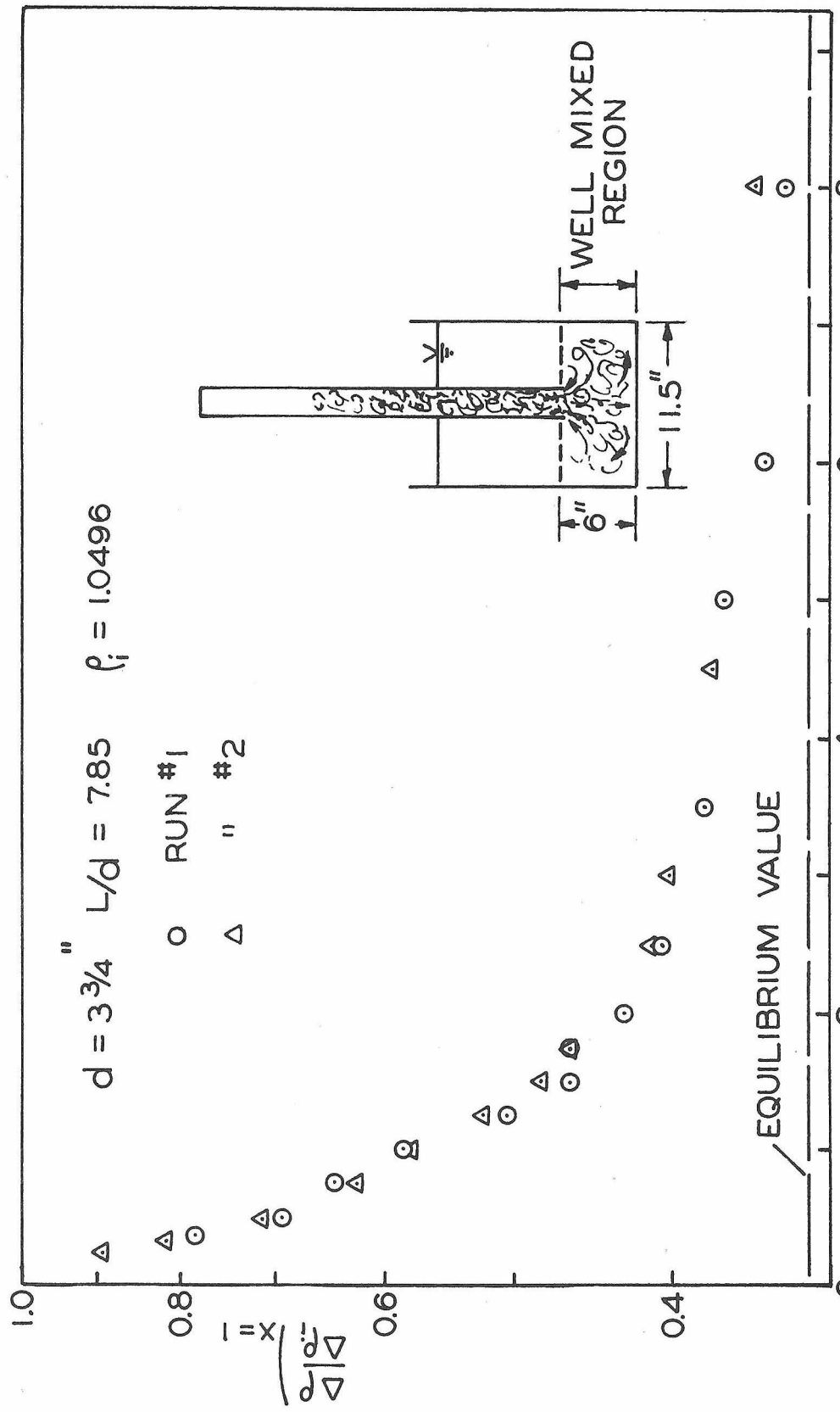

Fig. 6.22 Variation of $\Delta\rho$ with t in the Stairwell-Basement System for $V_r = 2$.

same as that in the region below it. The density of the fluid in the upper region had the same value as it had initially.

The interesting feature of the system in Fig. 6.22 was the intense mixing in the region below the tube. The entire volume was in motion during the mixing process in the tube, and it seemed to be well mixed at all times. Although measurements were not taken to check this observation, the "well-mixed bottom" boundary condition was based on this point. The theory is applied to the experimental results in Figs. 6.23 and 6.24. The data from Fig. 6.21 (d = 1 1/2") are plotted in Fig. 6.23, and the data from Fig. 6.22 (d = 3 3/4") are plotted in Fig. 6.24. In both cases, the ambient density was replaced in the normalization of θ by the final equilibrium density of the system, and $1/\sqrt{H}$ was plotted against τ.

The theoretical values of α/k are not in very good agreement with the experimental values, as is shown in Figs. 6.23 and 6.24. In all cases, the estimated value of α/k should have been larger in order to ensure agreement with the data. The disagreement for d = 3 3/4" (Fig. 6.24) is largest; here, the predicted value of α/k is approximately 43 per cent too small. That is, the mixing rate is greater than that predicted by the theory.

The agreement between theory and experiments for $V_r > 12$ (see Fig. 6.23) is better. This result was expected because the mixing rates change only by roughly 15 per cent for $5 < V_r < \infty$, see Fig. 4.12.

As in the stairwell-corridor system, the fact that a linear curve fits the data points in both plots suggests that the general mixing model is valid. The disagreement between the theoretical and experimental

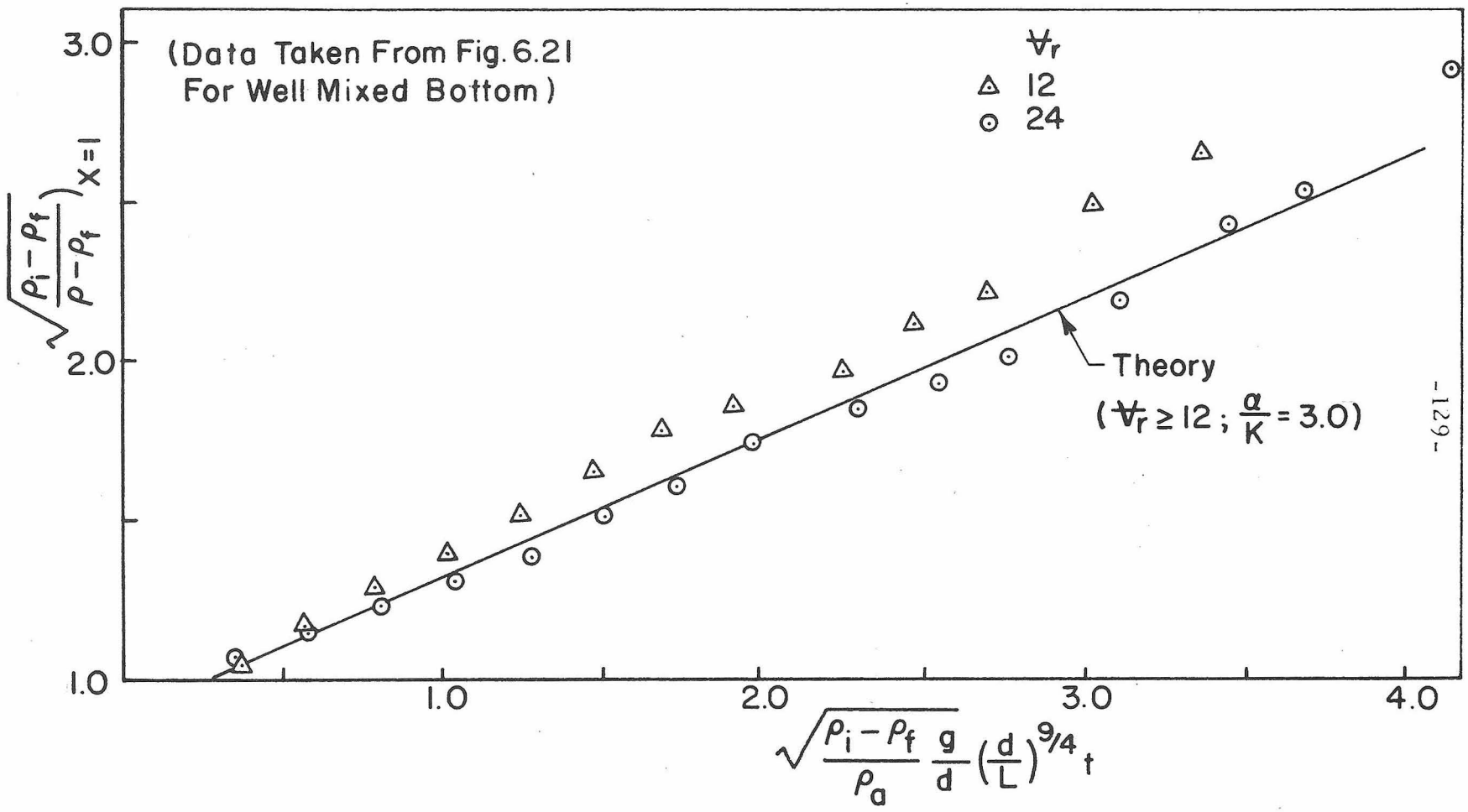

Fig. 6.23 A Comparison of Theory and Experiments for the Well-Mixed Bottom, $V_r > 12$.

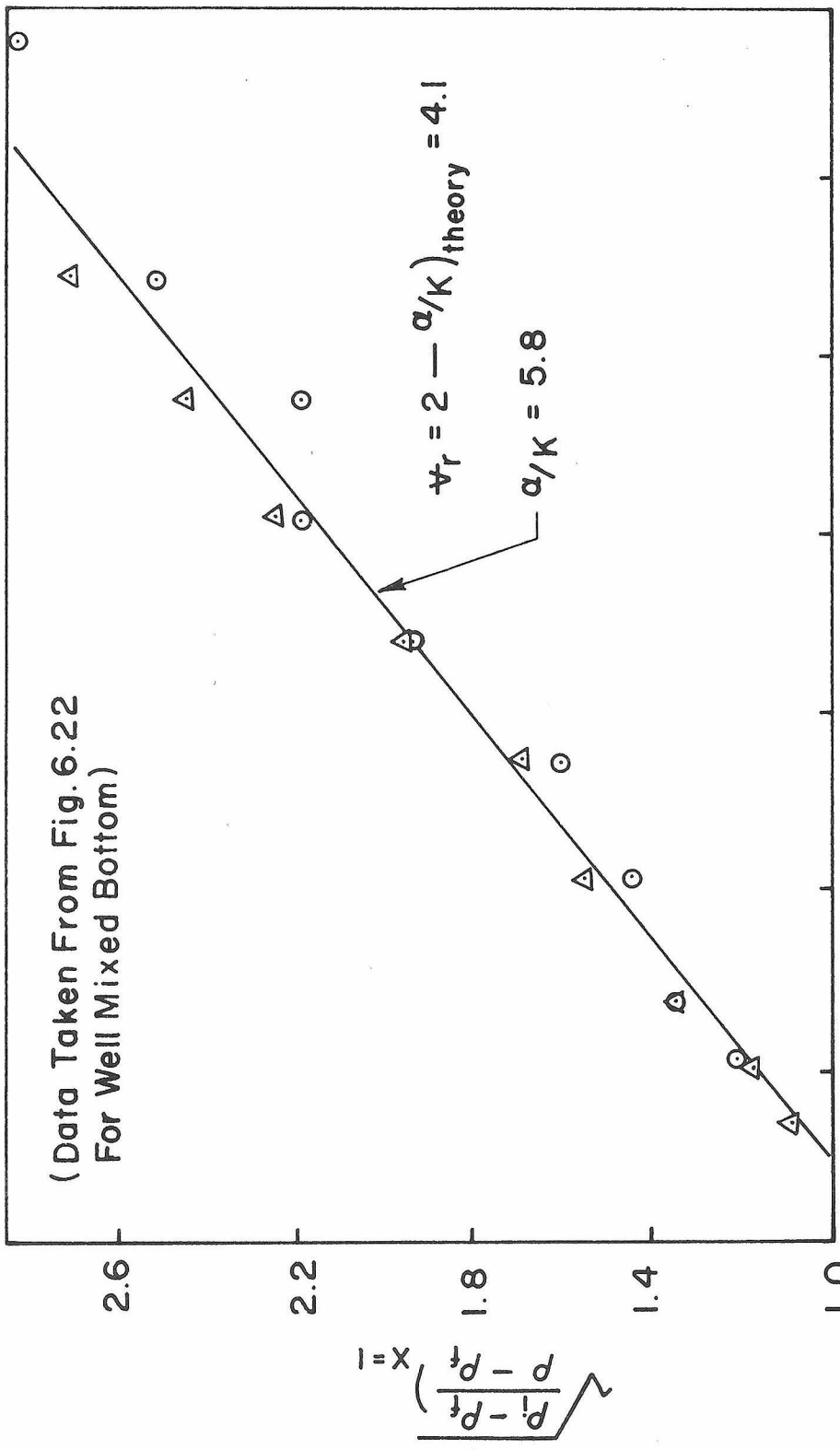

Fig. 6.24 A Comparison of Theory and Experiments for the Well-Mixed Bottom, $V_r = 2$.

slopes could result because the well-mixed bottom boundary condition is not valid. Also, the experiments were difficult to run without introducing turbulence into the bottom region in the tank. The initial disturbances should increase the mixing rate, which means that the experimental slope would be greater than the predicted slope, as was observed in the above cases.

6.1.5 Stairway System. The model of the stairway system consisted of semi-circular discs spaced one diameter apart in a cylindrical tube. The baffle and tube system is shown in Fig. 6.25. The tube and discs were made of lucite. The experimental procedure was the same as in the other cases of the brine solution model.

The mixing process was similar to that of the duct without the baffles. The presence of the semi-discs restricted the movement of the eddies, and they could not spiral in any direction as before. The lighter solution ascended beneath the discs and the heavier solution descended on top of the discs as shown in Fig. 6.25. As a result, individual cells formed between each set of discs that rotated in opposite directions. Most of the mixing occurred at the point where the solution ascended and descended.

The results are plotted in Fig. 6.26 along with a plot of the vertical tube without the baffles. The mixing was reduced by a factor of 10 due to the presence of the baffles. No effort was made to obtain a relation between the number of baffles and the time scale, but the density scaling did not change (i.e., $\tau \sim (\Delta\rho_i/\rho_a)^{\frac{1}{2}}$). These results are very important because they indicate that the presence of obstacles in the vertical ducts greatly reduces the mixing rates. A priori, this

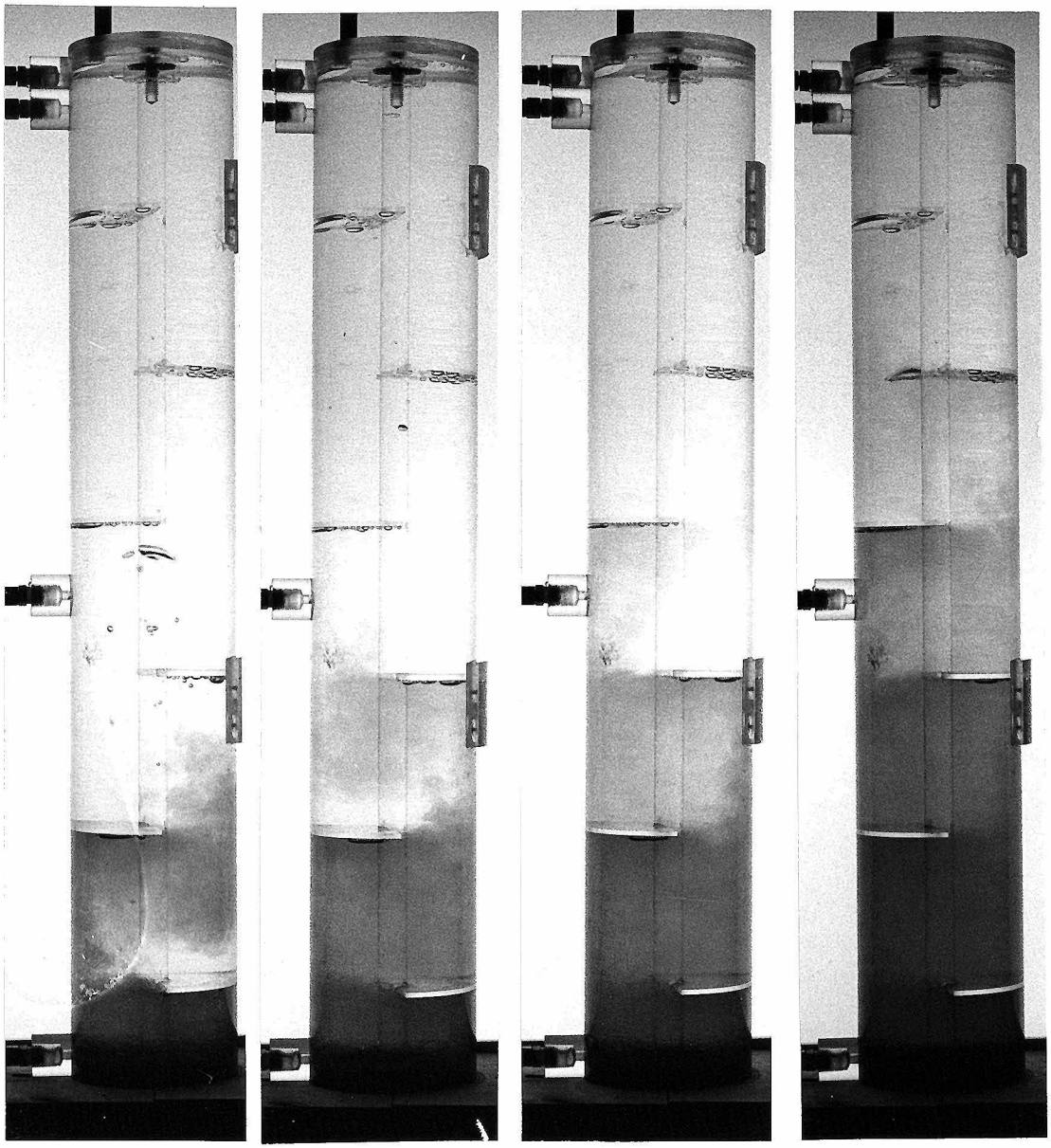

Fig. 6.25 Mixing Patterns in the Stairway System.

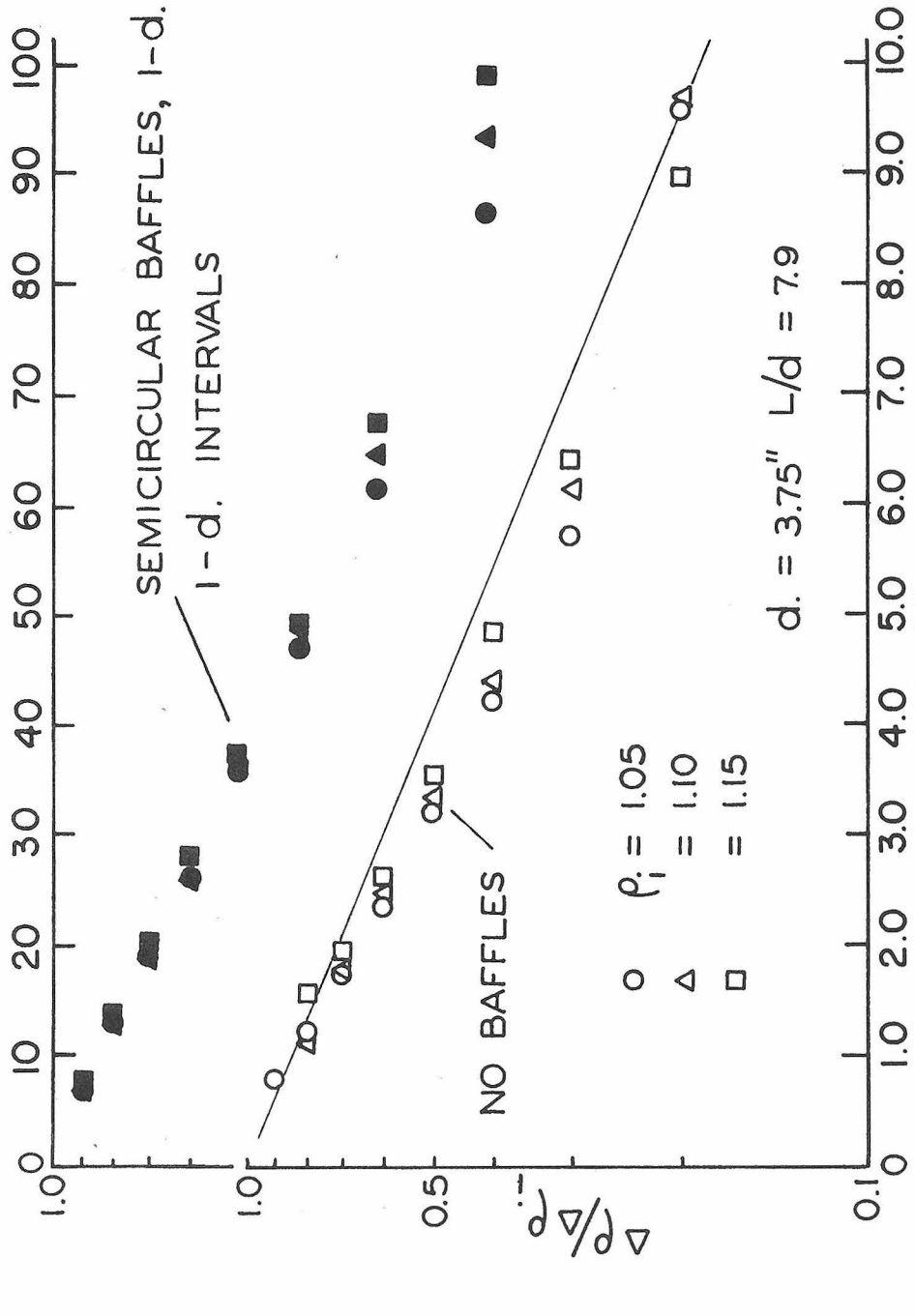

Fig. 6.26 Variation of $\Delta\rho/\Delta\rho_i$ with τ for the Stairway System.

phenomenon was expected because stairs in stairwells tend to reduce the effective diameter of the stairwell. Since the mixing coefficient is proportional to $d^{7/4}$, smaller diameters have smaller diffusion coefficients. Also, the mixing patterns are fixed by the geometry of the obstacles and thus reduce the mixing rates, because higher mixing rates are obtained when the flow is disorganized and random.

6.2 Heat Transfer Model

Figures 6.27 - 6.29 contain the results of the heat transfer experiments with the insulated and constant temperature tubes. The points in each plot are the average of a number of experimental runs for each case. Although visualization of the mixing phenomena was hindered due to the experimental setup, observations revealed the structure of the turbulence to be the same as that in the brine solution model. No attempt was made to vary the free parameters in the experimental model because of the difficulty involved in running the experiments. However, the surface temperature in each case could be varied at will. Acetone/dry ice solutions and liquid nitrogen were used as the coolants to obtain the desired surface temperatures.

The model developed previously furnishes a crude guide for the experimental work. The results were such that these experiments were adequate to explain the phenomena taking place.

6.2.1 Insulated Tube with Heat Transfer through the Top Surface. The insulated tube corresponds to $h = 0$ in the energy equation of the heat transfer model. A schematic of the mixing phenomena in this model was presented in Fig. 4.16 and the solution was discussed in Section 4.3.2 . There we pointed out that heat entered the mouth

of the tube and was conducted through the top surface, of which the temperature T_s was fixed. Also, the flow was steady because the tube system did not retain any of the heat that entered the tube. The experimental results of this model for $T_s = 85^{\circ}K$ (LN_2 temperature) are contained in Fig. 6.27. The graph indicates that the temperature of the upper probes did not approach the liquid nitrogen temperature. The temperature of the top probe, which was located approximately 1 1/2" below the top surface, was about $125^{\circ}K$ above the temperature of the surface. This result was not very surprising. A priori, one expects that the flow will be turbulent everywhere except near the boundaries of the tube and, in particular, that the turbulence will be dampened near the top surface. In this region, one expects the phenomena to be laminar, and that very close to the surface heat will be transferred by a pure molecular conduction process. The scales involved here are reasonable if pure conduction is involved.

The analytical model for the mixing phenomena in this case did not allow for conduction of heat through the top surface. Actually, the analysis is only valid for the flow in the turbulent regions of the tube. The foundation of this analysis was based on the mixing phenomena in the buoyancy force model. In particular, if dense fluid was allowed to flow (with small flow rates) from the top of the tube downward into the less dense ambient fluid surrounding the vertical tube in the buoyancy model, then this flow would be analogous to the flow in the insulated tube. That is, a steady state would exist in the tube of the buoyancy model, and the density at the top would be constant and a maximum there. Also, there would be a mass flux across

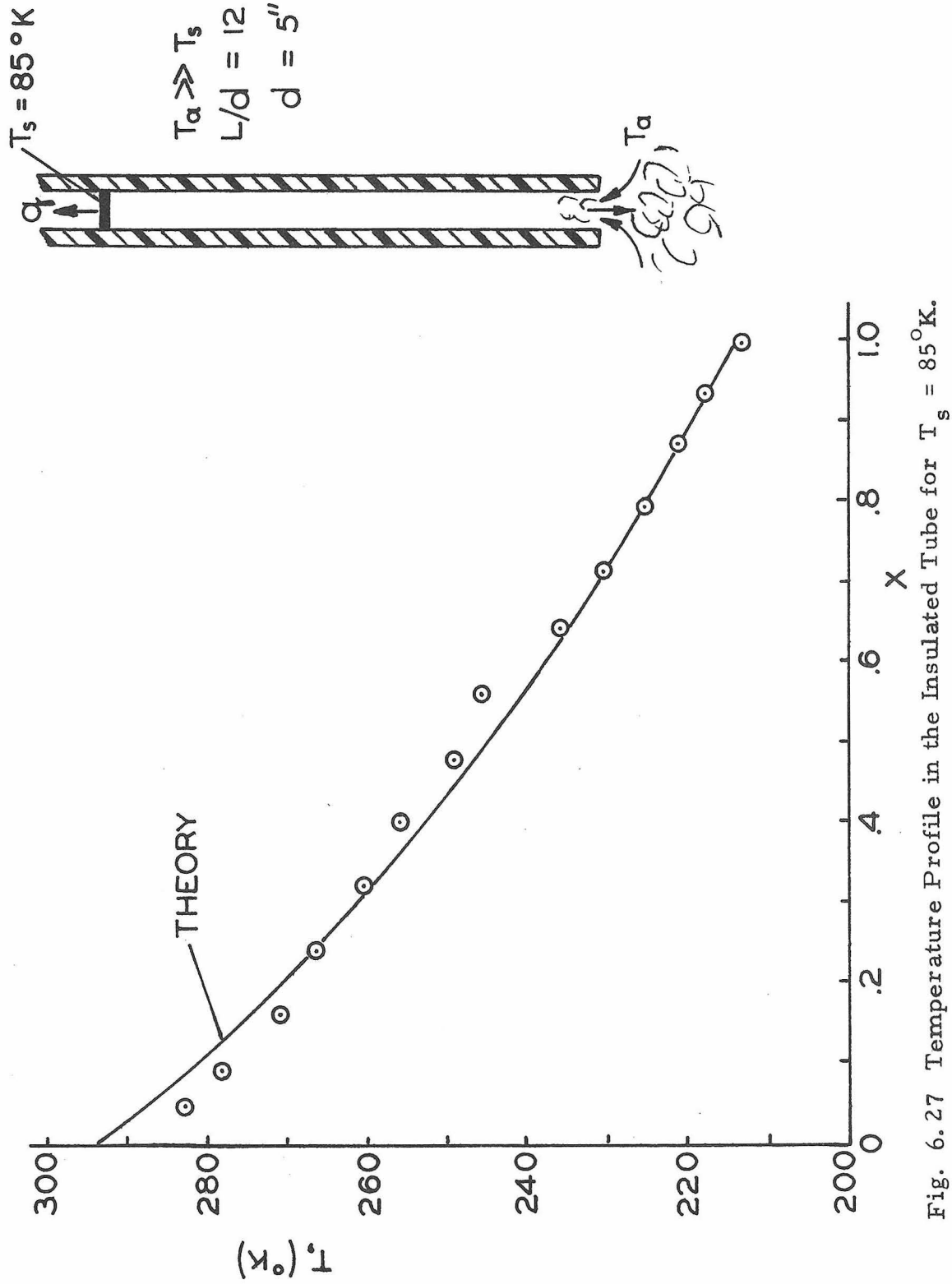

Fig. 6.27 Temperature Profile in the Insulated Tube for $T_s = 85^{\circ}K$.

the top boundary of the tube, and the flow would be turbulent everywhere. However, in the analytical model of the insulated tube, only T_s was specified at the top of the tube, which does not account for the thin thermal boundary layer on its surface.

Therefore, the analytical solution was applied to the experimental results by choosing the boundary condition, T_s, and the length, L, to be the data points near the top of the tube, but below this "conduction" region. This is equivalent to cutting the tube off at the region where it is known to be turbulent and to using the temperature at that point as the boundary condition. In this case, T_s was chosen to be 213°K, which is the temperature of the top probe. The theoretical curve is drawn in Fig. 6.27 with the data points. The agreement is good. The heat transfer coefficient for this system could not be calculated because the heat flux in the tube could not be obtained from the experimental results.

6.2.2 Constant Temperature Tube. Preliminary experiments using the constant temperature tube, $T_s \approx 85^{\circ}K$, indicated that convective heat transfer through the walls of the tube was the dominant energy transfer mechanism. For this wall temperature, the hot gases did not diffuse to the upper 3/4 of the tube. As a result, the density stratification resembled that of a step function with the upper 3/4 of the tube at liquid nitrogen temperature and the bottom 1/4 gradually increasing to room temperature, 295°K. Clearly, this set of experiments corresponds to $h \geq 10^{-3}$ in the heat transfer model, Fig. 4.15. In this case, very large temperature fluctuations were present which made measurements difficult. Hence, a dry ice and

acetone mixture at a temperature much warmer than the liquid nitrogen solution was used. This enabled the room temperature air to diffuse up the tube before its energy was drained by the convective heat flux out of the tube. The reason why the hot gases penetrated to the top of the tube for small T_s and not for large T_s was due to the magnitude of the temperature difference, ΔT, between the hot gas and the cooler walls of the tube. The heat flux was much greater for the colder surface or larger ΔT because the convective heat transfer is proportional to ΔT, and the film coefficient also increases with increasing temperature gradients. The results of this model are contained in Figs. 6.28 and 6.29.

The experiments with the constant temperature tube consisted of two phases. Initially, the surface temperature of the tube, T_s, was kept constant by filling the cavity surrounding the test tube with a mixture of dry ice and acetone. During this period, the process in the tube was steady. The steady-state profile of the gas temperature is shown in Fig. 6.28. This temperature profile resembles the theoretical profiles, Fig. 4.15, for a value of h between 10^{-3} and 10^{-4}. Note that the slope of curve has a maximum value at $x = 0$ and approaches zero near $x = 1$, which implies that the axial heat transfer decreases as x increases. The reason for this behavior is that heat is drained from the mixing eddies at each point along the tube, and that the film coefficient also decreases as x approaches one.

The second phase of the experiment was the transient period after the cavity had been drained. Only air remained in the cooling cavity, and heat transfer from the stagnant cool air in this cavity to

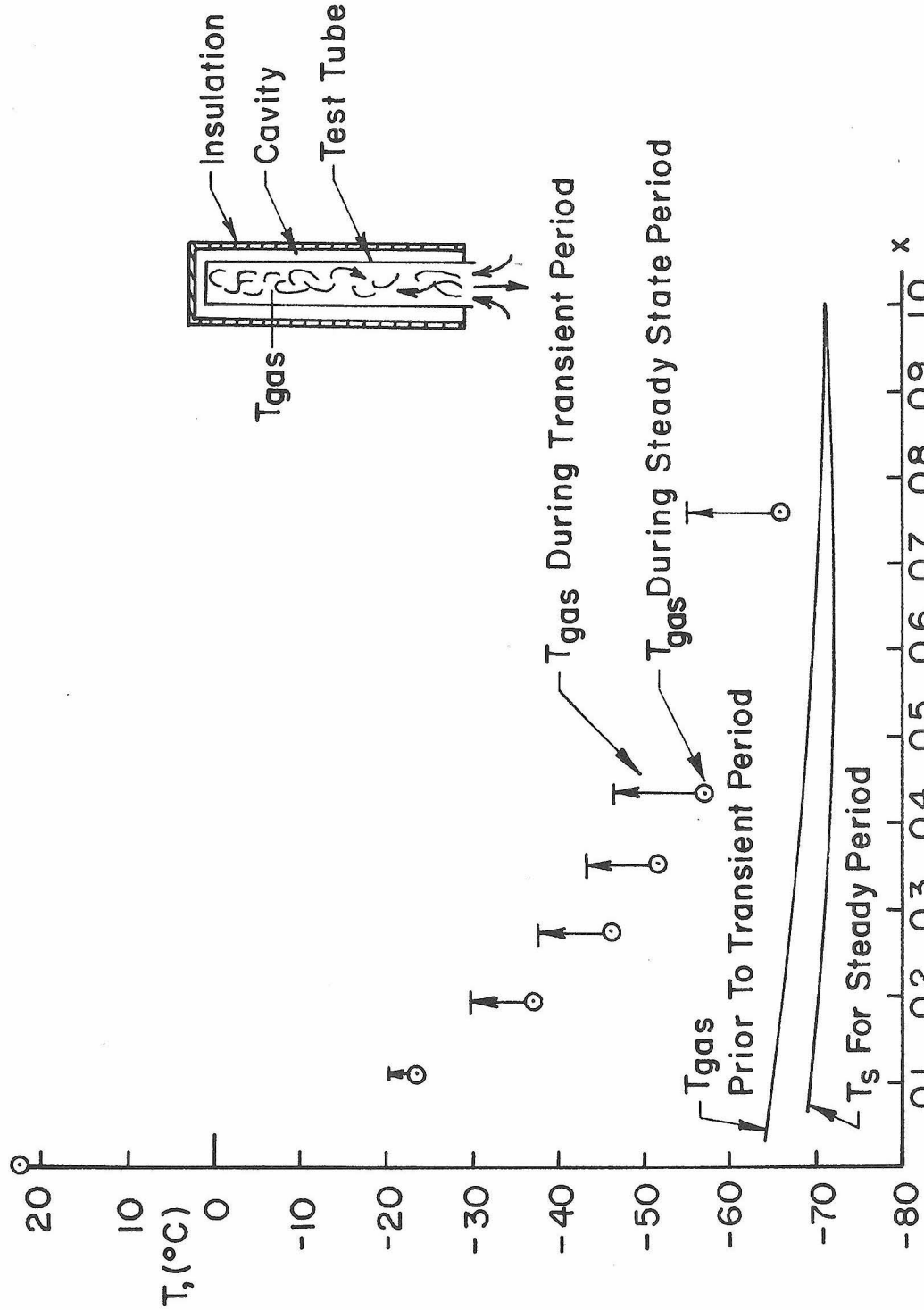

Fig. 6.28 Temperature Profile in the Constant Temperature Tube for $T_s = -70^{\circ}C$.

the thin tube wall was by natural convection alone. Early in the test period, the magnitude of this flux was very small compared with heat transfer from the warm air entering the tube at its open end. The surface temperature of the tube changed during this phase due to heat transfer from the gas inside the tube. Also, the mixing in the tube was reduced slightly because the gas temperature increased during this period, as shown in Fig. 6.28.

The temperature-time history of the surface temperature at certain points is given in Fig. 6.29. The walls of the tube heated up during the transient period as it absorbed energy from the gas entering the tube. Wall temperature data taken during the first 200 - 300 seconds can be used to estimate the heat transfer rates and the heat transfer constant, h. In this calculation, we made use of the "thin skin" approximation in order to estimate the heat transfer to the walls of the tube during the steady period. That is, the initial temperature stratification in the tube was assumed not to vary appreciably during the transient period for which T_s increased with time. This technique amounts to extrapolating all the slopes and temperature differences to their value at $t = 0$.

Figures 6.28 and 6.29 show that the initial temperature profile or slopes did not change very much during the 200 - 300 second transient period, which means that the approximation is valid. The heat transfer to the duct was calculated from the relation

$$q = \rho c_p V \frac{dT_s}{dt} ,$$

where V is the volume of the tube consisting of a section of one di-

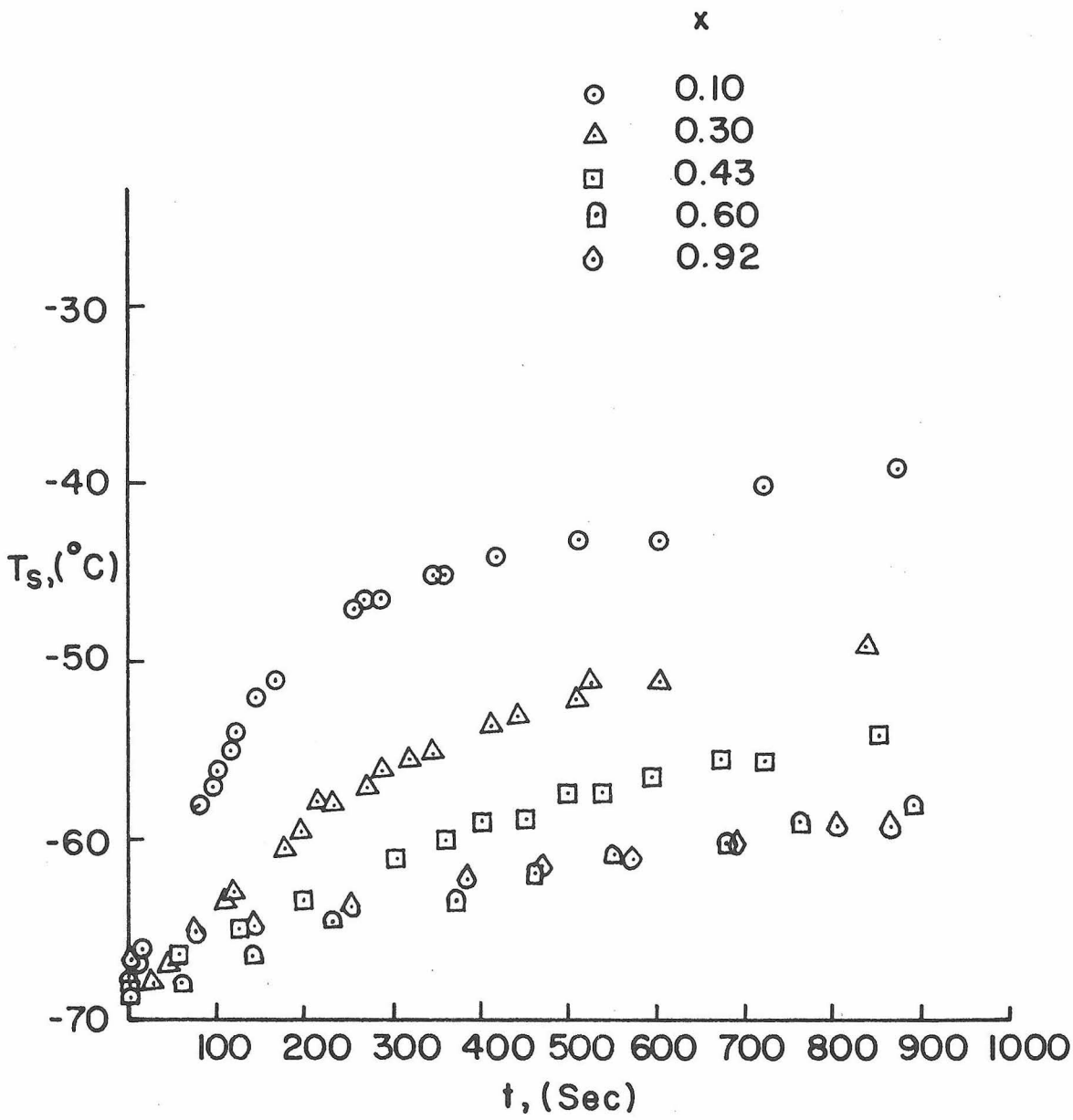

Fig. 6.29 Variation of T_s with t for the Constant Temperature Tube During the Transient Period.

ameter in length. The term dT_s/dt was obtained from the slopes of the curves in Fig. 6.29 for $t < 200$ seconds. The curves are linear in this range, and T_s does not vary from its steady-state value by more than $5^{\circ}C$ for $x > 0.11$.

In the analysis of this model in Section 4.3, we assumed

$$q = HA(T_s - T) \tag{4.55}$$

and

$$\frac{H}{\left(\frac{\rho_a c_p}{d}\right)} = h \cdot \frac{1}{4} \sqrt{\frac{g}{\rho} \frac{\partial \rho}{\partial z}} \, (d^7 L)^{1/4} , \tag{4.64}$$

where A is the surface area of the tube. Equating the values of q from these equations and solving for h yields

$$h = \left\{ \frac{(\rho c_p)_{tube}}{(\rho_a c_p)_{gas}} \left(\frac{Vd}{A} \right) \cdot \frac{4}{(d^7 L)^{1/4}} \right\} \frac{dT_s/dt}{\sqrt{\frac{g}{T} \frac{dT}{dz}} \, (T_s - T)} .$$

In this expression, $\frac{1}{\rho} \frac{d\rho}{dz}$ was replaced by $-\frac{1}{T} \frac{dT}{dz}$, which is equivalent when the pressure is assumed constant in the equation of state. Note that the quantity $4/(d^7 L)^{1/4}$ was used to scale the mixing coefficient of the buoyancy model. The temperature gradient of the gas in the tube was obtained from the steady-state profile in Fig. 6.28. Therefore, h was calculated from this expression at certain regions along the tube for $t = 100$ seconds. The results are tabulated in Table 6.3.

In the theoretical model, h was assumed to be constant. Excluding the value computed near $x = 0.1$, h is approximately constant to within 30 per cent. The value of h computed near the inlet of the tube does not agree with the other values; this is probably due to the

TABLE 6-3. The Values of h Computed from the Thin Skin Approximation.

x	$h \times 10^{-3}$
0.11	4.35
0.30	11.30
0.43	7.32
0.60	13.0

relatively large heat losses at that region.

The 1/8" steel flange located near the inlet of the tube (see Fig. 5.11) served as a heat sink, since its heat capacity was larger (roughly by a factor of 10) than that of the tube in that region. Therefore, it drained energy from the tube during the transient period which decreased dT_s/dt at $x = 0.11$ and hence decreased the heat transfer constant. Also, the axial heat conduction between points along the tube was greatest in that area.

The average value of h obtained from the experiments (Table 6-3) is of the order of 10^{-2}, which is larger, by roughly a factor of 10, than that of the theoretical model required to match the temperature profile. The actual value of h corresponding to the steady-state temperature profile in Fig. 6.28 was not calculated, but it is of the order of 10^{-3}, since this temperature profile agrees with the data in the theoretical curves (see Fig. 4.15) for h in this range.

Besides experimental error, the disagreement between the theoretical and calculated values of h could be due to the length scaling in the film coefficient, H. The form of H was assumed to be

the same as that of the mixing coefficient in the buoyancy model. However, the scaling quantity $\frac{1}{4}(d^7L)^{1/4}$ may be different in this model, and the value of h would be different also.

6.3 Discussion

In the previous sections of this chapter, the experimental results were presented and discussed in general. This section contains a more critical discussion of the models and the assumptions made when analyzing them. Also, the experimental errors are discussed.

6.3.1 Sources of Experimental Error. The most common sources of error in the experiments of the buoyancy force model were due to the initial turbulence in the system and to the finite ambient volume of less dense fluid in the brine solution experiments.

The initial turbulence in the system was due to the removal of the plug from the inlet of the tube. During the process of removing the plug the ambient fluid was disturbed, and also the ambient fluid rushed in to fill the space vacated by the plug. The turbulence that was put into the system by this process aided the mixing in the tube, and this distorted the results. Whenever the duration of the experiment was long for $L/d > 8$, the turbulence affected only the initial part of the data. However, for $L/d < 8$, the accuracy of the data was dependent on the magnitude of the disturbances initially in the system. Therefore, care was taken to avoid disturbing the ambient fluid excessively.

The size of the ambient volume of less dense fluid became important during the latter part of the brine solution experiments involving the largest of the tubes ($d = 7\ 1/8''$, $L/d = 15.6$). An infinite

(less dense) fluid environment was desired so that the ambient fluid density would approximately remain constant throughout the mixing process in the tube. This was not the case in all the experiments involving the 7 1/8" tube because of the large volume of salt-water mixture in the tube. The dense fluid that fell from the inlet of the tube entrained the less dense fluid very rapidly. The mixing in the ambient tank was very intense because of the large volume flow of brine solution out of the tube. Also, the entrainment caused disturbances in the ambient fluid. In most instances, a large clockwise spiral or vortex was observed around the tube. This phenomenon tended to distort the results.

The experimental error in the heat transfer experiments was of a different nature. Water vapor in the ambient air froze at some points on the inner surface of the test tube during all of the experiments. The ice on the inner surface affected the heat transfer to the walls of the duct, but not by any significant amount. Dry air should be used for the ambient fluid in order to avoid this problem in future experiments.

In the analytical models, the quantities ρ and T were assumed to be cross-sectional averages. However, only one probe was placed in the middle of the duct at a particular cross section, and each experimental run was repeated twice in most instances. Clearly, this is not a cross-sectional average, but the remarkable phenomenon was that the data were reproducible to within a few per cent in most cases. Initially, it was feared that one probe in the middle of the duct would not be representative of a cross-sectional average because of the high

intensity of the mixing. Later this notion was dropped because the results were reproducible. This is partly due to the mixing mechanism and to the turbulence itself. The mixing in the tube seems random and disorganized. Probably this is true locally, but not so when the tube is considered as a whole. The large eddies (in the brine solution model) that transport the solution up the duct can only propagate a certain distance before they break up into smaller eddies at each cross section. The distance a front propagates (as described in Section 4.1) is a function of the density stratification in the tube. Mixing of the smaller eddies is random, but they are confined to a length scale of the order of the tube's diameter. This is probably why the data are reproducible at any cross section.

6.3.2 Discussion of the Diffusion Equation of the Buoyancy Model. In the derivation of the turbulent diffusion equation of the buoyancy force model, the average velocity of the solution at any cross section in the tube was assumed to be zero. This assumption seems reasonable, since the velocity was unweighted and there was no net volume flux of solution in the tube. However, there was a net flux of salt out of the tube and also a net flux of water into the tube. The conservation equations could have been written to include the efflux of salt out of the tube. If the velocities used in these equations were the mass average values, they could not be considered zero when using Reynolds' averaging techniques. It is not clear what effect the addition of the advective term in the conservation equations would have on the solution. In the existing analysis, all of the advective transport was lumped into the diffusion coefficient by means

of Reynolds' analogy. The agreement of the model calculations with the experimental data was very good except for a short time period following the arrival of the initial front.

The turbulent diffusion coefficient in the buoyancy force model was assumed to have the form: $E_z \sim \sqrt{\frac{g}{\rho_a} \frac{\partial \rho}{\partial z}}$. A more general expression would be to replace ρ_a by ρ ; that is, $E_z \sim \sqrt{\frac{g}{\rho} \frac{\partial \rho}{\partial z}}$. A priori, one is more likely to use the latter expression, but the experiments suggest that the former gives an adequate representation even when ρ/ρ_a changes by a factor of 2 or more (as happens in the gas-gas experiments). In all of the plots of $\Delta\rho/\Delta\rho_i$ against τ, the initial portion of the curve exhibited an exponential relationship. Also, the same phenomenon existed for all τ when the initial density was small. This is shown in Fig. 6. 30, which is a plot of the results of the brine solution model where d and L/d were held constant and $\Delta\rho_i/\rho_a$ varied from 1 per cent to 15 per cent. The graph indicates that for $\Delta\rho_i/\rho_a \leq 2$ per cent, the diffusion process is exponential. However, the curves in the plot are not linear for $\Delta\rho_i/\rho_a > 2$ per cent.

The reason for this behavior could be due to the form of E_z . Perhaps $1/\rho$ is important, since $\Delta\rho_i$ is small in these experiments; whereas in the previous cases, $\Delta\rho_i$ was large and replacing ρ by ρ_a does not introduce much error. Another possible reason could be due to the omission of the advective transport term in the diffusion equation. Initially, the salt particles have a large velocity, and during the latter stages it is very small and can be neglected.

6.3.3 Discussion of Boundary Conditions Using the "Well-Mixed" Assumption . The agreement between the theoretical and ex-

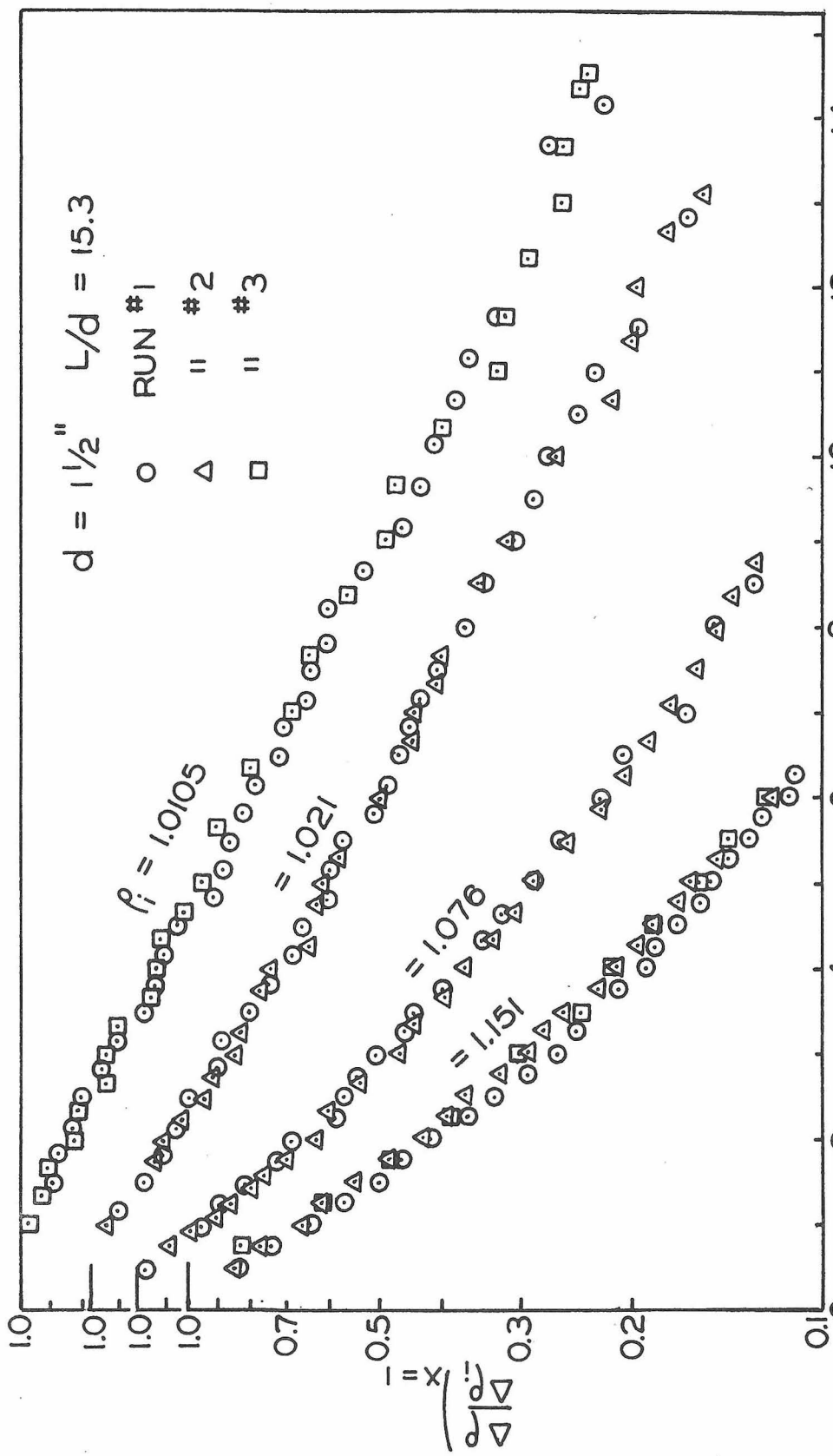

Fig. 6.30 The Exponential Behavior of $\Delta\rho$ with t for Small $\Delta\rho_i/\rho_a$.

perimental values of the slope, $\alpha/2$, in the stairwell-corridor and stairwell-basement systems was not very good. In each model, the experimental slope was too large. However, the general form of the proposed mixing mechanism in each model appeared to be valid because a linear curve could be drawn through the data points when they were plotted as $1/\sqrt{H}$ against τ. It appears that the "well-mixed" boundary conditions are not accurate, because they fix the value of the slope in each case.

In the brine solution experiments of the stairwell-corridor system, the "well-mixed top" boundary condition was based on the fact that the density at the top of the vertical tube was nearly the same as the density at the end of the horizontal tube for all times investigated. It is obvious that this could not be true before the two-layered flow system in the horizontal tube has been fully established. The time elapsed between the arrival of the initial front at the top of the tube and the end of the developmental period of the flow in the horizontal tube may be enough to distort the results. The theory has no way of taking this elapsed time into account. It seems as if τ_o would be larger in order to account for this time period. However, it is remarkable that the separation of variables solution is applicable in this case. Also, we pointed out in Section 4.2.3 that the addition of the horizontal attachment could change the length scaling in the model because of the increase in the turbulence near the top of the tube. This increased turbulence would be effective in increasing the overall mixing rates.

The "well-mixed bottom" boundary condition of the stairwell-basement model was based on the observation that the ambient fluid beneath the tube was mixed thoroughly due to the flow leaving the tube. Measurements were not taken to check the validity of this assumption as in the above case. However, the diffusion equation was solved using this boundary condition.

A second problem concerning this exit assumption is that it is not certain that the theory can account for the dense fluid that diffused from the tube before the initial front reached the top surface at $\tau = \tau_o$. In the previous case, the ambient fluid environment was infinite and we assumed $F = 0$ at $x = 0$, but in this case $F \neq 0$ at $x = 0$ because the density of the ambient fluid increases with time. This initial density is computed from the model, but it should properly be stated initially. However, comparison between values of $F\{x = 0, \tau = \tau_o\}$ calculated from the model and from a continuity model based on an assumed distribution of density in the tube at τ_o shows that they are almost equal. A final source of error may be that the bottom mixing may not be as thorough as expected on the basis of visual observations.

6.3.4 Discussion of Heat Transfer Model. In the heat transfer model, the walls of the duct were assumed to be constant in temperature. This hypothesis is only valid during the early stages of the fire before the walls have absorbed a sufficient amount of energy. The heat transfer experiments revealed that it is possible for the walls of the duct to drain most of the energy from the mixing eddies and inhibit them from propagating to the top of the duct. However, the

propagation of the gases or heat up the duct depends on the local temperature or density gradients and temperature differences relative to the walls. During the latter stages of the fire, the walls will be very hot and the amount of energy drained from the gases en route to the upper floors would not be significant. For this reason, it is important to know the length of the time interval during which the constant temperature assumption is valid. However, it was not obtained from these experiments because of the difficulty involved in performing them.

The theory for the heat transfer model was not as complete as that for the buoyancy model. The analysis of the buoyancy model related the diffusion constant to the slopes of the density-time curves, which enables it to be found empirically. However, this was not the case for the heat transfer model because the heat transfer constant was arbitrary and the analysis did not provide any basis for calculating it. Another point worth noting is that the steady state solution did not depend on the magnitude of the diffusion coefficient. That is, all of the scaling quantities (such as d, L, etc.) cancelled from the energy equation (see Eq. 4.61), since the film coefficient was assumed proportional to the diffusion coefficient. The solution would depend on the scaling quantities if the transient problem had been solved.

In spite of the crudeness of the theoretical heat transfer model, it is useful because the temperature profiles of the steady state solution are very similar to those found in the experiments.

7. SUMMARY AND CONCLUSIONS

This research project was motivated by the large number of fatalities from fires in homes and multi-story buildings each year. The major concern of this report was to analyze the flow mechanism and to develop simple modeling parameters by which hot gases propagate to the upper floors of high rise buildings.

The problem examined in this investigation has been the turbulent motion of hot gas through vertical shafts (e. g. ,ventilation shafts, stairwells, or elevator shafts) and horizontal passages (such as halls) when natural convection is the most important driving force. Primarily, consideration was given to the transient flow situation in which the gas in the shaft is initially cold; then, at some time, the bottom end of the vertical shaft, or either end of the horizontal shaft, is opened to allow a hot gas atmosphere outside the shaft to mix with the cold gas inside the shaft. Mixing in all cases is the result of natural convection alone.

The models were divided into two categories: a buoyancy force model,and a heat transfer model that includes buoyancy forces. Brine solutions and dense gases were used to model the buoyancy forces,and the heat transfer model made use of low temperature air. In both cases, the diffusion equation was solved and found to be in agreement with the experimental models. The following major conclusions can be drawn from the buoyancy model:

1) Salt-water mixtures can be used successfully to model buoyancy forces due to dense gases in an unstable density stratification.

2) The fundamental time scale that characterizes mixing rates in vertical columns due to unstable buoyancy forces is

$$\tau \equiv \sqrt{\frac{\Delta\rho_i}{\rho_a}\frac{g}{d}}\left(\frac{d}{L}\right)^{9/4} t \ .$$

3) The turbulent diffusion coefficient for the flow induced in a vertical column of fluid with an unstable density stratification is

$$E_z = 0.28\sqrt{\frac{g}{\rho_a}\frac{\partial\rho}{\partial z}}\,(d^7 L)^{1/4} \ .$$

4) The density stratification due to the mixing caused by unstable buoyancy forces in a vertical column of fluid placed in an infinite environment of less dense fluid can be described as follows:

$$\frac{\rho-\rho_a}{\rho_i-\rho_a} = \frac{F(x)}{\left[\frac{\alpha}{2}(\tau-\tau_o)+1\right]^2} \ ,$$

where F(x) is plotted in Figure 4.9. This solution is only valid when turbulent mixing exists throughout the column.

5) The propagation of density currents along the upper surface of a horizontal duct can be described as follows:

$$V = 0.45\sqrt{\frac{\Delta\rho_i}{\rho_a} gd} \ ,$$

where V is the speed of the front and d is a characteristic length.

6) Obstacles in vertical columns (such as stairs in a stairwell) reduce the mixing rates associated with the mixing phenomena due to unstable buoyancy forces in an unstable density field.

In the heat transfer model, the unstable buoyancy forces were due to temperature differences in the air rather than to specie changes as in the buoyancy model. The major conclusions that can be drawn

are as follows:

The mixing caused by hot gas entering a vertical duct filled with a relative cool gas is reduced by the heat absorbed by the walls of the duct. In some instances, depending on the temperature difference between the wall and the hot gas, it is possible for the heat flux out of the system to inhibit the hot gas from propagating to the top of the duct.

LIST OF SYMBOLS

For simplicity, symbols of secondary importance which appear only briefly in the text are omitted from the following list.

c	concentration of solute in the salt-water mixture, (mass/volume)
d	tube diameter
D	molecular diffusion coefficient; mixing coefficient (heat transfer model)
E_z	turbulent mixing coefficient
F	normalized density profile, $\Delta\rho(x)/\Delta\rho_i$
g	acceleration due to gravity
h	heat transfer constant
H	normalized density at top of tube, $\Delta\rho/\Delta\rho_i\|_{x=1}$ in the buoyancy model; film coefficient in the heat transfer model
k	diffusion constant
L	length of tube
M	molecular weight of gas mixture
$\dot{q}$	convective heat transfer to the duct
R	universal gas constant
t	time
t_ρ	time scale for various initial density ratios
$t_{d/L}$	time scale for various diameter-to-length ratios
T	temperature of gas mixture
T_a	ambient fluid temperature
T_s	surface temperature of tube
$\underline{V}$	velocity vector
V_r	volume ratio

x	normalized position along the central axis of the tube, z/L
z	position along the central axis of the tube
z_f	position of initial front
$\alpha/2$	slope of the theoretical curve, $1/\sqrt{H}$ versus τ
θ	normalized density, $\Delta\rho/\Delta\rho_i$
ρ	density of fluid
ρ_a	ambient density of fluid
ρ_f	equilibrium density of system
ρ_i	initial fluid density
$\Delta\rho$	$\rho-\rho_a$
$\Delta\rho_i$	$\rho_i-\rho_a$
$\Delta\rho_L$	$\rho(x=1) - \rho_a$
τ	fundamental time scale
τ_o	arrival time of initial front
τ_{avg}	average value of τ for various $\Delta\rho_i/\rho_a$
τ'	time scale for initial period, $\tau < \tau_o$

REFERENCES

1. International Conference on Fire Safety in High Rise Buildings, General Services Administration, Airlie House (May 1971).

2. America Burning, the Report of the National Commission on Fire Prevention and Control (May 1973).

3. Hutcheon, N. B. and Shorter, G. W. "Smoke Problems in High Rise Buildings," paper presented at ASHRAE Annual Meeting, Lake Placid, New York (June 1968).

4. International Symposium on the Use of Models in Fire Research, National Academy of Science - National Research Council, Publication 786 (1961).

5. Fung, Francis C. W. "Quantitative Evaluation of a Pressurized Stairwell Smoke Control System for a 12-Story Apartment Building," National Bureau of Standards, Interim Report (June 1973).

6. Benjamin, T. Brooke "Gravity Currents and Related Phenomena," Journal of Fluid Mechanics, Vol. 31 (1968), pp. 209-248.

7. Yih, Chia-Shun, Dynamics of Nonhomogeneous Fluids, The MacMillan Co., New York (1965).

8. Standard Methods for the Examination of Water and Wastewater, American Public Health Association, New York (1971), pp. 325-326.

9. Landau, L. D. and Lifshitz, E. M. Fluid Mechanics, Addison-Wesley Publishing Co., Reading, Mass. (1959), pp. 195-196.

10. Fitzgerald, R. W. "Multi-Protection Design: Fire," in Multi-Protection Design, edited by R. E. Kummer and R. B. Sprankle. Defense Civil Preparedness Agency, TR-20, Vol. 6 (Dec. 1973).